

Quantum Jumps of One and Two Atoms in a Strongly Coupled Atom-Cavity System

Diplomarbeit

von

Alexander Thobe

geb. am 23. August 1984 in Hannover

angefertigt am
Institut für Angewandte Physik
der Rheinischen Friedrich-Wilhelms-Universität Bonn

vorgelegt an der
Mathematisch-Naturwissenschaftlichen Fakultät I
der Humboldt-Universität zu Berlin

04. Juni 2009

1. Gutachter: Prof. Dr. Oliver Benson
2. Gutachter: Prof. Dr. Dieter Meschede

Abstract

In this thesis I present an experimental investigation of the hyperfine groundstate dynamics of one and two neutral caesium atoms coupled to a high finesse optical resonator. The atom-cavity system is in the strong coupling regime, where coherent interaction dominates over energy dissipation. The hyperfine state is detected nondestructively via the dispersive shift of the resonator frequency induced by the atom-light interaction.

The existing experimental setup used for the measurements in this thesis is described in chapter 1. It allows to cool and trap single caesium atoms and transport them with high precision into the light field of a high finesse optical resonator. To achieve fast and nondestructive state detection it is important to detect the photons transmitted through the resonator with high efficiency. I have optimized the photon detection setup, which has improved the detection efficiency by a factor of three.

In chapter 2 I present continuous measurements of the hyperfine state of one and two caesium atoms inside the resonator. They reveal quantum jumps between the two hyperfine groundstates of caesium. I have performed a detailed analysis of the statistical properties of these quantum jumps and modeled them theoretically. The measurements of the two-atom quantum jump signals point towards the experimental implementation of a scheme for probabilistic, measurement-induced entanglement generation. In chapter 3 I theoretically analyze this scheme in detail and give an estimate of the entanglement fidelity achievable with our setup under optimal conditions.

Zusammenfassung

Gegenstand dieser Arbeit ist die Untersuchung der Dynamik des Hyperfein-Grundzustands von ein und zwei neutralen Cäsium Atomen in einem optischen Resonator hoher Finesse. Das gekoppelte Atom-Resonator System ist im Regime starker Kopplung, in dem die kohärente Wechselwirkung über die Dissipation dominiert. Der Hyperfeinzustand wird nicht-destruktiv über die dispersive Verschiebung der Resonatorfrequenz nachgewiesen, die durch die Wechselwirkung des Atoms mit dem Resonatorfeld verursacht wird.

Der bereits bestehende experimentelle Aufbau, der für die Messungen in dieser Arbeit benutzt wurde, erlaubt es einzelne Cäsium Atome zu fangen, zu kühlen und mit hoher Präzision in einen optischen Resonator zu transportieren. Der Aufbau ist in Kapitel 1 beschrieben. Um den Zustand schnell und nicht-destruktiv zu detektieren, ist es wichtig die Photonen, die durch den Resonator transmittiert werden, mit hoher Effizienz nachzuweisen. Ich habe den Aufbau zur Photonendetektion optimiert und konnte die Effizienz um einen Faktor drei verbessern. Der verbesserte Detektionsaufbau wird ebenfalls in Kapitel 1 vorgestellt.

In Kapitel 2 präsentiere ich kontinuierliche Messungen des Hyperfein-Grundzustands von ein und zwei Atomen im Resonator. Diese Messungen zeigen Quantensprünge zwischen den beiden Hyperfein-Grundzuständen von Cäsium. Ich habe die statistischen Eigenschaften dieser Quantensprünge im Detail analysiert und theoretisch modelliert. Die Messungen der Zwei-Atom Quantensprünge sind ein Schritt hin zur experimentellen Realisierung eines Verfahrens zur messinduzierten Verschränkung zweier neutraler Atome. In Kapitel 3 analysiere ich dieses Verfahren theoretisch und gebe eine Abschätzung der Güte der Verschränkung, die mit unserem experimentellen Aufbau erreicht werden kann.

Contents

Introduction - Measuring the Quantum	1
1 Strong Coupling of Atoms and Photons Inside a High Finesse Optical Resonator	3
1.1 Theoretical Description of Atom-Light Interaction in a Resonator	3
1.1.1 Coherent Atom-Light Interaction - The Jaynes-Cummings Model . . .	3
1.1.2 Decoherence via Dissipation - The Master Equation	5
1.2 Experimental Implementation of a CQED System in the Strong Coupling Regime	9
1.2.1 Preparation of Cold Atoms and Transport into the Resonator	9
1.2.2 Characteristics of the High Finesse Resonator and Resonator Stabilization	11
1.2.3 Detection of the Resonator Transmission	15
1.2.4 Influence of the Caesium Multi-Level Structure	19
1.2.5 Continuous Monitoring of the Atom Light Interaction via the Resonator Transmission	21
2 Quantum Jumps of Neutral Atoms in a Resonator	23
2.1 Non-Destructive State Detection Using a High-Finesse Optical Resonator . . .	23
2.1.1 A Resonator as an Atomic State Detector	24
2.1.2 Influence of Experimental Parameters on the Performance of the State Detection	27
2.2 Continuous Observation of Single Atom Quantum Jumps	30
2.3 Quantum Jumps of Two Atoms Coupled Simultaneously to the Resonator . . .	37
2.3.1 Distinction of One and Two Atoms Coupled to the Resonator	37
2.3.2 Atom Number Dependent Quantum Jump Rate	40
2.3.3 Two-Atom Random Telegraph Signals	44
3 Measurement-Induced Entanglement	51
3.1 Mølmer's Probabilistic Entanglement Scheme	51
3.2 Fidelity of the Entanglement Operation	52
3.3 Experimental Implementation of the QND Measurement	56
3.3.1 Transmission Level Detection	56
3.3.2 Homodyne Phase Detection	57
3.4 Influence of Technical Noise and Variation of g	61

Outlook - Control, Control, Control	63
Appendix	65
Appendix A Calculation of the Quantum Jump Time	65
Appendix B Two-Atom Intensity Auto-Correlation Function	67
Appendix C Homodyne versus Transmission Level Detection	71
Bibliography	73

List of Figures

0.1	Schematic Sketch of Atom-Light Interaction in a Fabry-Perot Cavity	2
1.1	Energy Spectrum of the Jaynes-Cummings Hamiltonian	5
1.2	Schematic of a Cavity QED system	6
1.3	Cavity Transmission as a Function of Cavity-Atom Detuning and Probe-Cavity Detuning	8
1.4	Experimental Setup of MOT and Optical Lattice	10
1.5	ICCD Image of Two Atoms in the Optical Lattice	11
1.6	Schematic and Photograph of the High Finesse Optical Resonator	12
1.7	Cavity Ringdown	13
1.8	Stabilization Setup	14
1.9	Laser Configuration Inside the Resonator	15
1.10	Schematic of the Probe Laser Detection Setup	17
1.11	Reflection Spectrum and Sketch of the Volume Holographic Grating	19
1.12	Scattering Processes Induced by the Probe Laser	20
1.13	Continuous Observation of the Coupling Of a Single Atom to the Resonator	22
2.1	Nondestructive State Detection - Schematic	24
2.2	Single Quantum Jumps and Ensemble Average	26
2.3	Illustration of Poissonian Detection Noise	27
2.4	Transmission Level and Jump Time versus Cavity-Atom Detuning	28
2.5	State Detection Error Probability versus Photon Number	29
2.6	One-Atom Random Telegraph Signals	31
2.7	Relative Frequency Distribution of Photon Counts from One-Atom Random Telegraph Signals	32
2.8	Histograms of Dwell Times for One Atom Quantum Jumps	33
2.9	Second Order Intensity Auto-Correlation Function of One-Atom Random Telegraph Signals	34
2.10	Second Order Auto-Correlation Function of Quantum Jumps and Sub-Poissonian Jump Distribution	36
2.11	One- and Two-Atom Transmission Level Difference	38
2.12	Transmission Level for One and Two Atoms Coupled to the Resonator as a Function of Cavity-Atom Detuning	39
2.13	Two-Atom Quantum Jumps	41
2.14	Jump Time versus Photon Number	42

2.15	Ensemble Average of Two-Atom Quantum Jump Traces Without Repumper	43
2.16	Random Telegraph Signal for Two Atoms in the Resonator	46
2.17	Averaged Dynamical Probabilities and Photon Count Histogram for Two-Atom Random Telegraph Signals at $\Delta_{ca} = 2\pi \times 38$ MHz	47
2.18	Intensity Auto-Correlation Function of Digitized Two Atom Telegraph Signals	48
2.19	Averaged Dynamical Probabilities and Photon Count Histogram for Two-Atom Random Telegraph Signals at $\Delta_{ca} = 2\pi \times 280$ MHz	49
3.1	Schematic Signal Distribution in an Atom Number Measurement	54
3.2	Sketch of a Homodyne Phase Detector	57
3.3	Fidelity and Signal Distribution for Homodyne Detection	59
3.4	Fidelity versus Success Probability	60
A.1	State Changing Inelastic Raman Transitions	65
B.1	Average Intensity Auto-Correlation Function of Ideal Two-Atom Telegraph Signals	69

Introduction - Measuring the Quantum

Imagine someone wants to buy new furniture for his living room. Before driving to the home-center he measures length and width of the room. When he comes back with a sofa and a cupboard, carefully selected according to the room size he measured, he realizes that they do not fit in. Baffled he drives back to the home-center to get smaller furniture. But strangely, now the room is much larger than he measured. Sofa and cupboard are too small.

While this situation seems rather far-fetched as far as everyday life is concerned, in modern quantum physics similar situations commonly appear in the lab. The objects and their properties that are measured are so fragile, that the slightest disturbance by a measurement apparatus changes the measured property. One way to tackle this problem is to prepare many identical copies of the system under investigation. By measuring one copy, one knows the properties of all other copies without disturbing them. The preparation of many copies is, however, often time consuming. Sometimes it is even impossible, because the measurement is in fact necessary to verify the successful preparation of the desired state. The best way to avoid destroying the measured object is to minimize the disturbance by the measurement.

Such a nondestructive measurement is the subject of this thesis. The property to be measured is the total angular momentum F of a caesium atom. For the ground state of caesium F can take only the two values 3 and 4, corresponding to the two hyperfine ground states $|F = 3\rangle$ and $|F = 4\rangle$. Due to their long life time they are well suited as carriers of quantum information, e.g. $|F = 3\rangle$ encoding a binary 0 and $|F = 4\rangle$ encoding a binary 1. Retrieving information encoded in this way, obviously requires a measurement of F , which ideally should be fast and nondestructive. The measurement investigated here is based on what might be called the state dependent refractive index of the atom: An atom driven by a laser beam with a frequency close to one of the atom's transition frequencies induces a phaseshift on the laser light, just like a piece of glass does. For a caesium atom this phaseshift depends on its angular momentum state $|F\rangle$. Thus, F can be measured via this refractive index effect. The good thing about this measurement is that it does in principle not change the measured observable F . The bad thing is that for a single atom in free space, the state dependent phaseshift is far too small to be measured by any existing detector.

One way to enhance the phaseshift is to use many atoms. This has recently been done in the group of E. Polzik in Copenhagen [1], where the nondestructive observation of Rabi oscillations between the states $|F = 3\rangle$ and $|F = 4\rangle$ has been reported. While the nondestructive probing of large atomic ensembles is particularly useful for precision metrology, it cannot be used for quantum information purposes, where the manipulation and readout of single quantum systems is required.

Instead of using many atoms to increase the phase shift, one can as well make the light pass

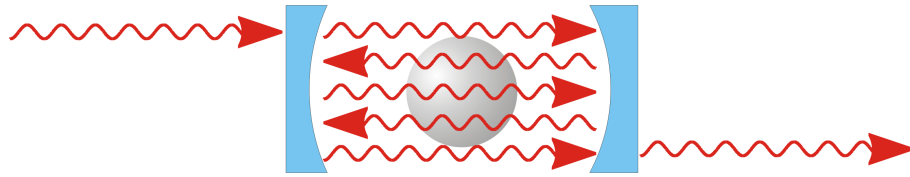


Figure 0.1: Schematic sketch of atom-light interaction inside a Fabry-Perot resonator. The light is reflected back and forth between the two mirrors and interacts with the atom many times before it exits the interferometer.

by a single atom many times so that the resulting phaseshift is as large as if many atoms had interacted with the light. This can be done by placing the atom between the two mirrors of a Fabry-Perot resonator (see fig. 0.1). Light circulating in the resonator interacts with the atom on each path between the two mirrors. This strongly enhances the strength of the atom-light interaction. Loosely speaking, if the light does 1 million round trips in the interferometer, the effect of a single atom on the light is as strong as if it would interact with 2 million atoms in free space. Conversely, already a single photon in the interferometer interacts with the atom as strongly as millions of photons in free space.

The nondestructive detection of the hyperfine state of a single atom in a high quality Fabry-Perot resonator via the atom-induced phase shift has first been used in the group of H. J. Kimble at the California Institute of Technology [2]. In this thesis I present the investigation of quantum jumps between the hyperfine ground states of a single caesium atom, based on this measurement technique. Apart from single-atom experiments, our setup allows to couple two atoms simultaneously to the resonator field in a controlled way and observe their internal state dynamics. Experiments that investigate quantum jumps of one *and two* atoms in the resonator are presented in chapter 2. The state measurement via the atom-induced phaseshift in principle allows not only to measure the state without changing it, but even without scattering a single photon. Applied to two atoms, this should allow generating two-atom entangled states [3]. In chapter 3 I theoretically analyze the entanglement scheme presented in [3] for our experimental conditions and estimate the entanglement fidelity that can be achieved with our setup. The state detection scheme outlined above measures the atomic state via the phaseshift imprinted on a probe laser beam. To achieve fast and efficient detection with the least possible photon scattering it is thus crucial to optimize the efficiency of the light detection. A large part of my Diploma work was dedicated to improving the efficiency of the detection of the photons transmitted through the resonator. The optimized detection setup is presented in the second part of chapter 1. Before describing the experiment, I will outline the basic theoretical framework, describing the interaction between atoms and light in a high quality resonator. This is done in the first part of chapter 1.

1 Strong Coupling of Atoms and Photons Inside a High Finesse Optical Resonator

This chapter provides the theoretical and experimental background necessary to understand the experiments and calculations presented in chapters 2 and 3. In the first section I present a basic theoretical description of atom-light interaction in an optical resonator. In the second section I describe the experimental setup used for the measurements in chapter 2 with a focus on the improved photon detection setup.

1.1 Theoretical Description of Atom-Light Interaction in a Resonator

The theoretical framework describing the interaction between atoms and light in a resonator is called cavity QED or CQED, which is short for cavity quantum electrodynamics. A cavity QED setup as studied in the laboratory really has two different facets: On the one hand, there is the interaction between the atom and the cavity light field, which is the object of investigation in most of today's cavity QED experiments. This interaction is a *reversible* and *coherent* process governed by Schrödinger's equation. On the other hand, atom and resonator light field interact with the environment: The atom can decay from its excited state and emit a photon into modes other than the cavity mode. The cavity light field can decay due to losses of the cavity mirrors. The energy transferred to the environment is forever lost from the atom-cavity system. Thus, the interaction with the environment is *dissipative*, i.e. *incoherent*.

1.1.1 Coherent Atom-Light Interaction - The Jaynes-Cummings Model

The strongest interaction between an atom and light is the electric dipole interaction. It is described by the Hamiltonian

$$\hat{\mathcal{H}}_{\text{dip}} = \hat{\mathbf{d}} \cdot \hat{\mathbf{E}}(\mathbf{r}). \quad (1.1)$$

If only one ground state $|g\rangle$ and one excited state $|e\rangle$ of the atom and one mode of the light field described by the annihilation operator \hat{c} are relevant, the dipole interaction Hamiltonian in the Heisenberg picture simplifies to [4]

$$\hat{\mathcal{H}}_{\text{dip}} = \hbar g(\mathbf{r}) (\hat{\sigma}^\dagger \hat{c} + \hat{\sigma} \hat{c}^\dagger). \quad (1.2)$$

Here, the atom-light coupling strength $g(\mathbf{r})$ and the atomic lowering operator $\sigma = |g\rangle\langle e|$ have been introduced. Due to the spatial mode profile of the light field, the coupling strength is position dependent. It is given by

$$g(\mathbf{r}) = \frac{d}{\hbar} \sqrt{\frac{\hbar\omega_c}{2\epsilon_0 V}} M(\mathbf{r}). \quad (1.3)$$

The function $M(\mathbf{r})$ describes the spatial mode profile. It is normalized to unity at the field maxima. ω_c denotes the angular frequency of the light and ϵ_0 the permittivity of the vacuum. The only experimentally tunable parameter in eq. (1.3) is the mode Volume V . In order to achieve strong atom-light coupling it is thus desirable to use a cavity, e.g. a Fabry-Perot resonator, to confine the light to a small mode volume. This is what is done in cavity QED experiments. In the following, I will always consider the field \hat{c} to be confined by a resonator. And I will call \hat{c} the cavity field.

The structure of the interaction Hamiltonian (1.2) has a quite intuitive interpretation: Due to the atom-light coupling, a photon can be annihilated from the cavity mode (\hat{c}), if in turn the atom is transferred to the excited state ($\hat{\sigma}^\dagger$). Or the other way around, the atom can emit its excitation energy into the cavity mode ($\hat{\sigma}$), where consequently a photon is created (\hat{c}^\dagger). Through these processes, energy is *exchanged* between atom and resonator field, but it can never get lost from the system.

Apart from the dipole interaction Hamiltonian, the total Hamilton operator of a coupled atom-cavity system comprises contributions of the unperturbed atom and light field

$$\hat{\mathcal{H}}_a = \hbar\omega_a \hat{\sigma}^\dagger \hat{\sigma}, \quad \hat{\mathcal{H}}_c = \hbar\omega_c \left(\hat{c}^\dagger \hat{c} + \frac{1}{2} \right). \quad (1.4)$$

Here, ω_a is the resonance frequency of the atomic transition. Note that the cavity Hamiltonian \mathcal{H}_c has the same form as that of a quantum mechanical harmonic oscillator. Using eqs. (1.1) and (1.4) the total Hamiltonian, describing a lossless atom-cavity system is given by

$$\begin{aligned} \hat{\mathcal{H}}_{\text{JC}} &= \hat{\mathcal{H}}_a + \hat{\mathcal{H}}_c + \hat{\mathcal{H}}_{\text{dip}} \\ &= \hbar\omega_a \hat{\sigma}^\dagger \hat{\sigma} + \hbar\omega_c \left(\hat{c}^\dagger \hat{c} + \frac{1}{2} \right) + \hbar g (\hat{\sigma}^\dagger \hat{c} + \hat{\sigma} \hat{c}^\dagger). \end{aligned} \quad (1.5)$$

This Hamilton operator was first studied by Jaynes and Cummings [5] and has since become a standard model of atom-light interaction, due to its rather general applicability [6]. If the cavity is tuned in resonance with the atomic transition ($\omega_a = \omega_c = \omega$), the Jaynes-Cummings Hamiltonian can be diagonalized exactly. Its eigenstates and eigenenergies are

$$|n_\pm\rangle = \frac{1}{\sqrt{2}} (|g\rangle \otimes |n\rangle \pm |e\rangle \otimes |n-1\rangle), \quad E_{n,\pm} = n\hbar\omega \pm \hbar g \sqrt{n}. \quad (1.6)$$

Because of equal resonance frequencies of atom and cavity, the eigenstates are superpositions of the unperturbed eigenstates of atom and cavity light field. If there were no atom-light

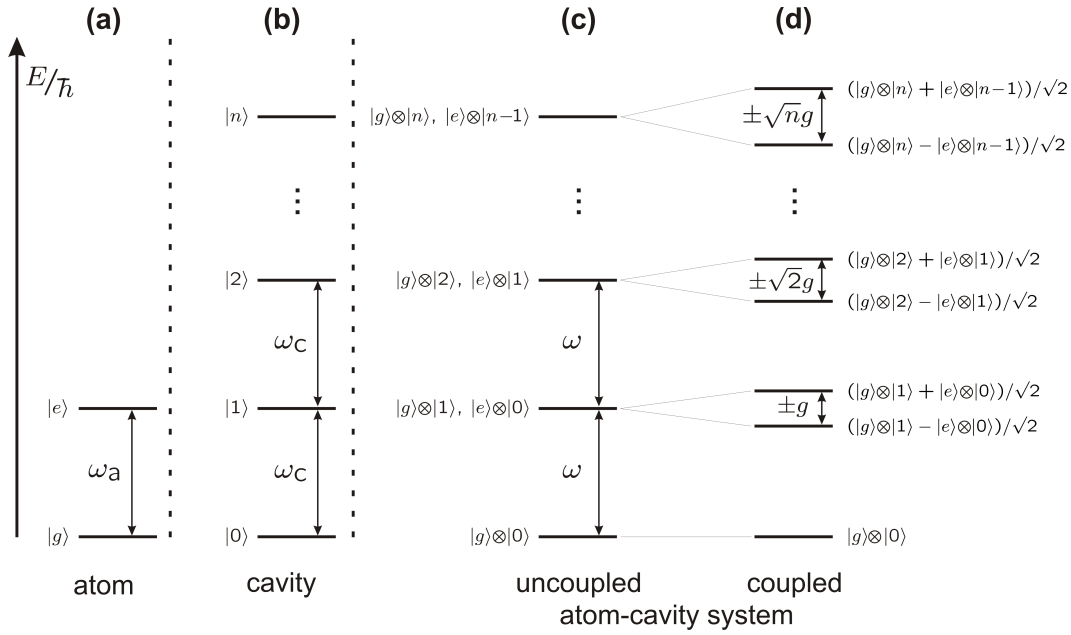


Figure 1.1: Energy spectrum of (a) the unperturbed atom, (b) the empty cavity mode, (c) the uncoupled atom-cavity system, and (d) the coupled atom-cavity system described by the Jaynes-Cummings Hamiltonian.

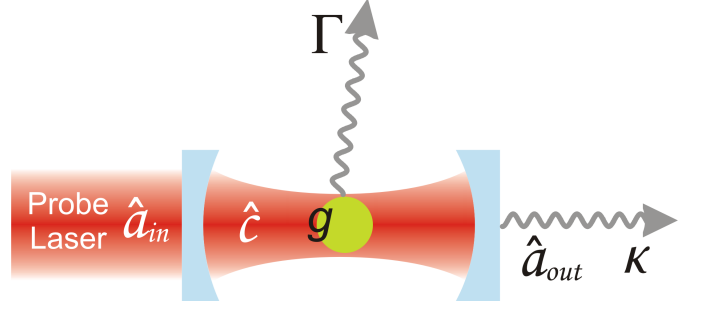
interaction, the total energy of the system would be the same, no matter how it were distributed between atom and cavity ($E(g, n) = E(e, n - 1)$). This degeneracy is lifted due to the interaction between atom and light field. This is graphically illustrated in fig. 1.1. The splitting of the states $|1_{\pm}\rangle$ of $2g$ is called normal mode splitting in analogy to the frequency splitting between the in-phase and out-of-phase modes of two coupled mechanical oscillators. If the coupled atom-light system is initially not in one of its eigenstates $|n_{\pm}\rangle$, but is prepared for example in the state $|e\rangle \otimes |0\rangle$, the solution of the time-dependent Schrödinger equation shows that the system oscillates between the states $|e\rangle \otimes |0\rangle$ and $|g\rangle \otimes |1\rangle$ with a fixed phase. The frequency of these oscillations is $2g$. This illustrates why the atom-light interaction described by the Jaynes-Cummings Hamiltonian is called *coherent*.

Up to here all considerations have assumed a *closed* interacting atom-light system. This assumption is invalid for any experimental setting. Not only are energy losses an unavoidable problem, they are even necessary for doing experiments at all: If the system under investigation were completely isolated from the environment, no information on the system's state could be obtained. The general framework in which the interaction between an atom-cavity system and its environment is treated will be given in the next section.

1.1.2 Decoherence via Dissipation - The Master Equation

To fully treat the interaction between atom, cavity light field, and environment, in principle one would have to diagonalize the full Hamiltonian including the environment. In an experiment, however, the state of the environment is rather not relevant, since it cannot be measured. All

Figure 1.2: Schematic of a Cavity QED system. The interaction between atom and cavity field with the coupling strength g leads to coherent energy exchange. This coherent energy exchange is damped by spontaneous emission of the atom with a rate Γ and the decay of the cavity field with a rate κ .



the information that can be obtained from observables acting solely on the investigated system is contained in the so-called reduced density matrix

$$\hat{\rho}_S = \text{tr}_E(\hat{\rho}_{SE}). \quad (1.7)$$

tr_E denotes the trace operation on the environmental degrees of freedom. $\hat{\rho}_{SE}$ is the density matrix of the combined system and environment. The part of the environment that most strongly interacts with atom and resonator light field are the other modes of the electromagnetic field, which are not confined by the cavity. They constitute a bath of harmonic oscillators. It turns out that for this specific type of environment the following equation of motion for the reduced density matrix $\hat{\rho}_S$ can be found [7]:

$$\begin{aligned} \frac{d\hat{\rho}_S}{dt} = & \frac{1}{i\hbar} [\hat{\mathcal{H}}_{JC}, \hat{\rho}_S] + \kappa (2\hat{c}\hat{\rho}_S\hat{c}^\dagger - \hat{c}^\dagger\hat{c}\hat{\rho}_S - \hat{\rho}_S\hat{c}^\dagger\hat{c}) \\ & + \frac{\Gamma}{2} (2\hat{\sigma}\hat{\rho}_S\hat{\sigma}^\dagger - \hat{\sigma}^\dagger\hat{\sigma}\hat{\rho}_S - \hat{\rho}_S\hat{\sigma}^\dagger\hat{\sigma}) \end{aligned} \quad (1.8)$$

Here, Γ is decay rate of the atomic excited state, corresponding to the FWHM of the atomic emission spectrum. κ is the cavity field decay rate, corresponding to the HWHM of the cavity transmission spectrum. This equation of motion for the reduced density matrix is called *master equation*. Not only does it allow to model energy dissipation by the environment, but also the driving by an externally applied field, such as that of a probe laser which is sent through the resonator in a spectroscopy experiment. The driving is modeled by an additional term in the Hamiltonian. The total Hamiltonian is then most conveniently expressed in a frame rotating at frequency ω_p of the probe laser driving field [7]. It reads

$$\hat{\mathcal{H}} = \hat{\mathcal{H}}_{JC,p} + \hbar\sqrt{\kappa\Phi_{ph}} (\hat{c} + \hat{c}^\dagger). \quad (1.9)$$

Φ_{ph} denotes the flux of photons impinging on the cavity incoupling mirror and $\hat{\mathcal{H}}_{JC,p}$ is the Jaynes-Cummings Hamiltonian in the rotating frame of the driving field. From the master eq. (1.8) one can derive equations of motion for the operators $\hat{\sigma}$ and \hat{c} . If the driving is weak, so that the intra cavity photon number $\langle \hat{c}^\dagger\hat{c} \rangle \ll 1$, these equations of motion can be solved analytically. One finds the following relation between the input driving field \hat{a}_{in} and the transmitted cavity output field \hat{a}_{out} [3, 8]:

$$\hat{a}_{out}(\Delta_{pc}, \Delta_{ca}; g) = \frac{\kappa}{i\Delta_{pc} - \kappa - \frac{|g|^2}{\gamma - i(\Delta_{ca} + \Delta_{pc})}} \eta_{cav} \hat{a}_{in} \quad (1.10)$$

Here the cavity-atom detuning $\Delta_{ca} = \omega_c - \omega_a$ and the detuning between probe laser frequency and cavity frequency $\Delta_{pc} = \omega_p - \omega_c$ have been introduced, as well as the on-resonance empty cavity transmission coefficient η_{cav} . An ideal resonator without absorption and diffraction losses ($R + T = 1$) is completely transparent on resonance ($\eta_{cav} = 1$). Finite absorption losses reduce this value. Multiplying each side of eq. (1.10) by its hermitian conjugate, one finds the following formula for the transmission level, i.e. the number of transmitted photons $\langle \hat{n}_{out} \rangle (\Delta_{pc}, \Delta_{ca}; g)$ normalized to the empty cavity on-resonance transmission $\langle \hat{n}_{out} \rangle (0, 0; 0) = \eta_{cav}^2 \langle \hat{n}_{in} \rangle$:

$$\text{TL}(\Delta_{pc}, \Delta_{ca}; g) = \frac{\langle \hat{n}_{out} \rangle (\Delta_{pc}, \Delta_{ca}; g)}{\eta_{cav}^2 \langle \hat{n}_{in} \rangle} = \kappa^2 \left[\left(\kappa + \frac{2|g|^2 \Gamma}{\Gamma^2 + 2(\Delta_{ca} + \Delta_{pc})^2} \right)^2 + \left(\Delta_{pc} - \frac{2|g|^2 (\Delta_{ca} + \Delta_{pc})}{\Gamma^2 + 2(\Delta_{ca} + \Delta_{pc})^2} \right)^2 \right]^{-1} \quad (1.11)$$

This relation is especially important, since the average photon number in the cavity output field $\langle \hat{n}_{out} \rangle$ is the observable that is most easily accessible in experiments. Figure 1.3 depicts the transmission level as a function of the detunings Δ_{ca} and Δ_{pc} . The two lines, where a nonzero transmission is observed are associated with the excitation of the first two dressed states $|1_{\pm}\rangle$ of the Jaynes-Cummings spectrum given by eq. (1.6). The finite width of the transmission lines is due to energy dissipation by the environment. On the horizontal solid line the probe laser is in resonance with the empty cavity. On the diagonal line, the probe laser is in resonance with the undisturbed atomic transition. The fact that the transmission lines associated with the dressed states adapt to these solid lines in the limit of very large detunings, means that in this limit the atom-light coupling acts only as a slight perturbation on the uncoupled systems. As the dressed states become more and more atom-like, the transmission fades, while it is strong in the cavity-like regions. This is due to the fact that the probe laser drives the cavity mode and not the atom.

In the dissipation free Jaynes-Cummings model the system oscillates between the states $|e\rangle \otimes |0\rangle$ and $|g\rangle \otimes |1\rangle$, if it is initially prepared in one of these states. Due to the interaction with the environment, the excitation decays, leading to a damping of these oscillations. This damping process is called decoherence as opposed to the coherent oscillations predicted by the dissipation free Jaynes-Cummings model. If the frequency of the coherent oscillations, given by two times the coupling strength g , is much larger than the damping rates κ and Γ , the coherent coupling dominates over the dissipation. This regime where $g \gg \kappa, \Gamma$ is called the *strong coupling regime*.

The theory described above becomes in principle much more difficult as soon as more than a single atom is interacting with the resonator light field. However, it turns out that eqs. (1.10) and (1.11) are still valid if $|g|^2$ is replaced by [8]

$$|g_{tot}|^2 = \sum_i |g_i|^2, \quad (1.12)$$

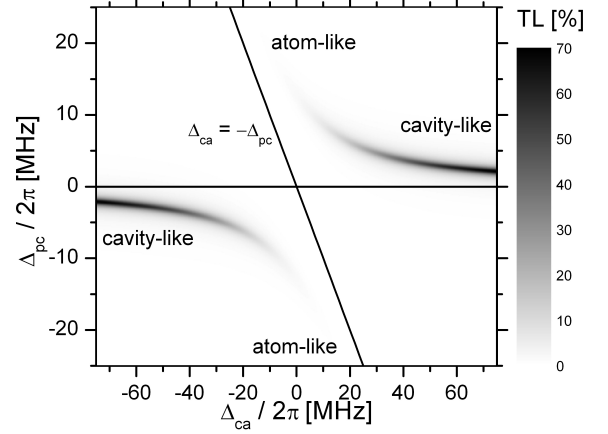


Figure 1.3: Cavity transmission as a function of cavity-atom detuning and probe-cavity detuning, plotted according to eq. (1.11). In the far-detuned regions, the dressed states exhibit cavity-like or atom-like characteristics.

where g_i are the coupling strengths of the individual atoms.

If the cavity is detuned from the atomic resonance by a few atomic linewidths or more, the effect of the atom is rather similar to that of a medium with a refractive index. Assuming that $\Delta_{ca} \gg \Gamma$, eq. (1.11) simplifies to

$$\text{TL} = \frac{\kappa^2}{\kappa^2 + \left(\Delta_{pc} - \frac{|g|^2}{\Delta_{ca}}\right)^2}. \quad (1.13)$$

Thus, in the dispersive limit, where $\Delta_{ca} \gg \Gamma$, the atom-light interaction leaves the shape of the Lorentzian cavity transmission spectrum unchanged. Only the resonance frequency ω_c is shifted to $\omega'_c = \omega_c + g^2/\Delta_{ca}$.

Avoiding spontaneous scattering as good as possible will be important for the nondestructive state measurement presented in chapter 2 and is even crucial if this measurement is to be used for the generation of entangled states as will be discussed in chapter 3. Naively, it could be suspected that in the dispersive regime the rate of spontaneous photon scattering decreases drastically as it is the case in free space. However, as Δ_{ca} increases, also the cavity transmission level increases. And so does the intra cavity photon number. The spontaneous scattering rate in the resonator is given by:

$$R_{\text{scat}} = \frac{\Gamma |g|^2}{\Gamma^2/4 + \Delta_{ca}^2} \langle \hat{c}^\dagger \hat{c} \rangle \quad (1.14)$$

Using eq. (1.11) and the relation $\langle \hat{c}^\dagger \hat{c} \rangle = \langle \hat{n}_{\text{out}} \rangle / \kappa$, one finds

$$R_{\text{scat}} = \frac{4 |g|^2 / \kappa \Gamma}{1 + 4 (|g|^2 / \kappa \Gamma)^2 + (|g|^2 / \kappa \Delta_{ca})^2 + (\Delta_{ca} / \Gamma)^2} \langle \hat{n}_{\text{out}} \rangle. \quad (1.15)$$

Obviously, the scattering rate decreases only with Δ_{ca} , if the last term in the denominator dominates. As long as $\Delta_{ca} > |g|^2 \Gamma / \kappa$ the scattering rate increases with Δ_{ca} , due to the third

term in the denominator.

After the theoretical principles of atom-light interaction have now been outlined, the next section will describe how controlled strong coupling between single caesium atoms and the field of a high quality optical resonator is achieved in our experiment.

1.2 Experimental Implementation of a CQED System in the Strong Coupling Regime

Implementing strong coupling between a single atom and a cavity field in the first place requires a high quality resonator with a low field decay rate κ and a small mode volume to achieve a high coupling strength according to eq. (1.3). Having such a resonator, it is then important to position a single atom precisely at the field maximum of the resonator mode. I will first describe the existing setup that allows to trap and cool single caesium atoms and insert them in a controlled way into the resonator. The characteristics of the Fabry-Perot resonator used in our experiment are described in section 1.2.2, and measurements of the most important cavity properties are presented. In order to retrieve information on the coupled atom-cavity system, the photons from a probe laser transmitted through the resonator have to be detected. The photon detection setup that I have optimized during my thesis work is presented in section 1.2.3.

1.2.1 Preparation of Cold Atoms and Transport into the Resonator

The experimental setup for the preparation and transport of single caesium atoms has been built several years ago and is extensively described and characterized in references [9–12]. A schematic of the setup is shown in fig. 1.4. The experiments take place in an ultra high vacuum glass cell, connected to a caesium reservoir. Caesium atoms are loaded from the background gas into a magneto optical trap (MOT). Due to a rather high magnetic field gradient of 300 G/cm, the trap diameter is only 10 μm so that only few atoms are trapped in the MOT. The number of atoms loaded on average can be controlled by adjusting the MOT loading time. For loading times between 5 and 500 ms the average atom number can be adjusted between 1 and 50. The fluorescence of the atoms is collected with a high numerical aperture objective [13]. Half of the collected light is detected on a single photon counting module (SPCM) (EG&G SPCM-200). The other half is directed onto the chip of an intensified charge-coupled device (ICCD camera) (Roper Scientific, PIMAX: 1K). The number of atoms in the MOT can be determined from the number of fluorescence photons detected by the SPCM. In order to experiment with an exactly determined number of atoms, the MOT is reloaded until the fluorescence counts correspond to the desired atom number.

From the MOT the atoms are transferred into a red detuned, far off-resonant one dimensional optical lattice. The lattice is produced by two counterpropagating beams of an Yb:YAG laser

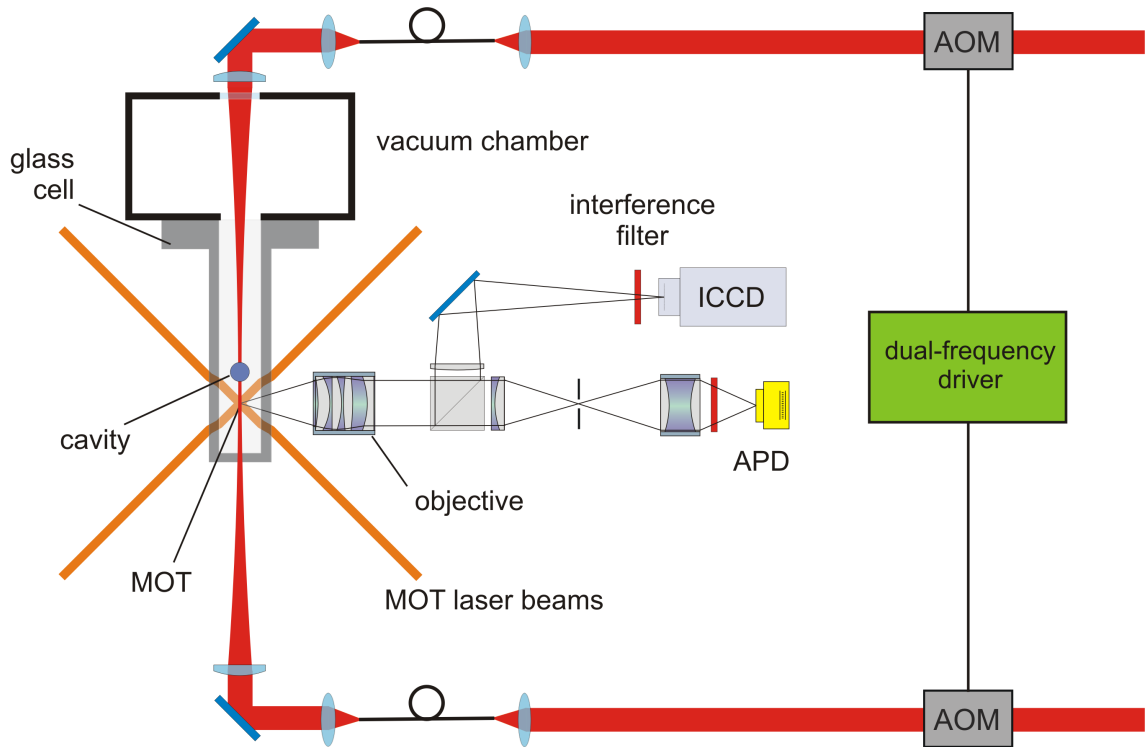


Figure 1.4: Experimental setup of MOT and optical lattice. Single atoms are trapped in a high gradient MOT and are transferred into a one dimensional optical lattice. The number of atoms in the MOT is measured via fluorescence detection on a SPCM. The atomic position in the lattice is determined of the fluorescence image of the atom, taken with an ICCD camera. Two AOMs and a dual frequency driver allow to move the optical lattice and thereby transport the atoms.

(ELS VersaDisk-1030-10-SF) operating at a wavelength of 1030 nm and an output power of 23 W. The typical power in each beam in the glass cell is 1.8 W. The beams are focused to a waist of $w_{0,OL} = 39 \mu\text{m}$. The position of the atoms in the optical lattice is determined by illuminating them with the MOT molasses beams and imaging their fluorescence onto the chip of the ICCD camera. A typical image obtained for two atoms in the lattice is depicted in fig. 1.5. The resolution of the imaging system is $1.8 \mu\text{m}$ corresponding to the diffraction limit of the imaging objective [13]. To determine the horizontal positions of the atoms relative to the camera, the counts of the ICCD chip are binned along the vertical direction of the image over a predetermined region of interest indicated by the red lines in fig. 1.5. A Gaussian distribution is then fitted to the resulting peaks in the count histogram.

In the optical lattice, the atoms can be transported over a distance of several millimeters with high precision. This is done with the help of two acousto optic modulators (AOMs) and a dual frequency driver, allowing to sweep the phase of the two lattice beams with respect to each other by an arbitrary amount. This phase sweep results in a shift of the optical lattice. Since the atoms are drawn to the intensity maxima by the dipole force, they are dragged along with the lattice. The lattice acts like a conveyor belt that transports the atoms to an arbitrary

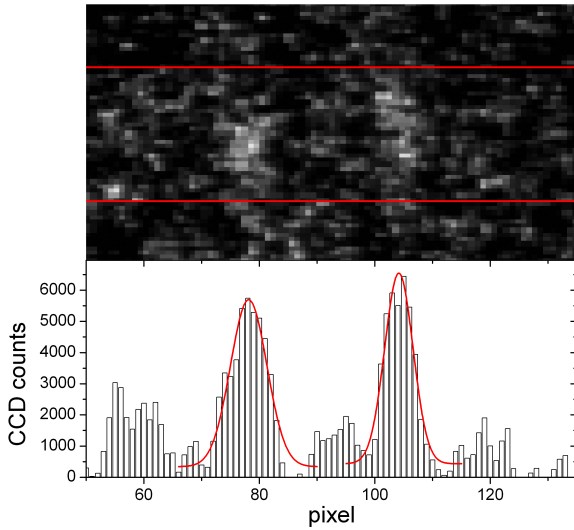


Figure 1.5: ICCD image of two caesium atoms trapped in the optical lattice. To determine the position of each atom relative to the camera, the counts of the ICCD pixels are binned along the vertical direction of the image over a predetermined region of interest (red lines). The peaks in the resulting histogram are fitted with a Gaussian.

position (for details see [12]). The precision of the transport is 300 nm, limited by the accuracy of the position detection and by phase drifts of the optical lattice beams.

Altogether, MOT, optical lattice, atom counting and imaging, and the transport mechanism enable us to prepare a predetermined number of caesium atoms and transport them into our high quality optical resonator, which shall be described in the following.

1.2.2 Characteristics of the High Finesse Resonator and Resonator Stabilization

A schematic and a photograph of our cavity are shown in fig. 1.6. It is a Fabry-Perot type resonator, consisting of two highly reflective mirrors facing each other. Each mirror is glued onto a shear piezo electric transducer, allowing to control and stabilize the resonator length. The optical lattice beams traverse the resonator and provide the means to bring the atoms from the MOT into the cavity. The focus of the lattice beams is at a distance of 3 mm from the MOT. The cavity mirrors have been produced by the company Research Electro-Optics Inc. in close cooperation with a PhD student from our lab. The characterization of the mirrors, the resonator assembly, and its integration into the cold atom setup is described in detail in his thesis [12]. The mirrors have a radius of curvature of 5 cm. The length of the resonator is $156.3 \mu\text{m}$ corresponding to a free spectral range of $\omega_{\text{FSR}} = 2\pi \times c/2L = 2\pi \times 958 \text{ GHz}$. This yields a waist size of the cavity's TEM_{00} mode of $23.15 \mu\text{m}$. The key parameter of the resonator is its transmission linewidth κ (HWHM). It can be measured by directly observing the decay of the resonator light field. Shortly after implementation of the resonator in the cold atoms setup the linewidth was measured to be $\kappa = 2\pi \times 0.43 \text{ MHz}$. In order to check for changes of the cavity parameters we have remeasured the linewidth again in the winter of 2008, about two years after the first measurement.

The measurement is done as follows: The resonator length is locked by means of a stabi-

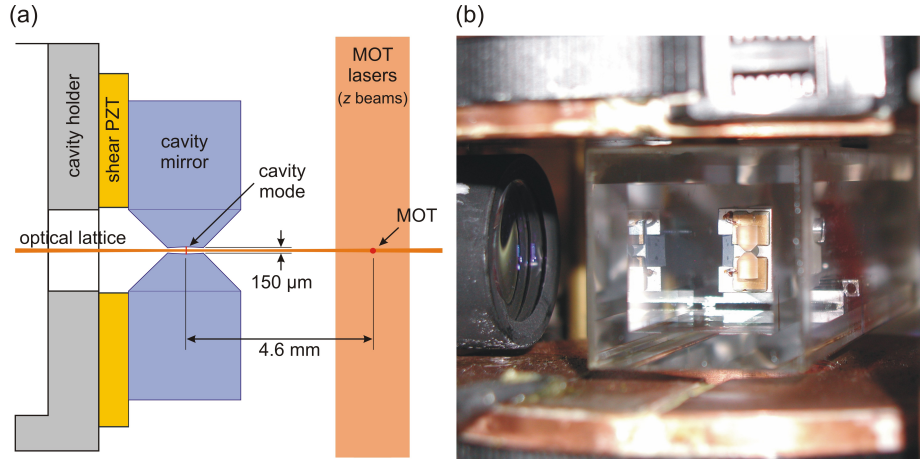


Figure 1.6: (a): True to scale sketch of the cavity setup. The resonator mirrors are glued to shear piezo electric transducers for active stabilization of the cavity length. The optical lattice beams traverse the resonator and are used to transport atoms from the MOT to the resonator over a distance of 4.6 mm. (b): Photograph of the cavity in the vacuum glass cell.

lization laser. A probe laser is applied on resonance with the cavity and the transmitted light is detected on a fast, analog avalanche photo diode (APD).¹ The probe laser is then switched off by means of an AOM and the decay of the transmitted intensity as measured on the APD is recorded with a digital oscilloscope. To reduce the noise, the signal is averaged over several hundred single measurements. The obtained exponential decay is shown as a black line in fig. 1.7. To ensure that the finite detector bandwidth due to AOM switching time and APD bandwidth does not disturb the measurement, the APD is positioned directly behind the AOM without the cavity in between. The measured signal for this configuration is shown as a blue line in fig. 1.7. It can be seen that about 100 ns after switching off the AOM, the intensity has decayed completely to zero for the measurement without resonator. In order to extract the time constant of the cavity decay, an exponential is fitted to the signal measured *with* resonator. For the fit only the data to the right of the dashed line, i.e. for times longer than the detector dead time, is taken into account. In this way, a systematic error due to the finite detector bandwidth is avoided. Upon close inspection of the cavity decay it can be seen that a sinusoidal oscillation is superimposed on the exponential decay. This is due to a beating of two polarization modes of the resonator (see below). To average out these oscillations, I varied the starting point of the exponential fit over one oscillation period and averaged the resulting decay constants. The resulting value for the cavity linewidth is

$$\kappa = (0.40^{+0.03}_{-0.02}) \text{ MHz}. \quad (1.16)$$

The errors are taken as the deviation of the minimum and maximum fitted values from the average. The linewidth depends not only on the reflectivity of the resonator mirrors, but also on the length of the cavity. The longer the cavity, the longer the round trip time of the light

¹The details of the resonator stabilization and the detection setup are presented below.

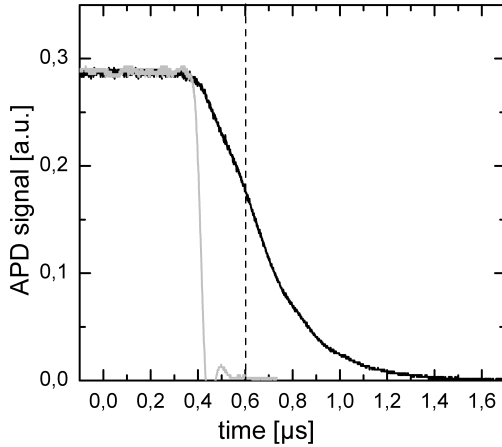


Figure 1.7: Decay of the intensity leaking from the cavity after the probe laser has been switched off (black line). The decay constant corresponds to the cavity linewidth. The switching time of the AOM and the APD deadtime are much shorter than the cavity decay. This is confirmed by the APD signal measured without cavity (gray line).

in the resonator. And since only twice per round trip a photon can escape from the cavity, the decay time increases with the length of the cavity. A quantity that characterizes solely the cavity mirrors is the finesse. It is defined as

$$\mathcal{F} = \frac{\pi\sqrt{R}}{1-R} \stackrel{R \approx 1}{\approx} \frac{\pi}{T+A}. \quad (1.17)$$

Here, R , T , and A are the reflection, transmission and absorption coefficients of the mirrors. They are assumed to be identical for both mirrors. In eq. (1.17) the relation $R + T + A = 1$ has been used. The finesse is connected to the resonator linewidth via

$$\mathcal{F} = \frac{c\pi}{2L\kappa}. \quad (1.18)$$

The measured linewidth of $\kappa = 0.4$ MHz together with the resonator length of $156.3 \mu\text{m}$ corresponds a finesse and reflectivity of

$$\mathcal{F} = (1.2 \pm 0.1) \cdot 10^6 \Leftrightarrow R = 1 - (T + A) = 1 - (2.6 \pm 0.2) \text{ ppm}. \quad (1.19)$$

To our knowledge this is the highest Finesse of an optical Fabry-Perot resonator that has ever been reported.

A slight birefringence in the dielectric coatings of the cavity mirrors causes a difference in the cavity lengths for the two linear polarizations defined by the birefringence. This results in a difference of the resonance frequencies for the two polarizations of $\Delta\omega_{\text{br}} = 2\pi \times 3.86$ MHz [12]. Since this splitting is significantly larger than κ , only linearly polarized light can be coupled into the resonator. This has consequences for the maximally achievable coupling strength as will be explained in section 1.2.4.

Controlling the interaction between the light field of such a narrow linewidth resonator and caesium atoms requires a sophisticated scheme for the stabilization of the resonator frequency. The resonator frequency has to be stable relative to the desired caesium resonance. The laser used for the stabilization should, however, be far detuned from any caesium resonance in order

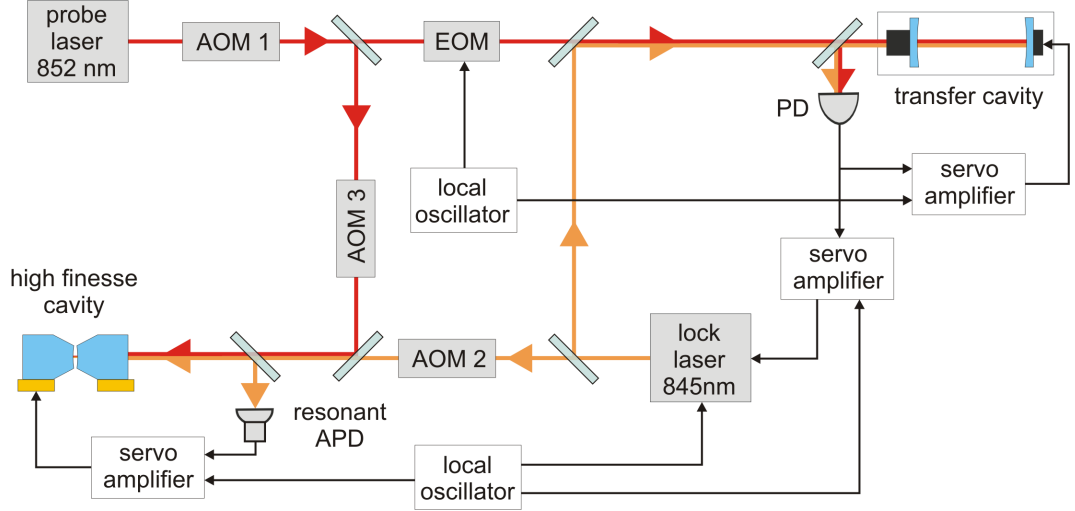


Figure 1.8: Schematic of the cavity stabilization setup. All cavity locks are implemented with the PDH method. The lock laser is stabilized onto a transfer cavity, which before has been stabilized to the caesium-locked probe laser. In this way the stability of the caesium transition at 852 nm is transferred to the lock laser operating at 845 nm. This lock laser is used to stabilize the QED cavity. In this way the QED cavity is stabilized relative to the caesium transition with a laser that only weakly interacts with the atoms in the cavity.

not to disturb the interaction between atom and cavity field. This gives rise to the need for a *transfer cavity*, i.e. a low finesse resonator with a small free spectral range that allows to transfer the stability of the caesium-locked probe laser to a so-called lock laser at a different wavelength. This lock laser is then used to stabilize the QED cavity. The basic principle of the locking scheme is as follows: The probe laser, which is used to probe the coupled atom-cavity system, is stabilized onto the $|F = 4\rangle \rightarrow |F' = 3/5\rangle$ crossover transition of the caesium D_2 -Line. The transfer cavity is then stabilized onto the caesium stabilized probe laser, using the Pound-Drever-Hall (PDH) method [14]. In a third step, the lock laser operating at 845 nm is locked onto the transfer cavity, again with the PDH method. In this way it is also stabilized with respect to the caesium transition. As a last step, the QED cavity is stabilized with a third PDH lock onto the lock laser. For technical details of the stabilization setup see [15].

Apart from stabilizing the QED cavity, the lock laser has a second purpose. It helps to control the position of the atoms in the resonator. The laser configuration in the resonator is shown in fig. 1.9. According to the mode shape of the Fabry-Perot resonator, the atom-cavity coupling strength has approximately the following spatial profile:

$$g(\mathbf{r}) = g_{max} \sin\left(\frac{2\pi z}{\lambda}\right) \exp\left(-\frac{x^2 + y^2}{w_{0,cav}^2}\right) \quad (1.20)$$

The variation of the radial width of the mode is neglected, because the resonator length is well below the Rayleigh range of the cavity mode. The maximum coupling strength is achieved at the anti-nodes of the probe laser standing wave. Before the atoms are transported into the cavity by the moving Yb:YAG optical lattice they oscillate along the radial direction of

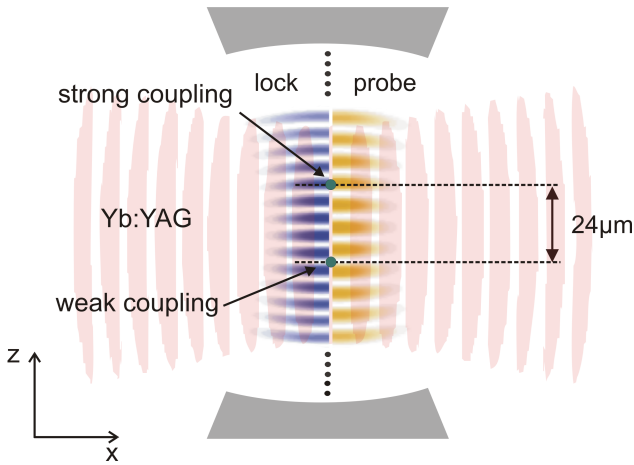


Figure 1.9: Laser configuration in the resonator. The atom is trapped at an anti-node of the Yb:YAG optical lattice. Along the cavity axis the dipole potential of the blue detuned lock laser confines the atom to the nodes of the lock laser standing wave. Due to the wavelength difference between lock and probe laser, the atom is confined to the places of strong coupling only at the center of the cavity. $24\ \mu\text{m}$ away from the cavity center the minima of the lock laser dipole potential coincide with the positions of minimum coupling.

the lattice with an amplitude of several micrometers as can be seen from the ICCD image in fig. 1.5. Thus, in the resonator they would oscillate over several maxima and minima of the coupling strength, which reduces the effective atom-cavity coupling. The lock laser, however, can be used to confine the atom also along the cavity axis. Since the lock laser is blue detuned from the atomic resonance, it pushes the atom away from its intensity maxima. Therefore, we adjust the lock laser wavelength such that it is 3 free spectral ranges away from the probe laser frequency. Consequently, at the center of the cavity the nodes of the lock-laser, where the atoms are confined, fall together with the anti-nodes of the probe laser, where the coupling strength is maximized. However, since they do not have the same wavelengths, lock and probe laser standing wave have a varying relative phase. At some distance from the cavity center, the two standing waves are exactly π out of phase. The nodes of the lock laser coincide then with the nodes of the probe laser, so that the atoms are confined to places of minimum coupling strength (see fig. 1.9). For a lock laser wavelength of 845 nm and a probe wavelength of 852 nm this distance between places of strong and weak coupling is $24\ \mu\text{m}$. To achieve reproducible and strong coupling for each atom that is inserted into the resonator, this distance should be as large as possible. Thus, the wavelength of the lock laser should be as close as possible to that of the probe laser. However, having lock and probe wavelengths very close to each other, poses a problem for the probe laser detection as will be pointed out in the next section.

1.2.3 Detection of the Resonator Transmission

The ultimate upper limit on the detection efficiency of the probe laser is set by the resonator itself: According to eq. (1.17), the finesse and also the linewidth only depend on the total resonator losses, i.e. the sum of T and A . For our resonator with a finesse of $\sim 10^6$, the absorption in the dielectric coatings becomes important. It is relative size of T and A which determines the maximum achievable detection efficiency, since absorbed photons cannot be detected. If the finesse is known, T and A can be determined by measuring the incoming,

reflected and transmitted powers of the probe laser in resonance with the cavity. This yields then also the fraction ϵ of the incoming light that is matched to the transverse mode of the resonator. The details of the measurement procedure are described in [12]. We have performed this measurement, resulting in

$$T = (0.6 \pm 0.1) \text{ ppm} , A = (2.0 \pm 0.2) \text{ ppm} , \epsilon = (36 \pm 9) \% . \quad (1.21)$$

Consequently, of the photons that are not reflected by the mirror only the fraction η_{cav} is transmitted. η_{cav} is given by:

$$\eta_{\text{cav}} = \frac{T}{T + A} = (24 \pm 4) \% . \quad (1.22)$$

This sets already a rather low upper limit on the total photon detection efficiency that can be expected. It underlines the need for an efficient detection setup. Apart from a high total detection efficiency, the major challenge of the probe laser detection is the suppression of the lock laser. While for the experiments presented in chapter 2 the probe laser power is on the order of ten thousand photons per second, i.e. a few tenth of fW, the lock laser power that exits the resonator is on the order of 10^{10} photons, i.e. \sim nW. Thus, to reduce the lock laser power to the order of magnitude of the detector dark counts of a few hundred photons per second, it has to be suppressed by eight orders of magnitude. At the same time, the probe laser should be suppressed as little as possible.

Our solution for the detection setup is shown in fig. 1.10. The separation of lock and probe laser is done in three steps, using a polarizer, an interference filter and a volume holographic grating (VHG). For the polarization separation, lock laser and probe laser are coupled into the two orthogonal polarization modes of the resonator. Slight polarization changes due to residual birefringence of optics and cavity substrates are compensated with a half wave plate (HWP) and a quarter wave plate (QWP). The orthogonally polarized beams then pass through a Glan-Taylor polarizing prism with an extinction ratio of better than 10^{-5} . The lock laser is reflected by the polarizer, while the probe laser is transmitted. The reflected lock laser light is detected on a transimpedance amplified APD with a bandwidth of 10 MHz and is used to monitor the lock performance.

In the current setup the polarization separation does not reach the extinction ratio of the polarizer of 10^{-5} , because of insufficient polarization purity of the light entering the cavity. The limiting element is the polarization maintaining fiber (PM fiber) that guides lock and probe laser to the cavity setup. It has an extinction ratio of only about 1/200. The polarization purity can be improved if the two lasers are brought to the cavity in two different PM fibers and then overlapped on a polarizing beam splitter. The polarization purity of the lock laser will then be limited by the extinction ratio of the polarizer used for the overlap, which is better than 1/1000 for a conventional polarizing beam splitter cube. With this technique at least one order of magnitude better suppression can be achieved. I have already prepared a second polarization maintaining fiber, and the two fiber modification of the setup is currently being implemented in the lab. The transmission of the optics behind the cavity up to and including the polarizer is:

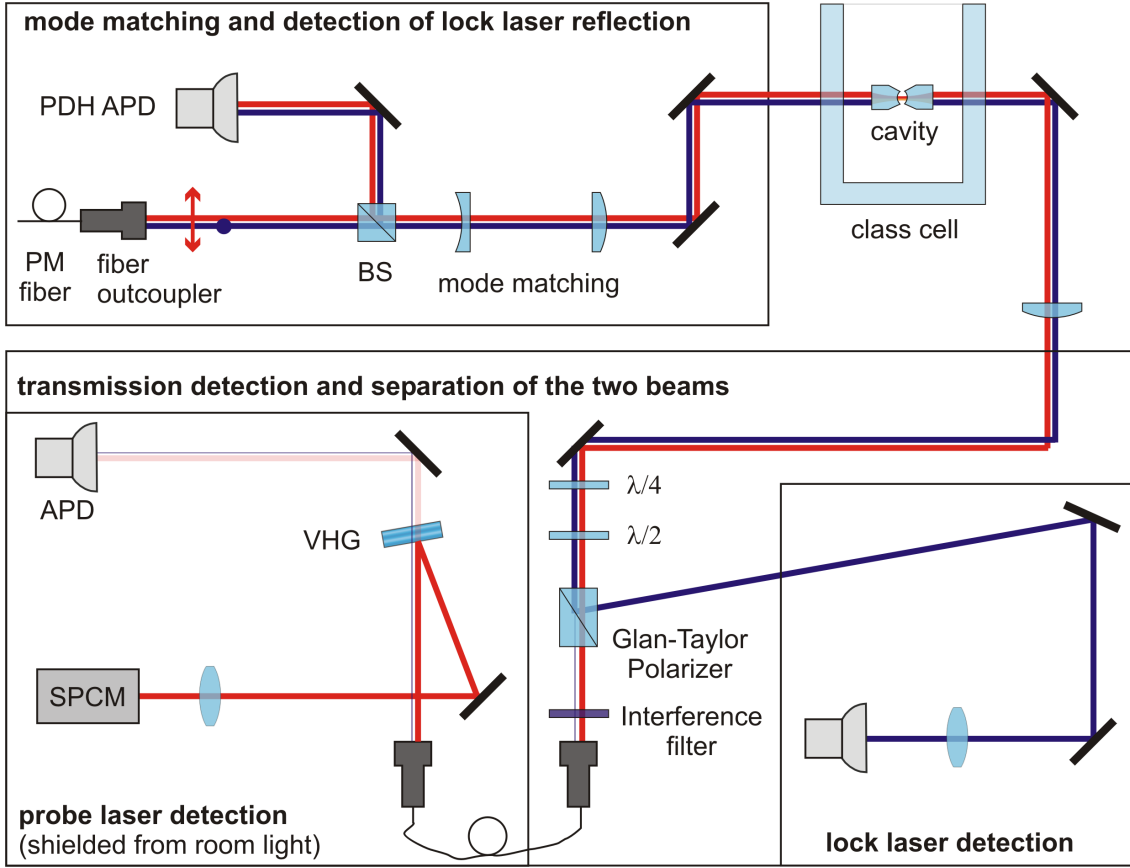


Figure 1.10: Schematic of the probe laser detection setup. Lock and probe laser are guided to the cavity setup in orthogonal polarization modes of a polarization maintaining fiber. A two lens telescope is used to mode match them to the QED cavity. As they exit the cavity, they beams pass through a polarizer that reflects most of the lock laser light, which is then detected on a fast APD. The light transmitted through the polarizer is spatially filtered by a single mode optical fiber. The residual lock laser light is filtered out by an interference filter and a volume holographic grating. The probe laser photons are detected on a SPCM. (The reflection of the lock laser from the QED cavity is detected on an APD. The signal is used for the PDH lock.)

$$\eta_{\text{opt}} = 0.82 \quad (1.23)$$

The losses are dominated by the glass cell ($\eta_{\text{cell}} = 0.91$) and the polarizer ($\eta_{\text{pol}} = 0.94$ for p-polarized light), which have been measured independently, as has the transmission of each waveplate of 0.99. The losses of the three mirrors and the lens have been estimated to be 0.5% per surface according to the coating specifications. They could not be measured independently, due to the weak powers transmitted through the cavity and the limited access to the optical setup.

The light that is transmitted through the polarizer is further filtered by an interference filter (company “Dr. Hugo Anders”) with a transmission of $\eta_{\text{IF}} = 0.77$ at 852 nm. The filter transmission at the lock wavelength of 845 nm is estimated to be below 10^{-2} . After the im-

provement of the polarization separation this filter is expected to be not necessary any more. Therefore, it has not been carefully characterized.

After passing through the interference filter the light is coupled into a non polarization maintaining single mode fiber that serves to purposes: It spatially filters the cavity transmission so that roomlight and other laser stray-light is blocked. And it guides the light from the cavity mode into a box shielded from roomlight, where an SPCM detects the cavity transmission. The measured fiber coupling efficiency is

$$\eta_{\text{fiber}} = 0.66. \quad (1.24)$$

After the first optimization a coupling efficiency of 78% was measured. After completion of the detection setup this value could not be reproduced. The reason for this is unclear.

Behind the fiber the light passes through a second wavelength selective element: a volume holographic grating (VHG) produced by the company ONDAX Inc. A VHG is a piece of UV sensitive glass, in which a sinusoidal variation of the refractive index has been imprinted using the photorefractive effect [16]. Due to the periodic index profile it works as a Bragg reflector. The period of the index profile can be designed so that a desired wavelength is reflected under a specific angle. Our grating has been customized to reflect the 852 nm probe light at an angle of incidence with respect to the substrate surface of 3.5° (see fig. 1.11(b)). The reflection coefficient as a function of wavelength at an angle of incidence of 3.5° is shown in fig. 1.11(a) as calculated by ONDAX. The reflection coefficient at 852 nm has been measured to be $\eta_{\text{VHG}} = 0.93$. The light that is not reflected by the grating is partly transmitted (5%), partly reflected by the anti-reflection coating (0.5%) and partly absorbed by the glass ($1 - 0.93 - 0.05 - 0.005 = 1.5\%$). To separate the coating reflection from the reflection by the grating, the k -vector is tilted by 1° with respect to the surface normal. The reflectivity of the grating has been measured for a lock laser wavelength of 840 nm² using calibrated attenuators and the SPCM. The measured reflectivity is 10^{-4} .

The light reflected from the grating is then focused onto an SPCM (Perkin Elmer SPCM-AQ RH-13, < 250 dark counts / s). Its quantum efficiency at the probe laser wavelength has been measured with a power meter and calibrated attenuators to be $\eta_{\text{SPCM}} = 0.49$. Multiplying all the efficiencies given above, one finds a total detection efficiency of

$$\eta = \eta_{\text{cav}} \eta_{\text{opt}} \eta_{\text{IF}} \eta_{\text{fiber}} \eta_{\text{VHG}} \eta_{\text{SPCM}} = 4.5\% \quad (1.25)$$

Before the optimization of the detection setup, lock and probe laser light were spatially separated with a standard diffraction grating. This had three main disadvantages: First, after two years, the diffraction efficiency of the grating had already decreased to 50% so that the total photon detection efficiency was only 1.4% (see [17]). Second, already at a lock laser

²During the optimization of the detection setup, the lock laser wavelength was 840 nm. Soon after the completion of the setup it was changed to 845 nm. If not otherwise specified, all values in this thesis are given for a lock laser wavelength of 845 nm.

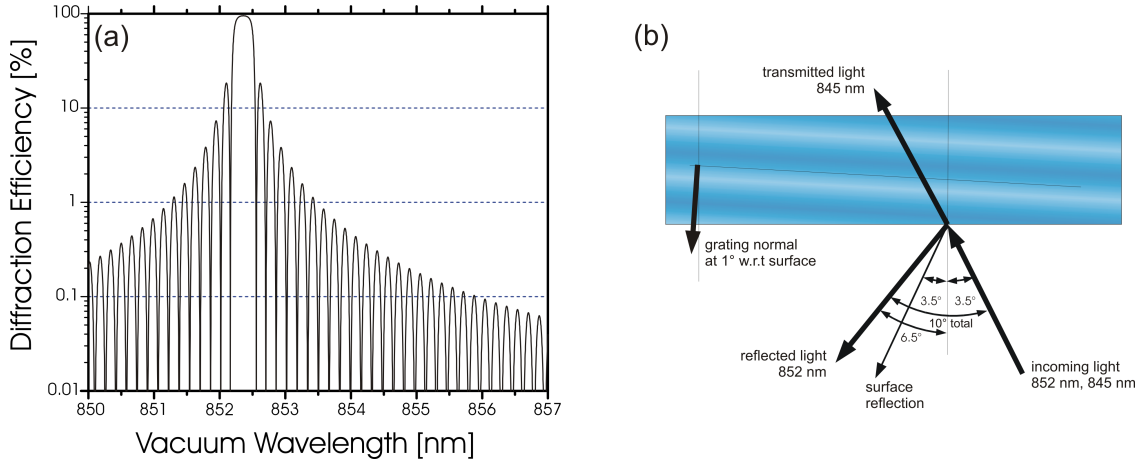


Figure 1.11: (a): Reflection spectrum of the volume holographic grating as calculated by ONDAX. (b): Angular configuration of the grating: The probe laser wavelength of 852 nm is reflected for an angle of incidence of 3.5° with respect to the surface. All other wavelengths are transmitted. To separate the reflection off the coating from the grating reflection, the grating k -vektor has an angle of 1° with respect to the surface normal.

wavelength of 840 nm the lock laser could not be suppressed below the detector dark counts. Thus, wavelengths closer to 852 nm could not be used with the old setup. Third, due to the diffraction grating, the optical path of the lock laser was dependent on its wavelength. Thus, each change of the lock laser wavelength would have required new alignment of the lock laser detection.

The optimized detection setup as presented here has a three times higher efficiency than the old setup, while providing a better suppression of the lock laser. Moreover, the alignment is not wavelength dependent so that the setup allows for an unproblematic switching between different lock laser wavelengths. For example in future experiments it is planned to have the lock laser red detuned with respect to the atomic transition. This is now easily possible.

1.2.4 Influence of the Caesium Multi-Level Structure

Due to the birefringent splitting of the cavity resonance of $\Delta\omega_{\text{br}} = 2\pi \times 3.86$ MHz, only linear polarization can be resonantly coupled into the cavity. Thus, it is impossible to only couple the closed transition $|F = 4, m_F = 4\rangle \rightarrow |F' = 5; m'_F = 5\rangle$ to the cavity mode. This transition is a σ^+ -transition, which would require circularly polarized light in the cavity.

A linearly polarized cavity mode can either couple π -transitions or σ^+ - and σ^- transitions at the same time, depending on the direction of the quantization axis. All the experiments presented in this thesis are done with a magnetic field along the cavity axis (z -direction in fig. 1.9), defining the quantization axis. In this configuration, the linearly polarized cavity mode couples σ^+ - and σ^- transitions. We have chosen this configuration, because it simplifies the comparison of theory and experiment. If σ^+ - and σ^- -transitions are driven, the atom spends most of the time in the outermost Zeeman sublevel, because the outermost σ^+ - and

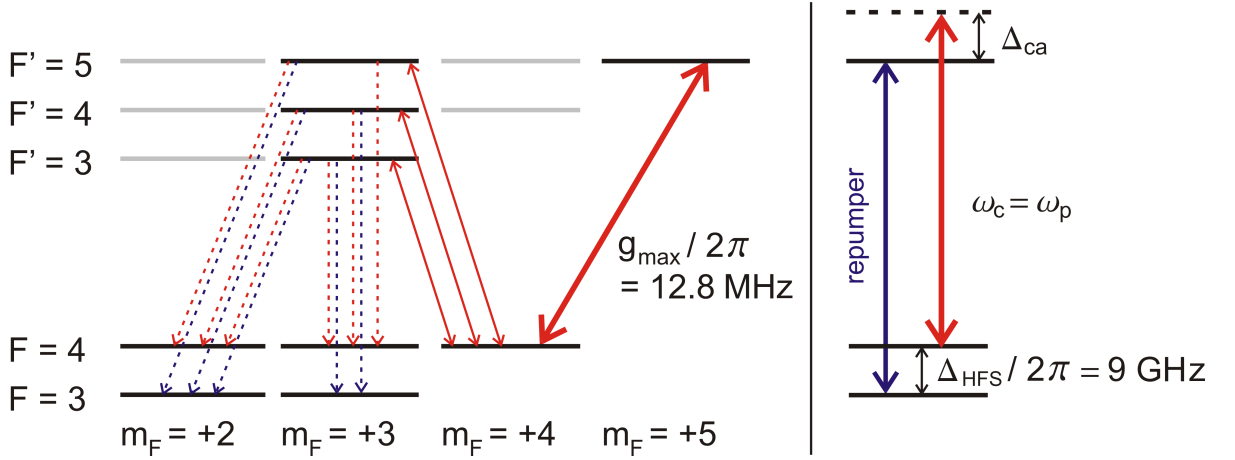


Figure 1.12: The linearly polarized probe laser induces σ^+ - as well as σ^- -transitions. If the atom is excited to one of the states of the $|F' = 3, 4\rangle$ manifolds it can decay to the groundstate $|F = 3\rangle$ manifold, which is dark with respect to the probe laser. To bring the atom back to the coupled $|F = 4\rangle$ manifold a repumping laser resonant with the $|F = 3\rangle \rightarrow |F' = 4\rangle$ transition can be applied.

σ^- -transitions have the largest Clebsch-Gordon-Coefficients. If π -transitions were driven, the atom would be expected to have a rather broad m_F -distribution. The calculation of this distribution is rather laborious. Moreover, it is favourable to have a quantization axis parallel to the polarization of the Yb:YAG dipole trap. If this were not the case, a complicated mixing of the Zeeman sublevels of the excited state would occur.

Since a linear probe laser always couples atomic transitions that are not closed, the atom is pumped into a dark state if no repumping laser is applied. This is schematically illustrated in fig. 1.12. In all the experiments presented in this thesis, the probe laser is resonant with the empty cavity ($\omega_c = \omega_p$) and slightly blue detuned from the $|F = 4\rangle \rightarrow |F' = 5\rangle$ transition. Assume the atom is in the outermost Zeeman state of the $|F = 4\rangle$ manifold. Then most of the time it cycles on the closed σ^+ -transition $|F = 4\rangle \rightarrow |F' = 5\rangle$, because the $|F = 4, m_F = 4\rangle \rightarrow |F' = 5; m'_F = 5\rangle$ has a much larger Clebsch-Gordon Coefficient than the $|F = 4, m_F = 4\rangle \rightarrow |F' = 5; m'_F = 3\rangle$ transition. However, the linear polarized probe laser also drives σ^- -transitions and excites from time to time one of the $|F' = 3, 4, 5; m_F = 3\rangle$ states. If the $|F' = 3, 4\rangle$ states are excited, the atom can decay to the $|F = 3\rangle$ manifold. The $|F = 3\rangle$ states are dark with respect to the probe laser, due to the large hyperfine splitting of the ground state of $\Delta_{\text{HFS}} = 2\pi \times 9 \text{ GHz}$. Thus, in order to keep the atom in the $|F = 4\rangle$ manifold, a repumping laser (short: repumper) resonant with the $|F = 3\rangle \rightarrow |F' = 4\rangle$ transition is applied. The maximum coupling strength on the outermost Zeeman transition is $g_{\max} = 12.8 \text{ MHz}$, already taking into account that only half of the probe laser intensity has the right polarization to couple this σ^+ -transition.

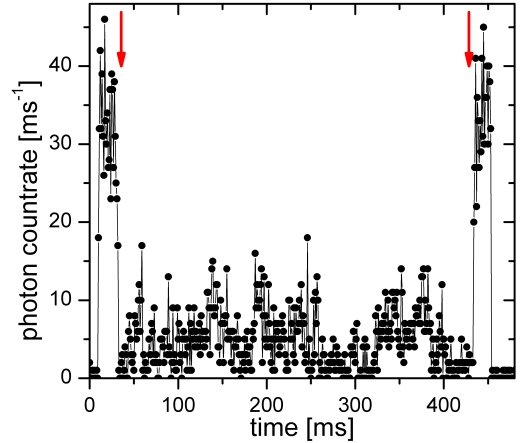
1.2.5 Continuous Monitoring of the Atom Light Interaction via the Resonator Transmission

In this section I present the continuous monitoring of the atom-light interaction via the resonator transmission. This measurement makes use of the resonator lineshift caused by the coupling of a single atom to the cavity field. It is the prototype of all measurements presented in chapter 2 and shows how the different parts of the setup described above work together. Moreover, the lineshift measurement provides a rough estimate of the achieved atom-light coupling strength and its variations.

The experimental sequence is as follows: Atoms are loaded into the MOT where they are counted via their fluorescence. Only if exactly one atom is present in the MOT, it is transferred to the optical lattice. In the lattice the atom is illuminated by the MOT molasses beams and imaged onto the ICCD camera. By leaving on the MOT repumping laser for 2 ms after the molasses beams have been switched-off, the atom is prepared in the $|F = 4\rangle$ state. From the ICCD image, the atomic position relative to the camera is determined. By moving the optical lattice, the atom is then inserted into the cavity, which is blue detuned with respect to the atomic transition by several Γ . Before the atom is inserted, the probe laser is already applied on resonance with the empty cavity. Upon insertion of the atom into the cavity, the transmission of the probe laser drops, due to the shift of the cavity frequency induced by the atom. As the atom is retrieved from the resonator by moving the optical lattice in the opposite direction, the transmission rises again to its original value. The repumping laser that brings the atom back from the uncoupled $|F = 3\rangle$ state to the coupled $|F = 4\rangle$ state is applied along the direction of the optical lattice (x -direction in fig. 1.9). The recorded probe laser transmission as a function of time is depicted in fig. 1.13. The cavity-atom detuning used for this measurement is $\Delta_{ca} = 2\pi \times 38$ MHz, including the light shift by the optical lattice. It can be seen that the transmission varies significantly, while the atom is in the resonator. This is due to variations of the coupling strength caused by position changes of the atom. In fig. 1.13 the transmission level, i.e. the transmission while the atom is coupled to the cavity relative to the empty cavity transmission, varies approximately between 10% and 30%. From eq. (1.13) one finds that this corresponds to coupling strengths between 11.7 MHz and 6 MHz. Note that deducing the coupling strength from the transmission level is only valid, if the coupling strength is constant during the integration time. If the coupling strength varies significantly during the integration time, the average transmission level will not correspond to the average coupling strength due to the nonlinear dependence of the transmission level on g .

The motion of the atom inside the resonator that leads to the observed variations of the coupling strength is determined by a rather complex combination of heating and cooling mechanisms. The dominant heating process is probably parametric heating due to fluctuations of the lock laser power: Due to noise on the cavity lock, the intra cavity lock laser power fluctuates. Noise at multiples of the frequency of the lock laser dipole potential excites higher vibrational states in that potential and possibly even causes jumps between different lock laser potential minima [18]. Moreover, also the scattering of probe laser and repumper photons heats the atom. These heating processes are compensated by cavity cooling mechanisms. Otherwise,

Figure 1.13: Typical transmission signal obtained for a single caesium atom coupled 400 ms to the resonator. The arrows indicate the insertion and retrieval of the atom by means of the movable optical lattice. Due to position changes of the atom, the atom light coupling strength varies with time. This causes variations in the transmitted intensity.



the long lifetimes of the atoms in the cavity could not be explained. The details of this cavity cooling are not clear.

Detailed theoretical work on cavity cooling has been done by H. Ritsch and P. Domokos [19]. This work is, however, not directly applicable to our setup, since it does not take any trapping potentials into account, such as that by the Yb:YAG optical lattice and by the lock laser.

In our experiment, we observe that the variations of the coupling strength as seen in the variation of the transmitted intensity increase as we reduce the cavity-atom detuning. We suppose that this is because the cooling mechanism does not work as effectively near the atomic resonance. From our experience in the laboratory, rather stable coupling for several hundred milliseconds is only possible for $\Delta_{\text{ca}} \gtrsim 38$ MHz. This limits the cavity-atom detuning that can be used for the state detection measurements that are presented in the following section.

I have now outlined the principles of the theory of atom-light interaction in a resonator and described the experimental setup on which this thesis is based. In the next chapter I present investigations of the internal state dynamics of one and two atoms in the resonator.

2 Quantum Jumps of Neutral Atoms in a Resonator

For a complete measurement of the state of the coupled atom-resonator system it is necessary to measure the state of the intra cavity field as well as the internal state of the atom. While a measurement of the intracavity light field is naturally realized by detecting photons leaking from the cavity [20], a measurement of the internal atomic state requires more effort. In this chapter I will explain how the coherent atom-light interaction in a high finesse resonator can be used to perform a fast and nondestructive readout of the internal atomic state [2]. I will furthermore present quantum jumps of a single and two atoms inside the resonator that can be monitored by virtue of this nondestructive detection method.

2.1 Non-Destructive State Detection Using a High-Finesse Optical Resonator

What is the difficulty in a measurement of the internal atomic state? In principle, illuminating a caesium atom with a laser close to the $|F = 4\rangle \rightarrow |F' = 5\rangle$ transition and detecting the fluorescence could serve as such a measurement. A problem with this method arises, however, when the rate of state changing Raman scattering events via the $|F = 4\rangle \rightarrow |F' = 3, 4\rangle$ transitions becomes comparable to the rate of fluorescence photon detection (see section 1.2.4). It is then not possible to measure the atomic state, because the measurement process changes the state before the measurement is completed. This will be a problem for most experiments, since efficient collection of the photons, spontaneously emitted into the full solid angle, has proven to be experimentally very challenging.

The most common way to detect the internal state of a single trapped atom is to apply a so-called push-out laser [21–23]. A push-out laser is tuned such that it is close to an atomic transition starting from one level and far off resonance for all transitions starting from another level. The trapping potential is lowered such that a few photon recoils push the atom out of the trap. Consequently, if the atom is in the lower level of the push-out transition it is removed from the trap. Otherwise, it remains in the trap. Thus, the push-out laser transforms the internal state measurement into a measurement of the number of atoms in the trap. This can easily be done via fluorescence detection as described in chapter 1.

A serious disadvantage of the push-out technique is the fact that the measurement is based on conditional *removal* of the atom from the trap. In this sense it is a destructive measurement. After each measurement a new atom has to be prepared for the next experimental run.

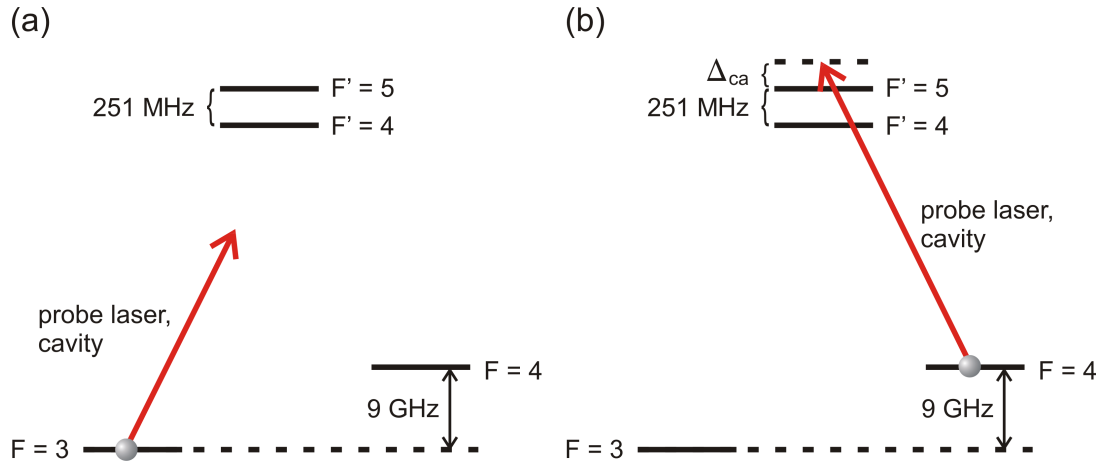


Figure 2.1: Simplified level scheme of the caesium D_2 -line. (a) If the atom is in $|F = 3\rangle$, probe laser and cavity are far detuned from any available transition. The cavity spectrum is unaltered. (b) If the atom is in $|F = 4\rangle$, it strongly interacts with the cavity field. This interaction shifts the cavity resonance with respect to the probe laser frequency and causes a drop in the probe laser transmission.

With a high finesse optical resonator it is possible to perform an atomic state measurement that avoids this problem. It is based on the shift of the resonator frequency caused by the dispersive interaction between an atom and the cavity field. This measurement neither removes the atom from the trap, nor does it change its internal state.

2.1.1 A Resonator as an Atomic State Detector

In section 1.1 it was explained that the coupling of a single two-level atom to the resonator field alters the transmission spectrum of the resonator. For $\Delta_{\text{ca}} \lesssim \Gamma$ the interaction leads to an almost symmetric splitting of the cavity resonance. If the resonator is tuned several atomic linewidths away from the atomic transition, this splitting is similar to a shift of the cavity resonance frequency. Thus, the transmission of a probe laser which is resonant with the empty resonator is suppressed if a single atom couples to the resonator field. If, however, the cavity's resonance frequency is very far detuned from the atomic transition, the transmission spectrum changes so little that the described suppression of the probe laser transmission cannot be observed.

In a three-level atom with a large groundstate splitting, this dependence of a probe laser's transmission on the detuning from an atomic resonance can be used to measure the internal state of the atom. Figure 2.1 depicts the hyperfine levels of the caesium D_2 -transition, relevant for the state detection. The two groundstates that are to be distinguished by the state measurement exhibit a large hyperfine splitting of 9 GHz. The hyperfine splitting of the excited state is much smaller. For the state detection the probe laser is always resonant with the empty cavity. The resonator is tuned 38 MHz to the blue of the $|F = 4\rangle \rightarrow |F' = 5\rangle$ transition, including the light shift by Yb:YAG optical lattice. For this detuning and the maximum coupling strength

of 12.8 MHz the probe laser transmission drops to 9% of the empty cavity transmission, if an atom in $|F = 4\rangle$ is inside the cavity field. If, however, the atom is in the $|F = 3\rangle$ state, probe laser and resonator are about 9 GHz detuned from any available transition. For this detuning the cavity lineshift due to the atom-light interaction, given by g^2/Δ_{ca} , is much smaller than the cavity linewidth κ so that the transmission of the probe laser is unaffected by the atom. To summarize, for an atom in $|F = 4\rangle$ the transmission of the probe laser is suppressed, for an atom in $|F = 3\rangle$ it is not. Consequently, the transmission of the probe laser through the resonator is a direct measure of the internal state of the atom inside the resonator field [2].

The suppression of the transmission due to the atom-light interaction, on which the state detection is based, is a coherent, dispersive effect. It does not rely on photon scattering. However, for feasible coupling strengths the detuning between atom and resonator cannot be made so large that spontaneous scattering is negligible, if a high signal to noise ratio is to be achieved. Therefore, as explained in section 1.2.5 from time to time spontaneous inelastic Raman scattering via the $|F' = 3, 4\rangle$ states changes the atom's state during the measurement. This becomes obvious when a sequence of many consecutive state measurements is performed. Figs. 2.2(a) to (c) depict three such sequences. They show the number of probe laser photons, detected during a 1 ms binning interval as a function of time. Each data point can be thought of as an atomic state measurement. At $t = 33$ ms a single caesium atom, prepared in the $|F = 4\rangle$ groundstate is inserted into the resonator field. The $|F = 4\rangle$ state is verified by the drop of the probe laser transmission. After the insertion the transmission stays low for several milliseconds. This shows that the atom remains in $|F = 4\rangle$ for several consecutive state measurements. After some time, however, spontaneous inelastic Raman scattering transfers the atom to the $|F = 3\rangle$ groundstate. This sudden change of the state translates into a discontinuous change in the transmission signal from low to high transmission. Such an abrupt change of the atomic state from one measurement to the next is called a quantum jump [24]. For each measurement there is a small probability that such a quantum jump occurs. The exact instance at which the jump happens cannot be predicted, due to the inherent randomness of quantum mechanics. In each of the traces of fig. 2.2 the quantum jump occurs at a different time. However, the ensemble average of many such state measurement sequences is very well predictable. It has an exponential shape, because the jump probability per unit time is constant (fig. 2.2(d)).

In the experiment there is an imperfection that has to be taken care of: Sometimes an atom can get lost from the resonator or can move to places of much smaller coupling strengths. Since an atom in $|F = 3\rangle$ leaves the probe laser transmission unchanged, the loss of an atom cannot be distinguished from a quantum jump to the $|F = 3\rangle$ state. To make sure that the atom was coupled to the resonator field for the whole measurement sequence, the repumping laser along the optical lattice direction is switched on. It is so strong that with the repumper on, the atom is nearly always in the $|F = 4\rangle$ state where it suppresses the probe laser transmission. Thus, a transmission drop upon the activation of the repumping laser ensures that the atom is still coupled to the resonator.

The time τ_{43} the atom spends on average in $|F = 4\rangle$ until it jumps to $|F = 3\rangle$ can be determined by fitting an exponential decay function to the ensemble average of many state mea-

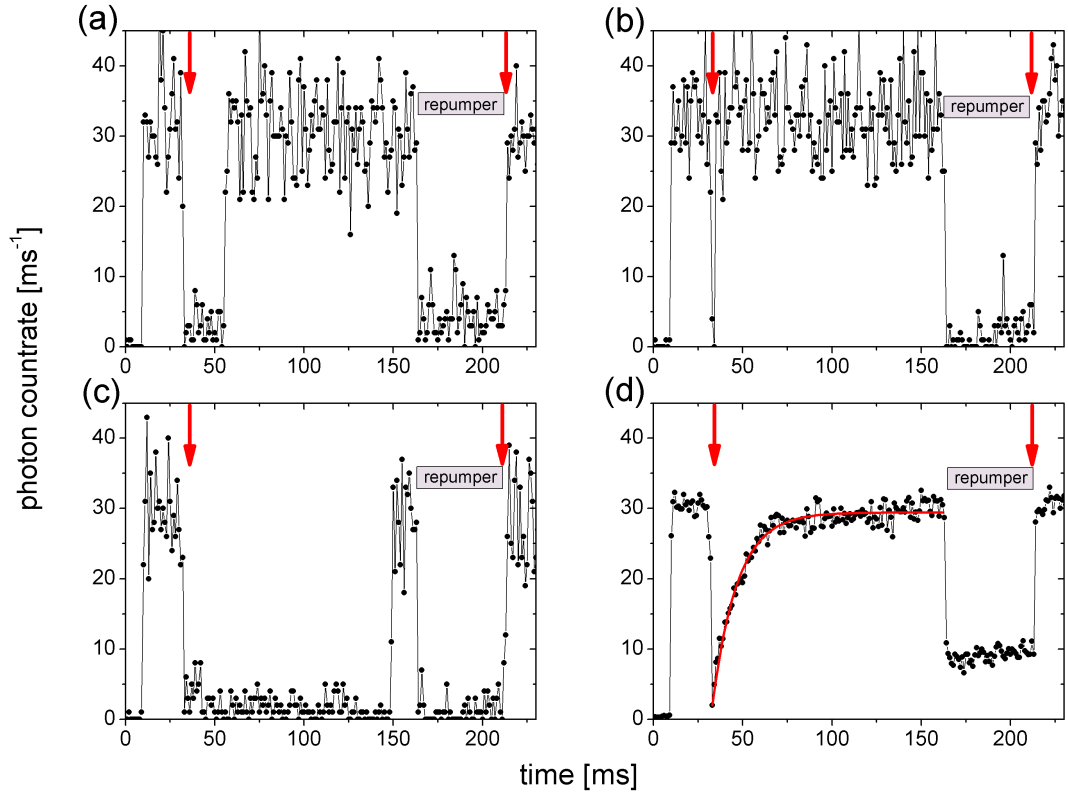


Figure 2.2: (a) to (c): Sequences of measurements of the transmission of the resonator containing a single caesium atom. The atom is prepared in $|F = 4\rangle$. For this state the transmission is suppressed. After some time inelastic Raman scattering changes the atomic state, causing a rise of the transmission. The instants of these quantum jumps are random. (d): The average over 31 single traces exhibits an exponential shape. Arrows indicate insertion and removal of the atom from the resonator.

surement sequences (fig. 2.2(d)). Only those traces are used for the ensemble average, where the transmission drops upon the activation of the repumper. For the current setup we have measured $\tau_{43} \approx 13$ to 18 ms for an empty cavity transmission of 30 photons/ms. This corresponds to a probability of 5 to 8% for a quantum jump to occur during the 1 ms measurement time.

The time constant τ_{43} depends strongly on experimental parameters, such as atom-cavity coupling strength, cavity-atom detuning and probe laser intensity. The influence of these parameters on τ_{43} and the performance of the state detection will be discussed in the following section.

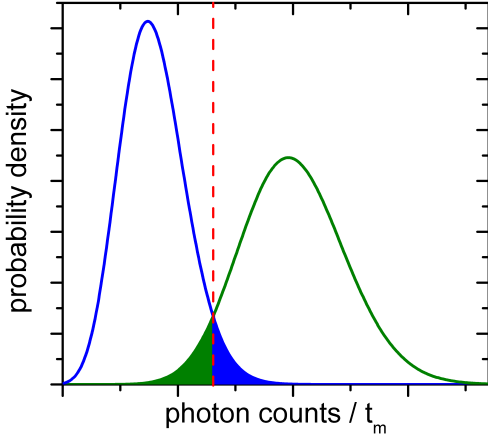


Figure 2.3: The overlap of the photon number distribution for the atom in $|F = 4\rangle$ and $|F = 3\rangle$ determines the probability for a measurement error due to noise in the photon counting measurement (schematic plot).

2.1.2 Influence of Experimental Parameters on the Performance of the State Detection

The nondestructive state measurement described in the previous section is best characterized by the probability that it yields a wrong result p_{err} . There are two ways in which a measurement error can occur: First, due to various noise sources the separation of the two transmission levels is never perfect. It can happen that during the measurement time the transmission is rather high, although the atom is in $|F = 4\rangle$ and vice versa. I denote the probability for this to happen as p_n . Second, inelastic Raman scattering can change the atom's state during the measurement, which in many cases also leads to a wrong measurement outcome. The probability for this to happen is denoted by p_{jump} . The total error probability is then: $p_{\text{err}} = p_n + p_{\text{jump}} - p_n p_{\text{jump}}$. The last term corrects for double errors and is negligible for small p_{err} . The jump probability p_{jump} is given by

$$p_{\text{jump}} = 1 - \exp(-t_m/\tau_{43}), \quad (2.1)$$

where t_m is the photon integration time, defining the duration of a single state measurement. The probability p_n is given by the overlap of the photon number distributions, corresponding to the two state dependent transmission levels. This is illustrated in fig. 2.3. The sum of the two colored areas corresponds to p_n . For shot noise limited detection, the count rate distributions depend only on the position dependent effective coupling strength $g_{\text{eff}} = g M(\mathbf{r})$ (see eq. (1.3)), the atom-resonator detuning Δ_{ac} , and the number of photons n_0 accumulated during the integration time when no atom is coupled to the resonator field.

In the experiment the most directly accessible observables are not p_{jump} and p_n , but the jump time τ_{43} and the resonator transmission level for one atom in $|F = 4\rangle$ coupled to the resonator $\text{TL}_{F=4}$. We have measured these quantities for a wide range of atom-resonator detunings. The results are displayed in fig. 2.4. In order to evaluate the measured data, I have performed calculations of τ_{43} and $\text{TL}_{F=4}$ by numerically solving the master equation¹. For

¹The numerical solution of the master equation is done by means of the quantum optics toolbox for MATLABTM[25]

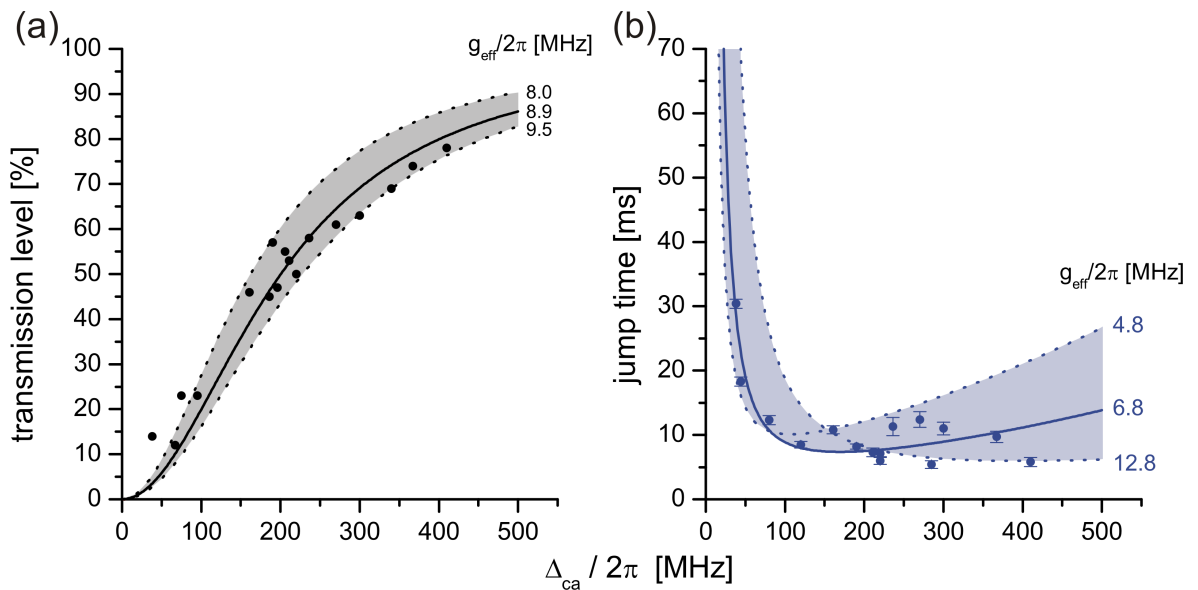


Figure 2.4: (a): Transmission levels measured for 1 atom in $F = 4$ coupled to the resonator as a function of cavity-atom detuning. (b) Single-atom jump time as a function of cavity-atom detuning. For the jump time measurement the empty cavity transmission is set to 20 photons/ms, while the transmission level measurement is done with 30 photons/ms. The line plots are simulations based on the numerical solution of the master equation (see text).

the calculation of τ_{43} the Kramers-Heisenberg Formula has been applied, taking into account the multi-level structure of the caesium atom [26]. The details of this calculation are given in Appendix A. The input parameters of these calculations are the decay rates κ and Γ of the cavity field and the atomic excitation, the maximum atom-light coupling strength g_{\max} , the position dependent effective coupling strength g_{eff} , and the probe laser intensity, which is proportional to n_0 . While κ , Γ , and g_{\max} are fixed to the values given in section 1.2 and n_0 is well controlled, g_{eff} is an unknown free parameter in our experiment. Thus, I have used g_{eff} as a fit parameter for the theoretical calculations. In principle the full motional dynamics of the atom should be included in the calculations. For simplicity, however, I have assumed a time independent atomic position and modeled different values of g_{eff} by changing this position. The solid lines show the best fits of the theory to the data. For the dashed lines g_{eff} is chosen such that most of the measured data lie in the colored areas within these lines. This gives an idea of the effective coupling strength achieved in the experiment and its variation.

Most of the transmission level measurements are well described by effective coupling strengths between 8 and 9.5 MHz. The best fit is achieved for $g_{\text{eff}} = 2\pi \times 8.9$ MHz. Only for small detunings two data points lie outside this region of coupling strengths. The reason for this is not clear. We assume that it is related to the cavity cooling mechanism (see section 1.2.5). This fits with our observation, that stable transmission levels below 10% are hardly ever observed, no matter how low Δ_{ca} is chosen.

As can be seen from fig. 2.4(b), the measured jump times are not described by the same range

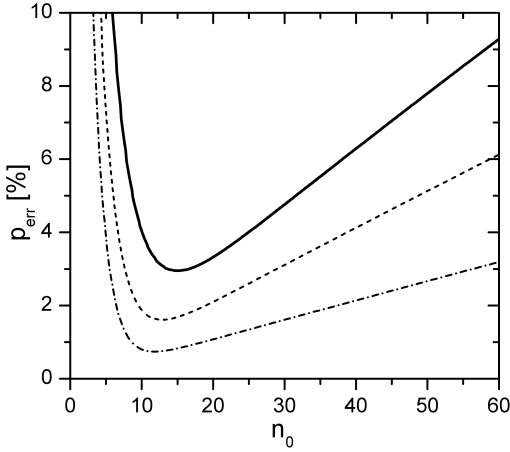


Figure 2.5: Total error probability of the dispersive state detection measurement as a function of n_0 for effective coupling strengths of 7 MHz (solid line), 9 MHz (dashed line), and 12.8 MHz (dashed-dotted line). The calculation takes into account the finite photon detection efficiency of $\eta = 4.5\%$.

of effective coupling strengths as the transmission levels. To describe all measured jump times, effective coupling strengths between 4.8 MHz and the maximum coupling strength 12.8 MHz have to be assumed. The best fit is achieved for $g_{\text{eff}} = 2\pi \times 6.8$ MHz. As can be seen from the figure, the value for g_{eff} obtained from the fit is mostly determined by the strongly varying jump times measured for large cavity-atom detunings $\Delta_{\text{ca}} > 2\pi \times 200$ MHz. Especially the three rather long jump times observed between 200 and 300 MHz indicate a rather low effective coupling strength. The reason for the strong variations of the jump time are not understood. Again the motional dynamics of the atom may be a possible cause. A systematic investigation of these variations has so far not been possible, since they are not reproducible in the experiment from day to day.

Some of the measured jump times lie even below the dashed line calculated for the maximum coupling strength of 12.8 MHz. They cannot be explained within the applied model, because an unphysical value for g_{eff} above the maximum coupling strength would have to be assumed to explain these data. This may be due to the simplifying assumption that the atom is always in one of the outermost Zeeman substates. From these states only the “inward” transitions $|F = 4; m_F \pm 4\rangle \rightarrow |F' = 3, 4; m_F = \pm 3\rangle$ can cause jumps from $|F = 4\rangle$ to $|F = 3\rangle$. If the atom were in one of the inner Zeeman states $|F = 4; |m_F| < 4\rangle$, also the “outward” transitions, e.g. $|F = 4; m_F = \pm 3\rangle \rightarrow |F' = 4; m_F = \pm 4\rangle$ would be allowed. This would decrease the jump time at the same intra cavity intensity (see Appendix A for details). Thus, the jump times calculated for the outermost Zeeman sublevels are systematically overestimated, if the atom has in fact a finite probability to be in one of the inner Zeeman levels.

The results from fig. 2.4 clearly state that the quality of the state measurement increases for low cavity-atom detunings. Small cavity-atom detunings yield low transmission levels and long jump times and thus minimize p_{err} . A detuning smaller than $\Delta_{\text{ca}} \lesssim 2\pi \times 38$ MHz has proven to be rather unfeasible, because the atom-light coupling becomes significantly more unstable and the atoms get lost rather fast. Therefore we set $\Delta_{\text{ca}} = 2\pi \times 38$ MHz for the state detection. Apart from Δ_{ca} , only n_0 can be adjusted without relevant restrictions. Figure 2.5 depicts p_{err} as a function of n_0 for three different effective coupling strengths at

$\Delta_{ac} = 2\pi \times 38$ MHz. For $g_{\text{eff}} = 2\pi \times 7$ MHz, which is the effective coupling strength extracted from the jump time measurements, the minimum error probability $p_{\text{err}} = 3\%$ is achieved for $n_0 = 15$. For stronger coupling, the error probability decreases and its minimum shifts towards smaller photon numbers.

A prime example of the application of a continuous and nondestructive measurement is the observation of quantum jumps. The measurement sequences in fig. 2.2 show single quantum jumps from $|F = 4\rangle$ to $|F = 3\rangle$, caused by Raman scattering of probe laser photons. Quantum jumps in the opposite direction can be induced by a repumping laser. It is then possible to observe random telegraph signals of the resonator transmission exhibiting quantum jumps between the two groundstates for several hundred milliseconds. The measurement and analysis of these random telegraph signals will be presented in the next section.

2.2 Continuous Observation of Single Atom Quantum Jumps

As described in section 1.2, in our experiment we usually illuminate the atoms with a repumping laser, shone in from the side of the resonator along the direction of the optical lattice. The repumper is resonant with the $|F = 3\rangle \rightarrow |F' = 4\rangle$ transition. For transmission level measurements, this laser is so strong that it ensures steady transmission signals without any quantum jumps. However, a steady transmission signal does not mean that the repumping process is infinitely fast. The time the atom spends on average in $|F = 3\rangle$ is just much shorter than the time resolution of the transmission measurement. The dwell time of the atom in $|F = 3\rangle$ can be increased by decreasing the repumper intensity. As soon as it becomes comparable to the measurement time resolution of 1 ms, quantum jumps can be observed.

For the observation of random telegraph signals the repumper intensity is set such that the dwell times in the “on” state corresponding to $|F = 3\rangle$ and the “off” state corresponding to $|F = 4\rangle$ are approximately equal. In order to study the statistical properties of the quantum jumps, I have recorded several hundred random telegraph signals of 400 ms duration each. The observation time has been limited to about 400 ms, due to the life time of the atoms in the resonator. Two example traces are shown in fig. 2.6. The photon number $n_0 = 30$ has deliberately been chosen larger than the optimum photon number for minimum error probability calculated above. This is because for the investigation of quantum jumps a good separation of the transmission levels is more important than a low jump time. The jump time should only be much larger than the measurement time resolution for the jumps to be resolved.

As can be seen in fig. 2.6, the obtained telegraph signals are of varying quality. Often the $|F = 4\rangle$ transmission level varies during the observation as in fig. 2.6(b), probably due to changes in the atomic position. This has influence on the separability of the two transmission levels. Figure 2.7(a) shows the relative frequency distribution of the number of transmitted photons per time bin for all 348 traces, where the atom survived in the resonator for the whole 400 ms. Clearly the lower peak, corresponding to the $|F = 4\rangle$ transmission level is not shot

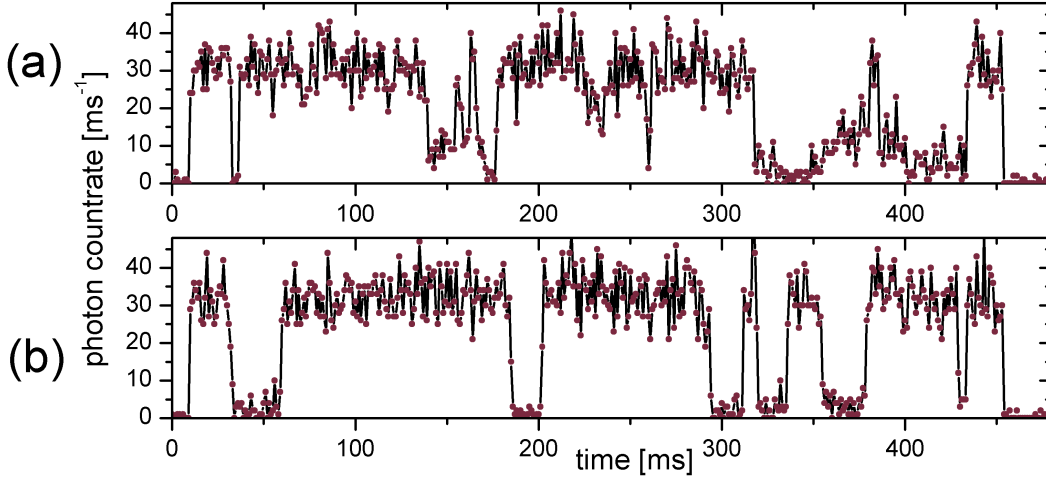


Figure 2.6: Two random telegraph signals, revealing quantum jumps of a single cesium atom in the resonator. In many traces the $|F = 4\rangle$ transmission level varies due to position changes of the atom (a). 27 out of 348 shots can be found without significant transmission level changes (b).

noise limited, because of position changes of the atoms. There is a significant overlap of the two peaks. Figure 2.7(b) shows the same histogram for the best 27 shots, which have the quality of fig. 2.6(b). They have been selected by eye for minimum variations in the lower transmission level. For this small selection, the $|F = 4\rangle$ transmission level is closer to the shot noise limit and the overlap is significantly reduced. The black fit curves are constructed as follows: A Poissonian is fitted to the $|F = 3\rangle$ peak. The good fit shows that the transmission measurement is essentially shot noise limited. Since the transmission measurement is shot noise limited as shown in section 1.2, the fit is very good and the area of the Poissonian yields the probability $p_{F=3}$ to find the atom in the $|F = 3\rangle$ state at any given instant. Using this probability, a second Poissonian is fitted to the $|F = 4\rangle$ peak with only the average value as fit parameter. The sum of these two Poissonians yields the black fit curves in fig. 2.6.

Since the $|F = 3\rangle$ transmission level is shot noise limited, the difference between the total histogram and the Poissonian fit to the $|F = 3\rangle$ peak corresponds to the count distribution belonging to the $|F = 4\rangle$ state. With the $|F = 3\rangle$ and $|F = 4\rangle$ count distributions independently available, a threshold can be found that minimizes the overlap of these two distributions. For the whole data set, the minimum overlap of 2.4% is achieved for the threshold set between 19 and 20 photons. For the selected 27 best shots, the minimum overlap reduces to 1.3% for the threshold between 18 and 19 photons.

The dynamics of the quantum jumps are described by the following rate equations [27]:

$$\frac{dp_{F=3}(t)}{dt} = -R_{34} p_{F=3}(t) + R_{43} p_{F=4}(t) \quad (2.2)$$

$$\frac{dp_{F=4}(t)}{dt} = -R_{43} p_{F=4}(t) + R_{34} p_{F=3}(t) \quad (2.3)$$

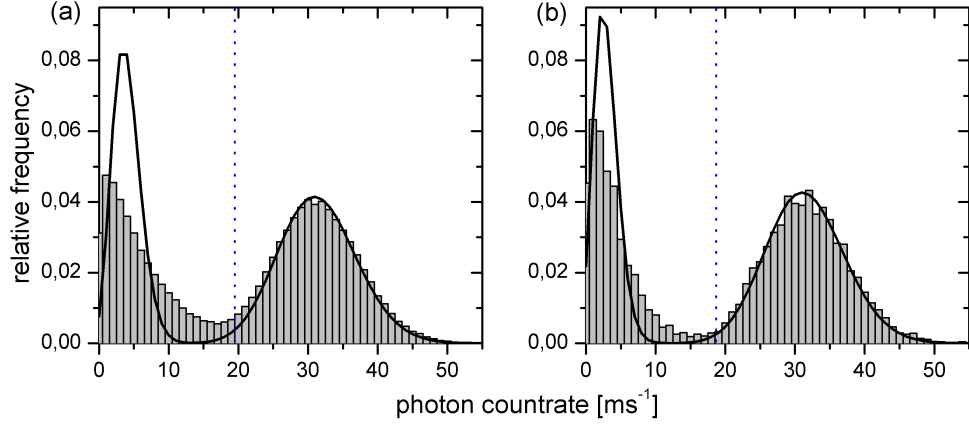


Figure 2.7: Relative frequency distribution of photon counts of (a) all 348 random telegraph signals of 400 ms duration and (b) of the best 27 traces. The black curves are Poissonian fits (see text for details).

Here, p_F is the probability for the atom to be in state $|F\rangle$. R_{34} and R_{43} are the rates of quantum jumps from $|F=3\rangle$ to $|F=4\rangle$ and vice versa. These two rates fully determine the dynamics of the atomic state during observation. For observation times much longer than the jump rates, the probabilities $p_{F=3}(t)$ and $p_{F=4}(t)$ equilibrate to their steady state values $p_{F,ss}$. Setting the right side of eqs. (2.2) and (2.3) to zero and using that $p_{F=3} + p_{F=4} = 1$, these probabilities can be linked to the jump rates

$$p_{F=3,ss} = \frac{R_{43}}{R_{43} + R_{34}} \quad (2.4)$$

$$p_{F=4,ss} = \frac{R_{34}}{R_{43} + R_{34}}. \quad (2.5)$$

The values of $p_{F=3,ss}$ and $p_{F=4,ss}$ are given by the areas of the two peaks in the photon count histograms. From the Poissonian fit of the $|F=3\rangle$ peak in the histogram of all 348 traces (fig. 2.7(a)) one finds

$$p_{F=3,ss} = 58\% \quad (2.6)$$

$$p_{F=4,ss} = 1 - p_{F=3,ss} = 42\%. \quad (2.7)$$

The absolute jump rates R_{34} and R_{43} can, however, not be deduced from these values. The steady state probabilities determine only the ratio between the rates. To obtain the absolute rates, I have extracted R_{43} from the ensemble average of many single quantum jumps from $|F=4\rangle$ to $|F=3\rangle$ without applying the repumping laser as described in section 2.1.2. R_{34}

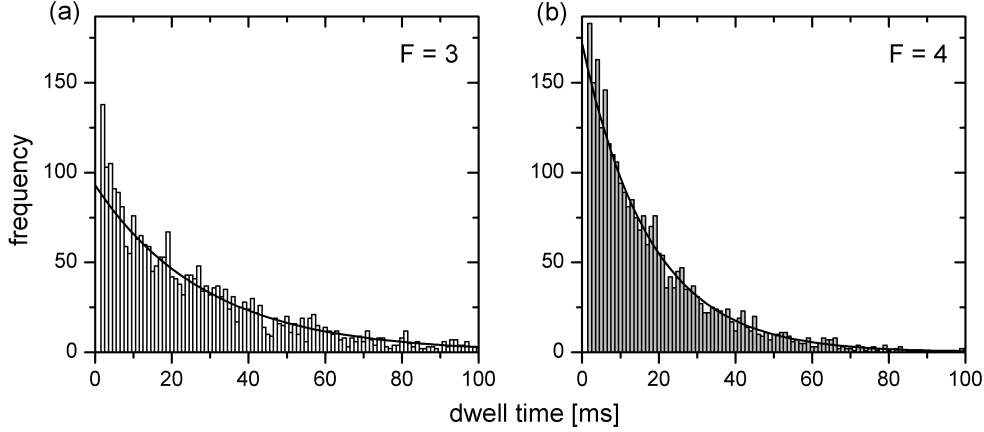


Figure 2.8: Histograms of dwell times in $|F = 3\rangle$ (a) and $|F = 4\rangle$ (b). Dwell times of 1 ms do not occur, due to smoothing of the data (see text). The black lines are fits to the data.

can then be calculated from R_{43} , $p_{F=3,ss}$, and $p_{F=4,ss}$. The obtained rates are

$$R_{43} = \frac{1}{\tau_{43}} = (0.072 \pm 0.002) \text{ ms}^{-1} \quad (2.8)$$

$$R_{34} = \frac{p_{F=4,ss}}{p_{F=3,ss}} R_{43} = (0.042 \pm 0.003) \text{ ms}^{-1}. \quad (2.9)$$

To verify these rates and to show that our quantum jumps are indeed described by eqs. (2.2) and (2.3) there are two predictions drawn from the rate equations that can be tested [27]:

1. The dwell times $T_{d,F}$ of the atom in state $|F = 3, 4\rangle$ follow an exponential probability density function:

$$p(T_{d,3}) = R_{34} \exp(-R_{34} T_{d,3}) \quad (2.10)$$

$$p(T_{d,4}) = R_{43} \exp(-R_{43} T_{d,4}) \quad (2.11)$$

2. The intensity auto-correlation function of the telegraph signals is given by:

$$g^{(2)}(\tau) = \frac{\langle I(t) I(t + \tau) \rangle}{\langle I \rangle^2} = 1 + \frac{R_{34}}{R_{43}} \exp(-(R_{34} + R_{43}) \tau) \quad (2.12)$$

The histograms of dwell times are shown in fig. 2.8. In order to compute the histograms, I have first digitized the trajectories: All photon numbers above the threshold are set to one, all below the threshold to zero. In this digitization, two directly subsequent changes in transmission are smoothed out: If a zero occurs between two ones, it is also set to one, and vice versa. This is because the chance that the middle value occurred due to a measurement error is much higher (2.4%) than the chance of two quantum jumps occurring directly after each other

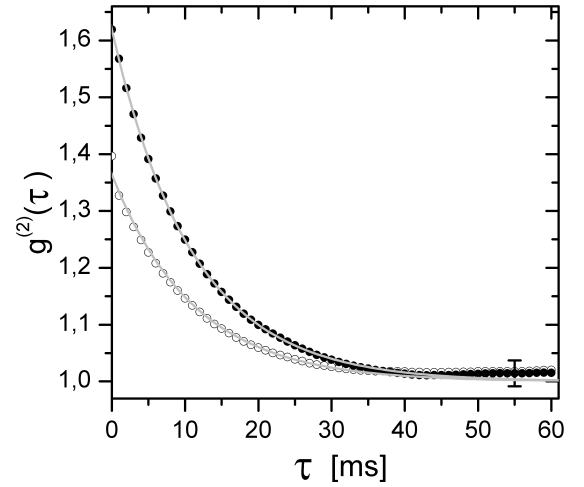


Figure 2.9: Second order intensity auto-correlation function of random telegraph signals, calculated from the original data (\circ) and from the digitized data (\bullet). The solid gray lines are best fits to the data. The deviation from the theoretically expected value 1 for large τ is within the statistical error. For better visibility of the data only one error bar is plotted.

(0.3%). The dwell time histograms are computed from the digitized signals by counting the number of subsequent zeros and ones. Although the 1 ms dwell times have been eliminated in the process of digitization, the histograms are still biased by dwell times occurring due to measurement errors. This can be seen from the fact that the decay constants of the fitted exponentials depend strongly on the range of data used for the fit. If short dwell times are excluded, the decay constants decrease. After dwell times up to 6 ms have been excluded, the decay constants do not change significantly any more and are taken as the jump rates. The resulting rates are

$$R_{43} = (0.057 \pm 0.001) \text{ ms}^{-1} \quad (2.13)$$

$$R_{34} = (0.035 \pm 0.001) \text{ ms}^{-1}. \quad (2.14)$$

They are a factor of about 0.8 lower than the rates obtained from the ensemble average of single jumps directly after the atomic insertion given in eqs. (2.8) and (2.9). A similar difference has been observed in earlier quantum jump measurements with our setup [28]. There are two possible explanations of this difference. Smoothing out two directly subsequent jumps as described above also prolongs other dwell times. This happens if two intervals, during which the atom is in one state, are interrupted by two real subsequent jumps. If these are smoothed out, two short intervals are connected to a longer one. This should lead to a slower decay of the dwell time histograms and thus to slightly shorter rates. Another reason might be that there are physical processes connected to the insertion of the atom into the resonator light field that cause the jump rate to be shorter directly after insertion and then to increase. It might be for example that directly after insertion it takes some time for the atom to be cooled to a position of strong effective coupling. Since at the chosen detuning of 38 MHz the jump rate decreases with increasing coupling, this could explain a larger rate shortly after insertion (see fig. 2.4(b)).

The smaller jump rates extracted from the histograms of dwell times are confirmed by the analysis of the second order intensity auto-correlation function $g^{(2)}(\tau)$. I have computed the

$g^{(2)}(\tau)$ from the original as well as from the digitized data. The results are shown in fig. 2.9. Obviously, the correlation function computed from the digitized data lies above the correlation function computed from the original data. This has two reasons: First, the measured transmission does not go down to zero during the dark intervals, while the digitized signal is indeed set to zero. This increases the contrast of the digitized signals compared to the measured transmission signals, which in turn leads to a higher intensity correlation. Second, non-Poissonian noise caused by variations of the effective coupling strength reduces the correlations. Since the form of $g^{(2)}(\tau)$ given in eq. (2.12) is calculated for a telegraph signal varying between 0 and 1, it has to be compared to the digitized data. Fitting the theoretical function from eq. (2.12) to the correlation function of the digitized data yields the rates

$$R_{43} = (0.056 \pm 0.001) \text{ ms}^{-1} \quad (2.15)$$

$$R_{34} = (0.034 \pm 0.001) \text{ ms}^{-1}. \quad (2.16)$$

They agree with the rates found from the dwell time histograms and confirm the difference with the rates from the independent R_{43} measurement.

Every quantum jump from $|F = 4\rangle$ to $|F = 3\rangle$ goes together with the emission of a photon on the $|F' = 4\rangle \rightarrow |F' = 3\rangle$ or $|F' = 3\rangle \rightarrow |F' = 3\rangle$ transition. Since we are working with a single atom, these photons and thus the corresponding jumps should exhibit anti-bunching [26]. In other words, the probability to find two jumps from $|F = 4\rangle$ to $|F = 3\rangle$ directly after each other should be zero. To show that this is indeed the case, I calculate the second order auto-correlation function of the jump instants $g_j^{(2)}(\tau)$, which is proportional to the probability to find a jump at time $t = \tau$ if a jump occurred at $t = 0$. Figure 2.10(a) depicts $g_j^{(2)}(\tau)$. The theoretically expected time dependence is [29, 30]

$$g_j^{(2)}(\tau) = 1 - \exp(- (R_{43} + R_{34}) \tau). \quad (2.17)$$

Fitting this function to the experimental data yields $(R_{43} + R_{34}) = 0.08 \pm 0.01$, which agrees with the rates found from the dwell time histograms and the intensity correlation function. This anti-bunching should also lead to sub-Poissonian counting statistics of the quantum jumps. A histogram of the number of jumps n_j from $|F = 4\rangle$ to $|F = 3\rangle$ during $\Delta t = 100\text{ms}$ is shown in fig. 2.10(b). A Poissonian distribution with the same mean as the experimental distribution shown as a black line clearly does not fit the data. The deviation from a Poissonian distribution can be quantified with Mandel's Q parameter [31]

$$Q = \frac{\langle (\Delta n_j)^2 \rangle - \langle n_j \rangle}{\langle n_j \rangle}. \quad (2.18)$$

For a Poissonian distribution this parameter is zero, while for a sub-Poissonian, i.e. quenched, distribution it is negative and for a super-Poissonian, i.e. broadened, distribution it is positive. For the experimentally found distribution this parameter is $Q = -0.42$ confirming the anti-bunching. The theoretically expected value of the Q parameter can be calculated from the

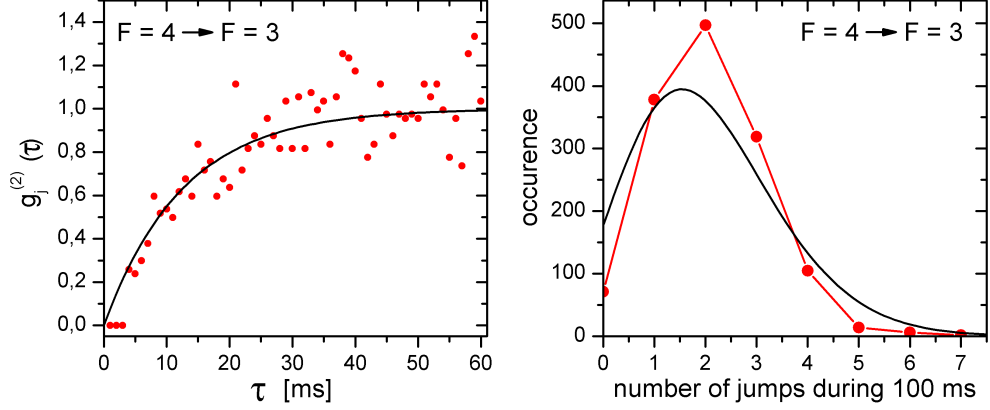


Figure 2.10: (a): Second order auto-correlation function of the instances of quantum jumps from $|F = 4\rangle$ to $|F = 3\rangle$ (red dots). The black line shows a fit of the theoretically expected function to the data. That the first three points are exactly zero is due to smoothing out the 1 ms dwell time intervals. These points are not taken into account for the fit. (b): Histogram of the number of jumps during 100 ms. The distribution is sub-Poissonian with $Q = -0.42$ (red dots). The black line shows a Poissonian distribution with the same mean as the actual distribution (2.06).

second order jump correlation function via [31]

$$Q(\Delta t) = \frac{2 N_j}{T \Delta t} \int_0^{\Delta t} dt' \int_0^{t'} \left(g_j^{(2)}(\tau) - 1 \right) d\tau. \quad (2.19)$$

Here, N_j is the total number of $|F = 4\rangle$ to $|F = 3\rangle$ jumps in all traces, T is the total duration of all traces and Δt is the time interval in which the jumps are counted. For $\Delta t = 100$ ms eq. (2.19) yields $Q = -0.45$, which agrees with the value of $Q = -0.42$ calculated from the experimental distribution.

The analysis of single atom quantum jumps in this section shows that we have a clean and well characterized system exhibiting all the known properties of quantum jumps. These have already been observed in a number of different systems [32–37] and are not new in themselves. In the previous experiments, the state measurement is done via fluorescence detection relying on photon scattering. In our experiment, however, the state detection method does not rely on photon scattering, but on coherent, dispersive interaction. Thus, in principle the atomic state can be detected without destroying its phase. This opens intriguing possibilities especially when working with several atoms in the resonator at a time, since the number of coupled atoms could be determined without destroying coherent superpositions of internal states. First experiments into this direction are presented in the following section.

2.3 Quantum Jumps of Two Atoms Coupled Simultaneously to the Resonator

A measurement allowing to determine the internal state population for more than one atom without scattering a single photon opens exciting possibilities for the probabilistic preparation of atoms in squeezed and entangled states [3, 38, 39]. Such a measurement has recently been realized for an ensemble of several hundred thousand atoms trapped in free space, i.e. without using a resonator to enhance the coherent atom light coupling strength [1]. In the absence of a resonator, the large atom number is necessary to achieve a measurement signal significantly above the technical noise.

Squeezed states of large atomic ensembles are especially useful in metrology. For quantum information purposes, however, it is desirable to prepare entangled states of a small number of individually addressable atoms [40]. To realize a scattering free population measurement for such a small number of atoms, the atom light coupling strength has to be enhanced by an optical resonator.

In principle our experimental setup provides all necessary means to entangle two neutral atoms. We can trap individual atoms, control their positions and internal states. And we have a high finesse optical resonator that should in principle allow to perform a measurement of the population of a particular internal state for two atoms without photon scattering. In this section, I will present a measurement of the number of caesium atoms in $|F = 4\rangle$ for two atoms in the resonator, which is an extension of the state detection method described above. I will evaluate the performance of this measurement by investigating random telegraph signals from two atom quantum jumps in the resonator. I will estimate, how close this measurement is to a scattering free measurement.

2.3.1 Distinction of One and Two Atoms Coupled to the Resonator

In order to distinguish one atom in $|F = 4\rangle$ from zero *as well as from two* atoms in $|F = 4\rangle$, the experimental parameters have to be chosen such that the transmission levels TL_0 , TL_1 , and TL_2 for zero, one and two atoms can be equally well separated. The reader may be reminded here that the transmission level is the intensity transmitted through the resonator normalized to its value for an empty cavity, implicating that $TL_0 = 1$. Neglecting slight differences in shot noise, the best separation is obtained if TL_0 , TL_1 , and TL_2 are equally spaced. From eq. (1.13) one finds that equally spaced transmission levels are obtained if the difference of the one and two atom levels $\Delta TL_{12} = TL_1 - TL_2$ is at its maximum of 33%. This maximum separation is obtained for $g_{\text{eff}}^2/\kappa\Delta_{\text{ca}} = 1/\sqrt{2}$ and $\Delta_{\text{pc}} = 0$. Experimentally we can control the effective coupling strength g_{eff} , as well as the cavity-atom detuning Δ_{ca} . The control of g_{eff} is achieved via controlling the distance Δx of the atom from the cavity center, since the gaussian mode profile implicates an exponential decay of the effective coupling strength with Δx . Figure 2.11(b) depicts ΔTL_{12} as a function of Δ_{ca} and Δx in units of the cavity mode

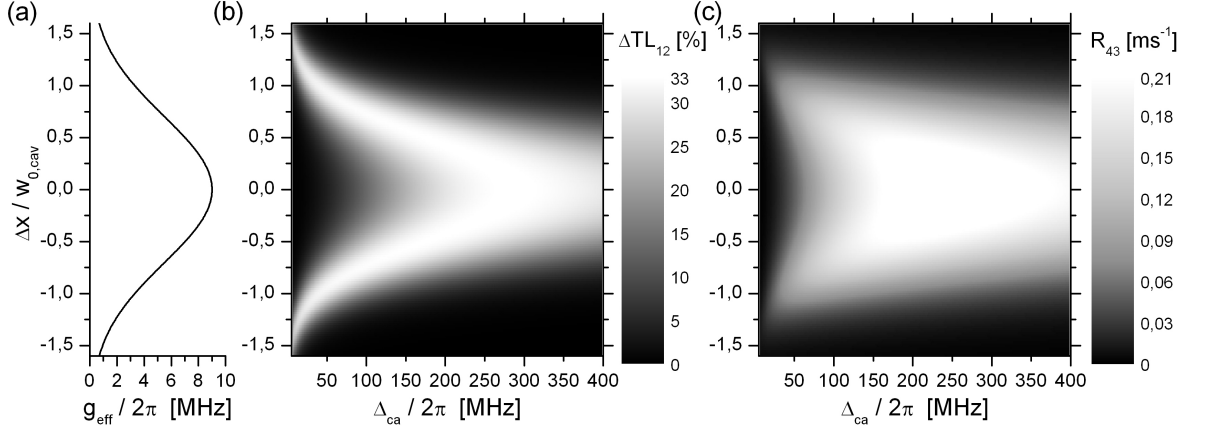


Figure 2.11: (a) Effective coupling strength as a function of the cavity mode waist $\Delta x/w_{0,\text{cav}}$. Adjusting Δx allows to control g_{eff} . The effective single atom coupling strength at the center of the resonator is assumed to be 9 MHz (see text). (b) and (c): Calculated one- and two-atom transmission level difference ΔTL_{12} and jump rate R_{43} as a function of cavity-atom detuning and $\Delta x/w_{0,\text{cav}}$. The maximum transmission level difference of 33% can be obtained for all detunings below 280 MHz by moving the atoms away from the cavity center. R_{43} decreases for small Δ_{ca} due to a stronger suppression of the intra cavity intensity.

waist $w_{0,\text{cav}}$. For the calculation I have assumed an effective single atom coupling strength at the cavity center of $g_{\text{eff}}(\Delta x = 0) = 2\pi \times 9$ MHz, based on the transmission level measurements depicted in fig. 2.4(a). The effective coupling strength as a function of $\Delta x/w_{0,\text{cav}}$ is shown in fig. 2.11(a). The atoms are assumed to be independent so that each atom couples with the same effective coupling strength. Optimum distinction can be achieved for all $\Delta_{\text{ca}} \leq 2\pi \times 280$ MHz. The smaller Δ_{ca} , the farther away the atoms have to be from the cavity center.

Since the measurement signal ΔTL_{12} does not depend on g_{eff} and Δ_{ca} separately but only on the ratio $g_{\text{eff}}^2/\Delta_{\text{ca}}$, these parameters can be adjusted to minimize the disturbance of the atomic state by the measurement. As explained in section 2.1 inelastic Raman scattering induces quantum jumps of the internal atomic state from $|F = 4\rangle$ to $|F = 3\rangle$ at a rate R_{43} . This jump rate is plotted in fig. 2.11(c) for the same range of Δ_{ca} and Δx as ΔTL_{12} . Comparing the two figures, it can be seen that along the regions of maximum ΔTL_{12} , the jump rate R_{43} decreases continuously with decreasing Δ_{ca} . This is due to the stronger suppression of the intra cavity intensity for small cavity-atom detunings. Conditional squeezing and entanglement generation proposals as described in [3, 38] require, however, not only the absence of state changing photon scattering, but of any photon scattering at all. The total scattering rate is dominated by scattering on the $|F = 4\rangle \rightarrow |F' = 5\rangle$ transition, which is least detuned from the cavity resonance. For a fixed intra cavity intensity the total scattering rate decreases with the usual factor $1/\Delta_{\text{ca}}^2$ [26]. Thus given optimal transmission level separation, the *total* scattering rate is minimized for a large detuning and a large effective coupling strength, while the *state changing* scattering rate is minimized for a small detuning and a reduced effective coupling strength. When aiming at the generation of entangled states, the total scattering rate has to be reduced

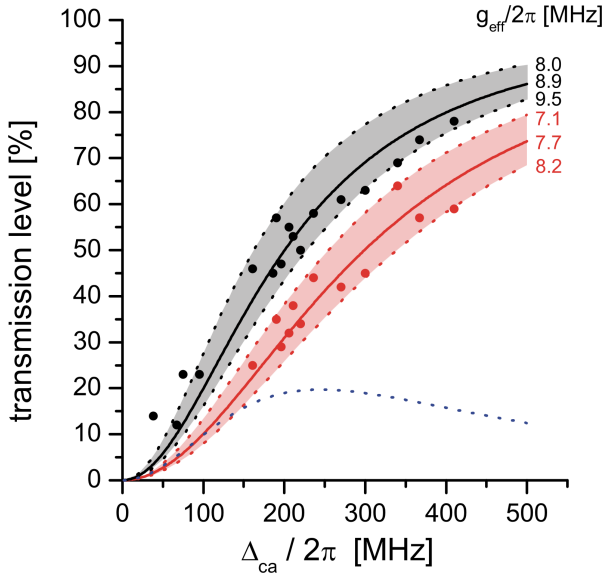


Figure 2.12: Transmission levels measured for 1 (black dots) and 2 (red dots) atoms in $|F = 4\rangle$ coupled to the resonator. The one atom data are the same as shown in fig. 2.4. The solid lines are best fits to the data. (see section 2.1.1). The largest measured transmission level difference is obtained for detunings between 250 and 300 MHz. The maximum difference between the calculated best-fit transmission levels (dashed blue line) is found at slightly lower detunings.

even further. This can be done by increasing Δ_{ca} beyond 280 MHz at the cost of a smaller ΔTL_{12} . This regime is not experimentally investigated here, but it is discussed theoretically in chapter 3.

As a preparation of the two-atom state population measurement, we have investigated the agreement of our experimental system with the theoretical expectations described above. First, we have measured the one and two atom transmission levels as a function of detuning for both atoms at the center of the resonator. The results are depicted in fig. 2.12. The one atom data are the same as shown in fig. 2.4. The two-atom transmission level has always been recorded immediately after the one-atom transmission level to have the experimental conditions as similar as possible. As in fig. 2.4 the solid lines are theoretical calculations where the effective single-atom coupling strength is used as a fit parameter (see section 2.1.1). For two atoms, the total coupling strength is calculated via eq. (1.12). By post selection, traces where the separation of the two atoms is larger than $10 \mu\text{m}$ are excluded from the analysis. The transport distance is chosen such that the two atoms are at equal distances from the cavity center. The best agreement between the two-atom data and theory is obtained for an effective single-atom coupling strength of $g_{\text{eff}} = 2\pi \times 7.7 \text{ MHz}$. The coupling strength expected from the one-atom data and the spatial separation of the atoms can be calculated via eq. (1.20). A maximal distance of each atom from the cavity center of $5 \mu\text{m}$ results in a single atom effective coupling strength $g_{\text{eff}} = 8.5 \text{ MHz}$. Why the fitted value of $g_{\text{eff}} = 2\pi \times 7.7 \text{ MHz}$ lies significantly below the expected coupling strength cannot be explained by the rather simplified theory used for the fits. The largest transmission level difference is obtained for detunings between 250 and 300 MHz. This agrees with the theoretically expected 280 MHz. The difference between the theoretical best-fit transmission levels is depicted as a dashed blue line in fig. 2.4. Its maximum is found slightly below 280 MHz, because g_{eff} is lower for the two-atom measurements than for the one-atom measurements.

The dependence of the one and two atom transmission levels on the distance Δx from the cavity center has already been measured in earlier experiments [41]. We have not repeated these measurements in the context of this investigation.

The jump rate as a function of cavity-atom detuning has already been shown in fig. 2.4. It has been found to agree with the theoretical expectations. It would have been interesting to experimentally verify the calculated dependence of the jump rate R_{43} on Δx for a fixed, small Δ_{ca} , where R_{43} should exhibit a local minimum at the cavity center (see fig. 2.11(c)). We have measured R_{43} for $0 \leq \Delta x \leq w_{0,\text{cav}}$ but could not find a significant dependence of R_{43} on Δx . This is again an indication for motional dynamics of the atom that are not understood. For example, the cavity cooling mechanism might work better further away from the cavity center, leading to a slower decrease of g_{eff} for increasing Δx . In this case, the local minimum of the jump rate would be broadened. Such a broadening could explain why the minimum could not be resolved for $0 \leq \Delta x \leq w_{0,\text{cav}}$.

2.3.2 Atom Number Dependent Quantum Jump Rate

The nondestructive detection of the population of the $|F = 4\rangle$ state allows the observation of quantum jumps for two atoms coupled to the resonator. These quantum jumps are best observed at low detunings and the atoms positioned about one waist away from the cavity center. As explained above, this yields optimum transmission level distinction and at the same time a rather low jump rate. As for the observation of single atom quantum jumps we have chosen a cavity-atom detuning of 38 MHz as a relatively low detuning that still yields rather stable transmission levels. The distance from the cavity center has been adjusted for optimum distinction of one and two atoms. Examples of consecutive quantum jumps of two atoms from $|F = 4\rangle$ to $|F = 3\rangle$ are shown in fig. 2.13. These traces are obtained by placing two atoms prepared in $|F = 4\rangle$ (21 ± 1) μm away from the cavity center. The data are post selected for atom pairs with an inter atom spacing of less than 2 μm . No repumper is applied during the first 170 ms of these measurements so that only quantum jumps from $|F = 4\rangle$ to $|F = 3\rangle$ can occur. The transmission drop upon the activation of the repumper after 170 ms verifies that both atoms are still coupled to the resonator field. The one- and two-atom transmission levels can clearly be distinguished. Obviously, the separation of the two transmission levels is even better than the theoretically expected maximum of 33%. This is true not only for the selected shots shown in fig. 2.13, but for most of the measured traces. It indicates that the effective coupling strengths of the two atoms are different or that they change upon the first jump.

The dynamics of these two atom quantum jumps are governed by the following system of

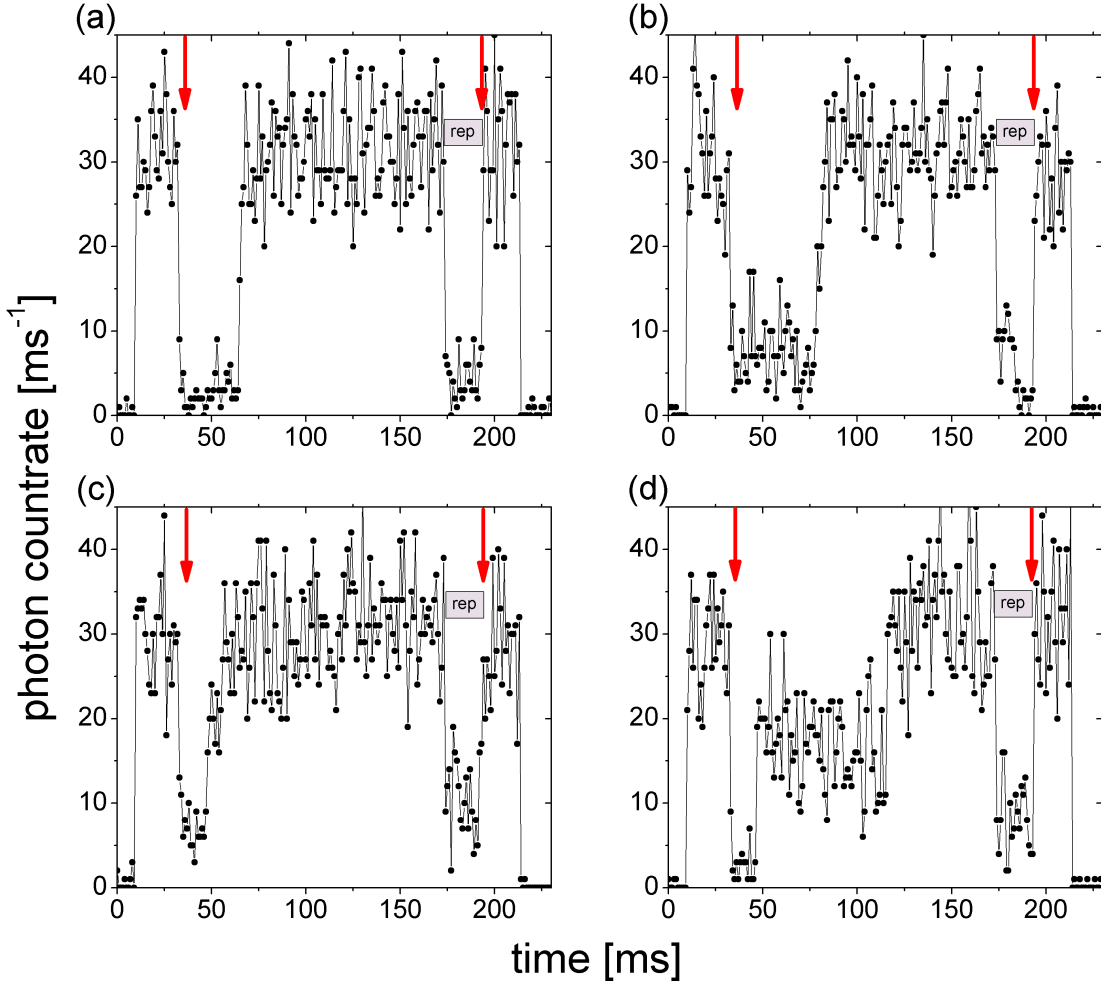


Figure 2.13: Transmission traces obtained for two atoms, prepared in $|F = 4\rangle$ that are placed $(21 \pm 1) \mu\text{m}$ away from the cavity center. Since for the first 170 ms no repumper is applied, only quantum jumps from $|F = 4\rangle$ to $|F = 3\rangle$ can occur. After 170 ms the repumper is switched on to verify that both atoms are still coupled to the resonator field. The arrows indicate the insertion and retrieval of the atoms from the cavity.

rate equations:

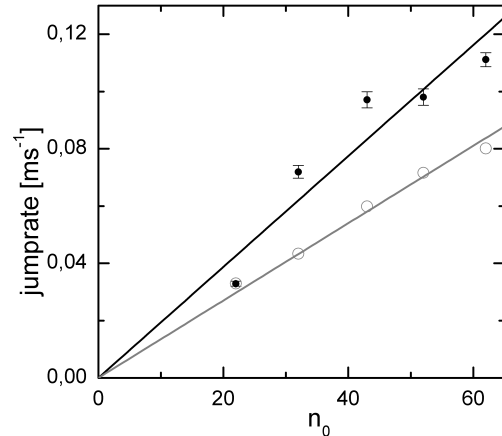
$$\frac{dp_0}{dt} = R_{10}p_1(t) \quad (2.20)$$

$$\frac{dp_1}{dt} = R_{21}p_2(t) - R_{10}p_1(t) \quad (2.21)$$

$$\frac{dp_2}{dt} = -R_{21}p_2(t) \quad (2.22)$$

Here, p_N is the probability for N atoms to be in $|F = 4\rangle$. R_{10} is the rate at which N decreases from 1 to 0 and equals the rate R_{43} of quantum jumps from $|F = 4\rangle$ to $|F = 3\rangle$. Similarly, R_{21}

Figure 2.14: Single atom jump rate as a function of the number of photons n_0 detected behind the empty cavity during the measurement time t_m (black dots). n_0 is proportional to the intra cavity intensity. The measured data lie significantly above the theoretically expected values (gray circles). The effective coupling strengths used in the calculations are extracted from the initial transmission level of the jump traces (see text). Slight variations of these effective coupling strengths lead to deviations from the linear dependence also for the calculated rates. The solid lines are linear fits.



is the rate at which the $|F = 4\rangle$ population decreases from 2 to 1. This rate is *not* simply given by $2 R_{10}$, because the intra cavity photon number for $N = 2$ is lower than for $N = 1$. I have measured R_{43} as a function of n_0 , the number of photons detected behind the resonator if no atom is coupled to the cavity light field. n_0 is proportional to the intra cavity photon number.

The data are shown in fig. 2.14 together with rates calculated from the initial average transmission level. The effective coupling strength used for the calculation was determined from the average transmission level directly after insertion of the atom into the resonator. Slight variations of these effective coupling strengths lead to deviations from the linear dependence also for the calculated rates. Apart from the jump rate at $n_0 = 20$ the measured rates lie significantly above the theoretically expected values. This might be due to a decrease of the effective coupling strength over time, since at low detunings the jump rate increases with decreasing effective coupling strength (see fig. 2.4). Moreover, as discussed in section 2.1.1 and Appendix A the simplifying assumption that the atom is always in the outermost Zeeman sub-level systematically underestimates the jump rate. The deviations of the measured data from the fitted linear dependence are also significantly larger than expected from the variations of the effective coupling strengths. These deviations are not understood. They might be due to variations in the temperature of the atoms caused by experimental imperfections such as noise of the resonator servo loop. However, since the deviations from the linear fit appear to be random, a linear dependence of the jump rate on the intra cavity photon number as theoretically expected seems a reasonable assumption. With this assumption R_{21} is given by

$$R_{21} = 2 \frac{\text{TL}_2}{\text{TL}_1} R_{10}. \quad (2.23)$$

Thus, the time dependence of the average transmission, i.e. the ensemble average of many individual quantum jump traces as shown in fig. 2.13 can be predicted from the single atom quantum jump rate $R_{10} = R_{43}$ and the ratio of the transmission levels for one and two atoms.

The ensemble average of 169 individual two-atom traces is shown in fig. 2.15 together with the ensemble average over 227 traces where only a single atom was placed in the resonator mode. To compare the data to the predictions according to the rate equations, I have solved

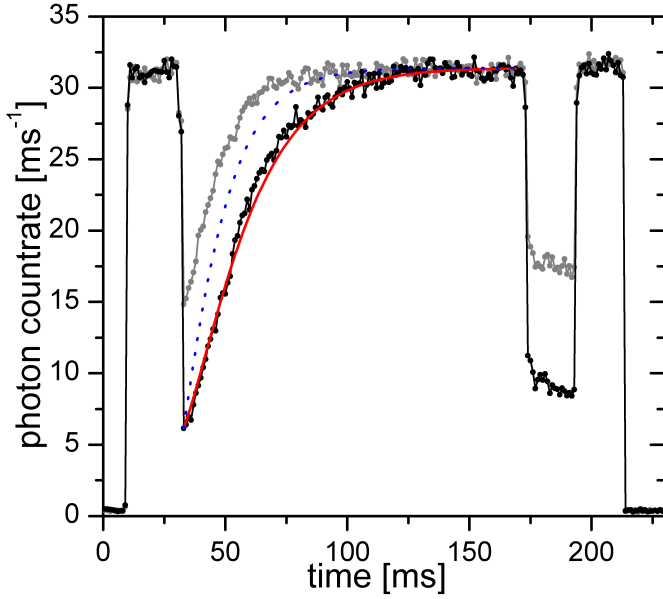


Figure 2.15: Ensemble average of 169 two-atom transmission traces without repumper (black dots). The observed dynamics is well explained by a parameter free model (red line), taking into account the atom number dependent jump rate (see text). The single atom jump rate used for the theoretical curve is determined from the ensemble average of 227 single atom quantum jump traces (gray dots). The time dependence of the blue curve would be expected, if both atoms would jump with the same rate R_{43} . Switching on the repumper after 170 ms verifies that the atoms have not been lost from the cavity.

the rate equations for the initial condition $p_2(t=0) = 1$ and calculated the time dependent average transmission level $\langle \text{TL} \rangle(t)$. It is given by

$$\langle \text{TL} \rangle(t) = \text{TL}_0 p_0(t) + \text{TL}_1 p_1(t) + \text{TL}_2 p_2(t) \quad (2.24)$$

$$\begin{aligned} &= \text{TL}_0 + \frac{(\text{TL}_0 - \text{TL}_1) \text{TL}_2}{\text{TL}_1 - \text{TL}_2} \exp(-R_{10}t) \\ &+ \left(\text{TL}_2 + \frac{(\text{TL}_2 - \text{TL}_0) \text{TL}_1}{\text{TL}_1 - \text{TL}_2} \right) \exp\left(-\frac{\text{TL}_2}{\text{TL}_1} R_{10}t\right). \end{aligned} \quad (2.25)$$

$\langle \text{TL} \rangle(t)$ is plotted as a red line in fig. 2.15. For the calculation R_{10} has been obtained from an exponential fit of the ensemble average of the single atom traces. The transmission level ratio TL_2/TL_1 has been determined from the measured average transmission levels directly after insertion of the atoms into the resonator. This parameter free model agrees well with the measured data. Between 50 ms and 75 ms the data lie significantly above the theoretically expected transmission. This reflects the fact that the observed separation between the one- and two-atom transmission levels observed in the individual traces is better than the theoretically expected 33%. As stated above, this might be due to a decrease of the coupling strength over time caused by heating of the atoms in the resonator. The dashed blue line shows the time dependent average transmission level calculated from eq. (2.25) for $R_{21} = 2 R_{10}$. It clearly does not fit the data and shows that the jump rate depends indeed via the intra cavity intensity on the number of atoms coupled to the resonator.

2.3.3 Two-Atom Random Telegraph Signals

At the same cavity-atom detuning, distance from the cavity center, and inter atom spacing, we have recorded 400 ms long random telegraph signals by monitoring the cavity transmission while a weak repumping laser is applied from the side of the resonator. An example trace is shown in fig. 2.16(a). In some parts of the trace, three different transmission levels can clearly be recognized. On the whole, the noise is too strong to determine the population of the $|F = 4\rangle$ state from a single 1 ms transmission measurement with good efficiency. It is, however, possible to give after each 1 ms transmission measurement a probability p_N for each possible value of N based on the rate equations and the history of the measurement record. The rate equations describing the dynamics of the telegraph signals differ from eqs. (2.20)–(2.22) only by the contribution from the repumper. They are given by

$$\frac{dp_0}{dt} = R_{10}p_1(t) - 2R_{\text{rep}}p_0(t) \quad (2.26)$$

$$\frac{dp_1}{dt} = 2R_{\text{rep}}p_0(t) + R_{21}p_2(t) - (R_{10} + R_{\text{rep}})p_1(t) \quad (2.27)$$

$$\frac{dp_2}{dt} = R_{\text{rep}}p_1(t) - R_{21}p_2(t). \quad (2.28)$$

Here, R_{rep} is the rate of quantum jumps from $|F = 3\rangle$ to $|F = 4\rangle$ caused by scattering of repumper photons. It is independent of N , since the repumping laser is applied from the side of the cavity. From these rate equations and the transmission measurements the probabilities $p_N(t)$ are calculated as follows: The probabilities are initially set to $p_0(0) = 0$, $p_1(0) = 0$, and $p_2(0) = 1$, since both atoms are prepared in $|F = 4\rangle$ with an efficiency close to 1 (see section 1.2.5). The probabilities after the first transmission measurement are obtained from these initial probabilities in two steps: First the expected change of the probabilities according to the rate equations is taken into account yielding the probabilities

$$\tilde{p}_0(t_m) = p_0(0) + (R_{10}p_1(0) - 2R_{\text{rep}}p_0(0))t_m \quad (2.29)$$

$$\tilde{p}_1(t_m) = p_1(0) + (2R_{\text{rep}}p_0(0) + R_{21}p_2(0) - (R_{10} + R_{\text{rep}})p_1(0))t_m \quad (2.30)$$

$$\tilde{p}_2(t_m) = p_2(0) + (R_{\text{rep}}p_1(0) - R_{21}p_2(0))t_m. \quad (2.31)$$

As previously, t_m denotes the duration of a single transmission level measurement. In a second step the outcome of the transmission measurement is accounted for by using Bayes' rule for conditional probabilities [42]:

$$p_0(t_m) = \frac{p(n|0)\tilde{p}_0(t_m)}{p(n, t_m)} \quad (2.32)$$

$$p_1(t_m) = \frac{p(n|1)\tilde{p}_1(t_m)}{p(n, t_m)} \quad (2.33)$$

$$p_2(t_m) = \frac{p(n|2)\tilde{p}_2(t_m)}{p(n, t_m)} \quad (2.34)$$

Here, n is the number of photons detected during the measurement time t_m , $p(n|N)$ is the probability to measure n photons, given that N atoms are coupled to the resonator, and $p(n, t)$ is the unconditional probability to measure n photons at time t . $p(n|N)$ and $p(n, t)$ are extracted from photon count histograms of independent transmission level measurements for zero, one and two atoms coupled to the resonator. $p(n|N)$ is the relative frequency of n photon events in the transmission traces for N coupled atoms. $p(n, t)$ is the sum of the three $p(n|N)$ weighted with the probabilities $\tilde{p}_0(t)$:

$$p(n, t) = \tilde{p}_0(t)p(n|0) + \tilde{p}_1(t)p(n|1) + \tilde{p}_2(t)p(n|2). \quad (2.35)$$

From here on, I will refer to the probability calculation procedure outlined above as the *Bayes method*². The dynamic probabilities $p_N(t)$ resulting from this method for the example trace of fig. 2.16(a) are shown in fig. 2.16(b). Of course, the noise of the transmission signals is also reflected in these probabilities. However, in contrast to the bare transmission signal these probabilities quantify the knowledge about the state of the system.

Obviously, the calculation of the probabilities $p_N(t)$ with the Bayes method requires knowledge of the jump rates R_{10} , R_{21} , and R_{rep} . A good first guess should be given by taking R_{10} from the exponential fit of the ensemble average of single atom quantum jump traces without repumper. R_{21} should then be given by the ratio TL_2/TL_1 taken from independent transmission level measurements. R_{rep} cannot be measured separately and is initially set at will to equal R_{10} . It should, however, be expected that the actual jump rates for the random telegraph signals are different. The analysis of the single atom quantum jumps has shown that the jump rates obtained from random telegraph signals can differ significantly from the rates obtained from single quantum jump averages. To find the three jump rates directly from the telegraph signals I have used the following consistency check: I have averaged the probabilities obtained with the Bayes method, using the guessed set of rates, over all traces. These averaged probabilities should follow the solution of eqs. (2.26)–(2.28) for the initial condition $p_0(0) = 0$, $p_1(0) = 0$, and $p_2(0) = 1$. I have calculated this solution using MAPLETM. A fit of this solution to the averaged probabilities with R_{10} , R_{21} , and R_{rep} as fit parameters yields a new set of rates that can be compared with the rates used for the probability calculation. By iterating the Bayes method and the fit of the rate equation solution, a self-consistent set of rates can be found. Self-consistent here means that the rates obtained from the rate equation fit are the same as those used for the Bayes method. The self-consistent set of rates resulting from this analysis is

$$R_{10} = 0.104 \text{ ms}^{-1}, \quad R_{21} = 0.052 \text{ ms}^{-1}, \quad R_{\text{rep}} = 0.045 \text{ ms}^{-1}. \quad (2.36)$$

For these rates the averaged probabilities $p_N(t)$ are plotted in fig. 2.17(a) together with the fitted solution of the rate equations. Striking is the factor of two difference between R_{21} and R_{10} , since the radial distance of the atoms from the cavity center was adjusted such that the

²Similar methods have been used in experiments in the group of S. Haroche, investigating quantum jumps of the electromagnetic field in a microwave resonator [37, 43]. Klaus Mølmer encouraged us to apply this method to our data.

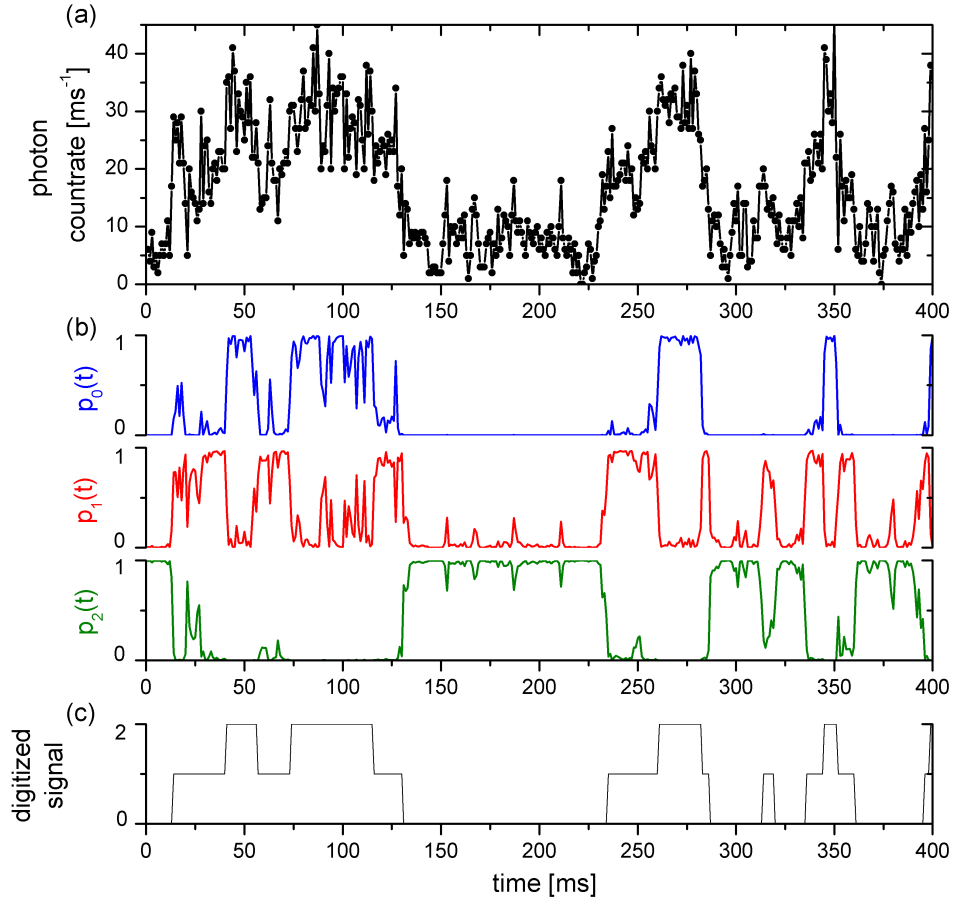


Figure 2.16: (a): Example of a random telegraph obtained for two atoms placed $21 \mu\text{m}$ away from the cavity center at a cavity-atom detuning of 38 MHz. (b): Probabilities for $N = 0, 1, 2$ atoms to be in $|F = 4\rangle$ calculated using the Bayes method (see text). (c): Digitized random telegraph signal. The digitized signal takes the value 0 if $N = 2$ has the largest probability, 1 if $N = 1$ has the largest probability, and 2 if $N = 0$ has the largest probability.

one atom transmission level is about two times the two-atom transmission level. According to eq. (2.23) this should result in approximately equal rates $R_{21} \approx R_{10}$.

To exclude systematic errors due to the algorithm of the Bayes method, I have analyzed the photon count histogram of the telegraph signals. It is shown in fig. 2.17 together with the histograms from independent transmission level measurements for zero, one and two atoms coupled to the resonator. The histogram of the telegraph signals should be a weighted sum of the independently measured histograms with weights determined by the three jump rates. The black line in fig. 2.17 shows the sum of the independent histograms weighted according to the rates from eq. (2.36). It agrees well with the histogram of the telegraph signals. Almost identical weights are obtained by fitting a weighted superposition of the transmission level histograms to the telegraph histogram with two independent weights as fit parameters. This best fit is shown as a light blue dotted line in fig. 2.17 and shows excellent agreement with the

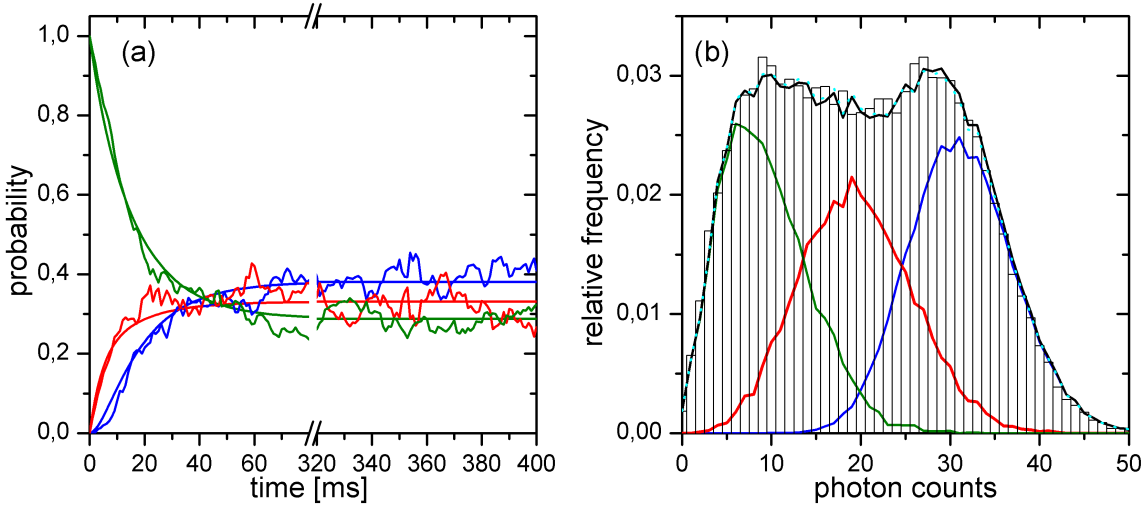


Figure 2.17: (a): Probabilities for 2 atoms (green), 1 atom (red), and 0 atoms (blue) being in $|F = 4\rangle$ calculated with the Bayes method for all individual traces and then averaged over all traces. The solid lines are best fits of the solution of the rate equations. The rates used for these plots are self-consistently obtained by alternately applying the Bayes method and the rate equation fit (see text). (b): Normalized photon count histogram of the two-atom random telegraph signals (bars) together with the independently measured histograms for 0, 1, and 2 atoms coupled to the resonator (blue, red, and green lines, respectively). The weighted sum of these independent histograms with weights taken from the self-consistent Bayes method-results (black line) agrees well with the histogram of the telegraph signals. A fit of the weighted sum of the independent histograms to the telegraph signal histogram with two independent weights yields the same result (dashed light blue line). The telegraph signals have been obtained at $\Delta_{ca} = 2\pi \times 38$ MHz and $21 \mu\text{m}$ away from the cavity center.

histogram obtained for weights from the rate equation fit. This jump rate analysis confirms the factor of two difference between R_{21} and R_{10} . It does, however, not explain this difference. On the contrary, the ratio of the average transmission levels for one and two coupled atoms calculated from the independently measured histograms in fig. 2.17 is $\text{TL}_2/\text{TL}_1 = 0.48$, as expected for optimum transmission level separation. Thus, according to the transmission levels, R_{21} should be 96% of R_{10} . This significant disagreement is not understood so far.

The self-consistent calculation of the $p_N(t)$ yields absolute numbers for the jump rates. The analysis of the countrate histograms provides an independent test of only the *relative* rates. A consistency check of the absolute values of the rates can be done by calculating the intensity auto-correlation function $g^{(2)}(\tau)$ of the two atom telegraph signals. Before this can be done, the telegraph signals have to be digitized as it was done for the single-atom telegraph signals in section 2.2. The digitization is done by setting the signal according to the value of N with the maximum probability. In accordance with the actual transmission signal, the digital signal assumes the values 0 for $N = 2$, 1 for $N = 1$, and 2 for $N = 0$. From these digitized signals I have calculated the second order intensity auto-correlation function. The result is shown in fig. 2.18 together with a theoretical calculation of the intensity correlation via the rate equations for the rates in eq. (2.36). The details of how to calculate the intensity correlation function from the rate equations is explained in Appendix B.

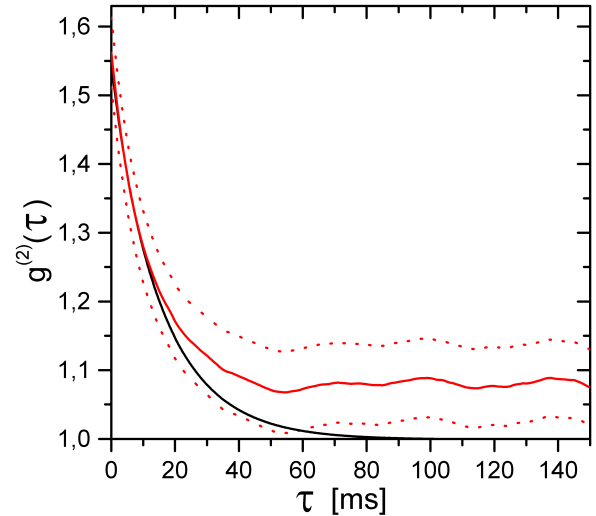


Figure 2.18: Intensity correlation function calculated from digitized two atom random telegraph signals (solid red line) and calculated from the rate equations (solid black line). The red dotted lines mark the standard deviation of $g^2(\tau)$ over the ensemble of telegraph signals.

For small τ the correlation function for the measured data and the prediction from the rate equations agree very well. For $\tau = 0$ good agreement is expected, since $g^{(2)}(\tau = 0)$ is determined by the relative steady state probabilities $p_N(t \rightarrow \infty)$, which have already been demonstrated to be in good agreement with the rate equations by the analysis of the photon count histograms. The good agreement of data and theory also for small but nonzero τ indicates the consistency of the analysis presented so far. For large τ however, the correlation function of the measured data does not decay to 1 as should be expected. This indicates that the ratios between the jump rates change from trace to trace: If the rates R_{21} and R_{10} vary from trace to trace due to variations in the effective atom-light coupling strength, the trace-to-trace variations of the probability to find a high intensity at a certain time are larger than would be expected statistically. This leads to a value above 1 of the intensity auto-correlation function at large τ , as is in detail explained in Appendix B.

The two-atom measurements presented up to here have been performed at a low cavity-atom detuning and at a distance from the cavity center. As explained above, for these parameters optimum one and two atom-distinction is achieved at a rather low quantum jump rate. This yields the least disturbance of the population by the measurement. Nevertheless, the total photon scattering rate is rather high in these experiments, because of the low detuning from the $|F = 4\rangle \rightarrow |F' = 5\rangle$ transition. While scattering on this transition cannot change the atomic groundstate, it will still destroy coherent superpositions of the two groundstates. As mentioned above, a population measurement that does not destroy such coherent superpositions would be highly desirable in order to generate entanglement between two atoms. In order to achieve this, the cavity-atom detuning should be made as large as possible. Consequently, the atoms should be placed in the center of the resonator mode, where the effective coupling strength is largest.

It can be seen from fig. 2.12 that for our system the best transmission level separation at the center of the resonator is achieved for a detuning of about 280 MHz. At this detuning we have

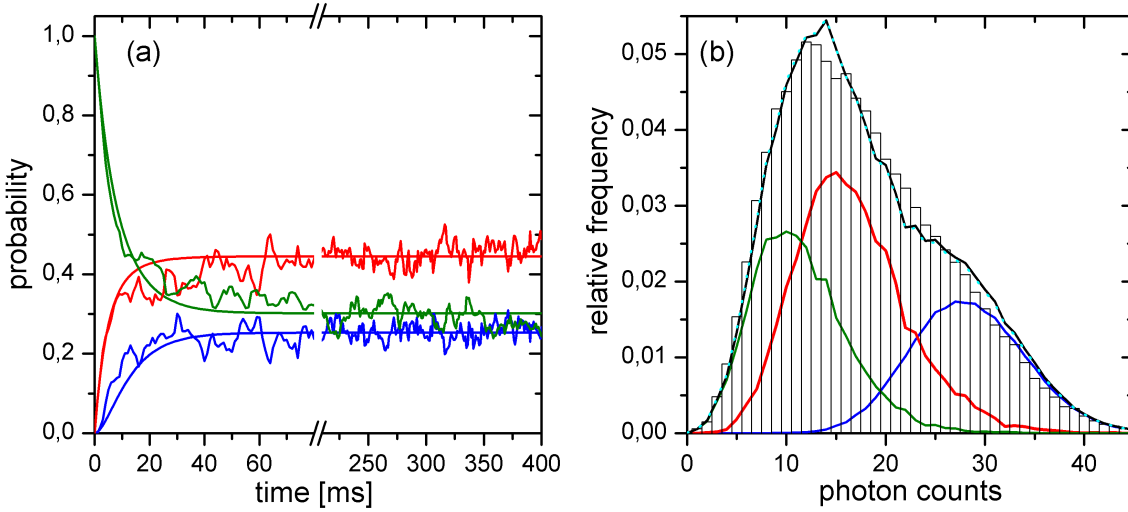


Figure 2.19: Same plots as in fig. 2.18, but here for telegraph signals obtained at $\Delta_{ca} = 2\pi \times 280$ MHz at the center of the cavity.

recorded telegraph signals, which I have analyzed in the same way as the signals obtained at the small cavity-atom detuning. Figure 2.19 shows the results of the self-consistent probability calculation and the photon count histograms. Obviously, the one and two atom transmission levels lie closer together than for the low detuning. I attribute this to a reduced single-atom effective coupling strength, if two atoms are coupled to the resonator, as already observed in the transmission level measurements in fig. 2.12. As above this can only partly be explained by the inter-atom spacing. For the telegraph signals at the center of the resonator the data was post selected for inter atom spacings $\Delta x < 10 \mu\text{m}$.

The jump rates resulting from the self-consistent Bayes method for the telegraph signals obtained at this large cavity-atom detuning are

$$R_{10} = 0.069 \text{ ms}^{-1}, R_{21} = 0.089 \text{ ms}^{-1}, R_{\text{rep}} = 0.061 \text{ ms}^{-1}. \quad (2.37)$$

Interestingly, here the value for the ratio $R_{21}/R_{10} = 1.29$ agrees much better with the ratio of the transmission levels $2 \text{ TL}_2/\text{TL}_1 = 1.39$ than in the case of low detuning.

As stated above, the detuning $\Delta_{ca} = 2\pi \times 280$ MHz minimized the total photon scattering rate, while at the same time yielding the optimum transmission level separation. However, even for this large detuning, the total photon scattering rate, calculated according to eq. (1.14) is still $R_{\text{scat}} = 21 \text{ ms}^{-1}$. Thus, during a 1 ms transmission measurement any coherent superposition of the atomic states will be destroyed with certainty. The scattering probability could be further decreased at the expense of the signal to noise ratio by detuning cavity and probe laser even further from the atomic transition. The balance between a high signal to noise ratio and a low scattering probability has to be adjusted according to the application of the measurement. One application that has been mentioned several times throughout this chapter is the generation of entangled states. In the following chapter, I describe a scheme for probabilistic

entanglement generation which is based on a nondestructive state population measurement similar to the measurements presented in this section.

3 Measurement-Induced Entanglement

In the preceding chapter I have shown how in our experiment we can nondestructively measure the population of the $|F = 4\rangle$ state for two atoms inside the resonator. Sørensen and Mølmer have suggested to use such a measurement to entangle two atoms [3]. In this chapter I will discuss the requirements for an experimental realization of this scheme. I will give an estimate of the entanglement fidelity that can be expected in our experiment under optimal conditions and discuss the most important experimental challenges.

3.1 Mølmer's Probabilistic Entanglement Scheme

Measurement-induced entanglement generation is based on the following idea: If two atoms are prepared each in a superposition of two internal states $|\phi\rangle_{1,2} = \frac{1}{\sqrt{2}}(|0\rangle_{1,2} + |1\rangle_{1,2})$ their combined state is an unentangled product state that can be written as

$$\begin{aligned} |\psi_P\rangle &= |\phi\rangle_1 \otimes |\phi\rangle_2 \\ &= \frac{1}{2} |0\rangle_1 \otimes |0\rangle_2 + \frac{1}{2} (|0\rangle_1 \otimes |1\rangle_2 + |1\rangle_1 \otimes |0\rangle_2) + \frac{1}{2} |1\rangle_1 \otimes |1\rangle_2. \end{aligned} \quad (3.1)$$

This product state differs from the entangled target state¹ $|\psi_t\rangle = \frac{1}{\sqrt{2}}(|0\rangle_1 \otimes |1\rangle_2 + |1\rangle_1 \otimes |0\rangle_2)$ because of contributions of the states $|0\rangle_1 \otimes |0\rangle_2$ and $|1\rangle_1 \otimes |1\rangle_2$. If these contributions are eliminated, the product state is transformed into an entangled state.

This can be achieved with an measurement of \hat{N} , the number of atoms in state $|0\rangle$. The components of the entangled state $|0\rangle_1 \otimes |1\rangle_2$ and $|1\rangle_1 \otimes |0\rangle_2$ are eigenstates of \hat{N} with the eigenvalue 1. $|0\rangle_1 \otimes |0\rangle_2$ and $|1\rangle_1 \otimes |1\rangle_2$ are eigenstates with the eigenvalues 0 and 2, respectively. Consequently, if a measurement of \hat{N} yields the outcome $N = 1$, the combined state of the two atoms is projected into the entangled state $|\psi_t\rangle$.

For this to work, the measurement has to fulfill two challenging requirements: On the one hand, the measurement inaccuracy has to be low. If the the measurement outcome is $N = 1$, while in fact $N = 0$ or $N = 2$, a product state will be mistaken as an entangled state. On the other hand, the measurement must not destroy the coherence of the superposition $(|0\rangle_1 \otimes |1\rangle_2 + |1\rangle_1 \otimes |0\rangle_2)$. Otherwise, even for an accurate outcome $N = 1$ the atoms would not be entangled. They would be *either* in the state $|0\rangle_1 \otimes |1\rangle_2$ *or* in the state $|1\rangle_1 \otimes |0\rangle_2$. In this sense the measurement has to be a quantum nondemolition (QND) measurement. The basic idea of the proposal in [3] is to use a high finesse optical resonator to perform this QND

¹For an introduction to the notion of entanglement see e.g. [44]

measurement.

In our system the two hyperfine groundstates of caesium $|F = 4\rangle$ and $|F = 3\rangle$ are taken as the states $|0\rangle$ and $|1\rangle$. Due to their extremely long natural lifetime they are well suited for entanglement generation. If short-lived atomic states were used, the entanglement would quickly be destroyed by the decay of the atomic excitation and could not be employed for further experiments.

In our experimental setup, the protocol for the entangling operation would be as follows: Two atoms are loaded into the standing wave optical dipole trap. In the dipole trap the atoms are pumped into the outermost Zeeman state $|F = 4, m_F = +4\rangle$ by a σ^+ polarized optical pumping laser. Then the atoms are transported into the resonator, where they are prepared in the superposition state $|\phi\rangle_{1,2} = \frac{1}{\sqrt{2}}(|0\rangle_{1,2} + |1\rangle_{1,2})$ by a microwave $\pi/2$ -pulse. After the superposition state has been prepared, a probe laser pulse is sent through the resonator. The number of atoms in $|F = 4\rangle$ is deduced from the properties of the transmitted light. For a measurement outcome $N = 1$ the two atoms are entangled, if the measurement was accurate and if the coherence of the superposition has not been destroyed by the measurement.

3.2 Fidelity of the Entanglement Operation

A measure of the quality of the entanglement operation is the *fidelity* F . In this section I will analyze this quantity and estimate the value possibly achieved with our experimental setup.

F is given by the expectation value of the density matrix $\hat{\rho}$ of the generated statistical ensemble calculated for the entangled target state

$$F = \langle \Psi_t | \hat{\rho} | \Psi_t \rangle. \quad (3.2)$$

For a pure state this reduces to the overlap of the generated state $|\Psi_g\rangle$ with the entangled state

$$F = \langle \Psi_t | \Psi_g \rangle \langle \Psi_g | \Psi_t \rangle. \quad (3.3)$$

Ideally, the generated state equals the entangled state yielding a fidelity $F = |\langle \Psi_t | \Psi_t \rangle|^2 = 1$. If errors occur due to an inaccurate measurement or decoherence, the generated ensemble is a statistical mixture yielding a fidelity of

$$F = \langle \Psi_t | (p_t |\Psi_t\rangle \langle \Psi_t| + p_{ia} (1 - p_{dec}) \hat{\rho}_{ia} + p_{dec} (1 - p_{ia}) \hat{\rho}_{dec} + p_{dec} p_{ia} \hat{\rho}_{dec,ia}) | \Psi_t \rangle. \quad (3.4)$$

Here, p_t is the probability to generate the entangled target state. p_{ia} and p_{dec} are the probabilities for an inaccurate measurement and destruction of coherence, respectively. $\hat{\rho}_{ia}$ and $\hat{\rho}_{dec}$ are the density matrices of the ensembles, generated if these errors occur. The last term $p_{dec} p_{ia} \hat{\rho}_{dec,ia}$ describes double errors, where the measurement is inaccurate *and* coherence is destroyed. $\langle \Psi_t | \hat{\rho}_{ia} | \Psi_t \rangle$ and $\langle \Psi_t | \hat{\rho}_{dec,ia} | \Psi_t \rangle$ vanish, because after an inaccurate measurement, the atoms are either in the state $|0\rangle_1 \otimes |0\rangle_2$ or in state $|1\rangle_1 \otimes |1\rangle_2$, which both do not overlap with the entangled state. $\langle \Psi_t | \hat{\rho}_{dec} | \Psi_t \rangle$ is not easy to calculate, because it depends on the details of the decoherence process. If decoherence occurs due to inelastic, state-changing Raman

scattering, the atoms end up in one of the states $|0\rangle_1 \otimes |0\rangle_2$ or $|1\rangle_1 \otimes |1\rangle_2$, or even in some other state, which all have no overlap with the entangled state. If, however, decoherence occurs due to dephasing or elastic Rayleigh scattering, the atoms end up in a statistical mixture of $|0\rangle_1 \otimes |1\rangle_2$ and $|1\rangle_1 \otimes |0\rangle_2$, having an overlap of 50% with the entangled state. For simplicity, I assume that also in the case of decoherence the generated state has no overlap with the entangled state. Then from eq. (3.4) one obtains a lower limit on the fidelity of

$$F \geq p_t = 1 - p_{ia} - p_{dec} + p_{ia} p_{dec}. \quad (3.5)$$

Note that even the *unentangled* product state (3.1), has an overlap of 50% with the desired entangled state. Consequently, a fidelity of 50% can always be achieved by *guessing* N instead of measuring it. Therefore, I will refer to a fidelity of 50% as the classical threshold for the fidelity. In the following I will estimate p_{dec} and p_{ia} in order to quantify the fidelity.

Decoherence: The most severe source of decoherence is spontaneous photon scattering. This can be understood as follows: For the entanglement scheme considered here it is essential that one of two atomic ground states couples much stronger to the resonator light field than the other and affects the transmitted light stronger. Only then is it possible to deduce the population of the two states from the transmitted light. The strongly coupled atom is of course much more likely to scatter a photon than the weakly coupled one. If now the two atoms are separated by more than half of the wavelength of the scattered light, each scattered photon can in principle be attributed to one of the atoms. A single scattered photon thus projects the atom that has scattered into the strongly coupling state, destroying coherent superposition of the entangled state.

In the weak excitation limit, the scattering rate for a two level atom inside the resonator is given by [3]

$$R_{scat} = \frac{\Gamma n_1}{\eta t_m \kappa} \frac{g^2}{(\Gamma^2/4 + \Delta^2)} \stackrel{\Delta \gg \Gamma}{\approx} \frac{\Gamma n_1}{\eta t_m \kappa} \frac{g^2}{\Delta^2}. \quad (3.6)$$

As in the previous chapter, t_m is the duration of the measurement and n_1 denotes the number of photons that are transmitted and detected during t_m , if one atom is coupled to the resonator. η is the photon detection efficiency. Entanglement can only be created, if the measurement time is much smaller than the inverse scattering rate. In this case the probability of scattering during the measurement is given by

$$p_{scat} = 1 - \exp(-t_m R_{scat}) \approx \frac{\Gamma n_1}{\eta \kappa \Delta^2} g^2. \quad (3.7)$$

Measurement inaccuracy: The probability of an inaccurate measurement p_{ia} is given by

$$p_{ia} = \frac{\int_{S_1 - \Delta S/2}^{S_1 + \Delta S/2} \left(\frac{1}{4} p_0(S) + \frac{1}{4} p_2(S) \right) dS}{\int_{S_1 - \Delta S/2}^{S_1 + \Delta S/2} \left(\frac{1}{4} p_0(S) + \frac{1}{2} p_1(S) + \frac{1}{4} p_2(S) \right) dS}. \quad (3.8)$$

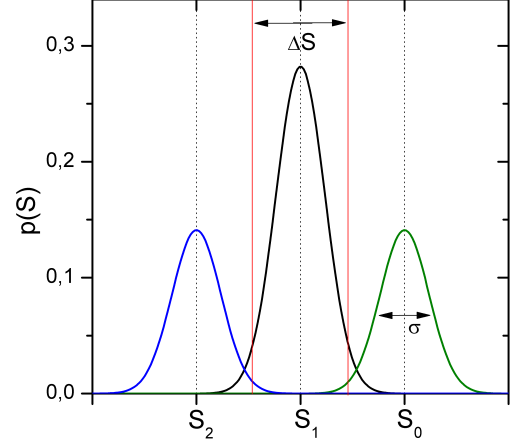


Figure 3.1: Schematic plot of the probability distribution of the measurement signal for zero (green), one (black) and two (blue) atoms coupled to the resonator, weighted according to the structure of the initial product state (see text).

Here S denotes the measured signal observable and ΔS is the interval of values of S that are attributed to the measurement outcome $N = 1$. $p_N(S)$ is the probability distribution of S obtained for N atoms coupled to the resonator. The weight factors $\frac{1}{4}$ and $\frac{1}{2}$ come from the fact that the measurement outcome $N = 1$ occurs two times as often as $N = 0, 2$, due to the structure of the two-atom product state (see eq. (3.1)). It can be seen from eq. (3.8) that the upper limit of p_{ia} is $1/2$, obtained if no information on N is obtained ($p_0(S) = p_1(S) = p_2(S)$). This yields the classical threshold for the fidelity of 50% introduced at the beginning of this section.

Apparently, p_{ia} depends on the size of the acceptance interval ΔS . The smaller ΔS , the larger the achieved fidelity. A small ΔS , however, decreases the success probability p_s of finding the outcome $N = 1$ and thus the rate at which entangled atom pairs can be created. The success probability is given by

$$p_s = \int_{S_1 - \Delta S/2}^{S_1 + \Delta S/2} \left(\frac{1}{4} p_0(S) + \frac{1}{2} p_1(S) + \frac{1}{4} p_2(S) \right) dS. \quad (3.9)$$

Experimentally, a low success probability is a challenge, since measurements that investigate the nonclassical character of entangled states have to be done on an ensemble of atom pairs. Thus, the lower the rate of entanglement generation, the higher the requirements concerning the longterm stability of the experiment. Here, I first want to find the highest possible fidelity. Thus, I consider the limit of $\Delta S \rightarrow 0$. Apart from ΔS , p_{ia} depends also on the distribution of the measurement noise $p_N(S)$. For the detection schemes discussed in the subsequent section the ideal shot noise limited noise distribution is either gaussian or poissonian (which can be well approximated by a gaussian for $n_1 \gtrsim 5$) and has the same width σ for $N = 0, 1, 2$ (see section 3.3)

$$p_N(S) = \frac{1}{\sigma_N \sqrt{2\pi}} \exp \left(-\frac{1}{2} \left(\frac{S - S_N}{\sigma} \right)^2 \right). \quad (3.10)$$

Here, S_N is the expectation value of S , if N atoms are coupled to the resonator. I define the

signal to noise ratio for the distinction of one coupled atom from N coupled atoms as follows:

$$\text{SNR}_N := \frac{|S_1 - S_N|}{\sigma} \quad (3.11)$$

In section 3.3 it will be shown that the best fidelity is achieved in a regime, where zero and two atoms can be equally well distinguished from one atom, i.e. $\text{SNR}_0 = \text{SNR}_2 =: \text{SNR}$. With $\Delta S \rightarrow 0$ eq. (3.8) then simplifies to

$$p_{\text{ia}} = \frac{\exp\left(-\frac{1}{2}\text{SNR}^2\right)}{1 + \exp\left(-\frac{1}{2}\text{SNR}^2\right)} \stackrel{\text{SNR}^2 \gg 1}{\approx} \exp\left(-\frac{1}{2}\text{SNR}^2\right). \quad (3.12)$$

The last approximation is justified, if the fidelity significantly exceeds the classical threshold of 50%, since this requires $p_{\text{ia}} \ll 1$. In section 3.3 it will be seen that for all relevant implementations of the QND measurement the square of the signal to noise ratio is proportional to the scattering probability:

$$\text{SNR}^2 = \alpha 2 p_{\text{scat}}. \quad (3.13)$$

The proportionality constant α depends only on parameters of the experimental apparatus and the measurement procedure and is in principal fixed for any experiment. Therefore, p_{scat} has to be adjusted to obtain the optimum fidelity. This can be done by varying the cavity-atom detuning Δ_{ca} or the number of photons accumulated during the measurement n_1 , since p_{scat} depends only on the ratio n_1/Δ_{ca}^2 . The quantity to be minimized is $1 - F$. Using eq. (3.5) in eq. (3.13) with $p_{\text{dec}} = p_{\text{scat}}$ one finds

$$1 - F = p_{\text{scat}} + \exp(-\alpha p_{\text{scat}}) (1 - p_{\text{scat}}). \quad (3.14)$$

Differentiating with respect to p_{scat} yields

$$\exp(\alpha p_{\text{scat}}) = 1 + \alpha (1 - p_{\text{scat}}). \quad (3.15)$$

For $p_{\text{scat}} \ll 1$, which should hold for fidelities significantly above 50%, eq. (3.15) is easily solved for p_{scat} , yielding:

$$p_{\text{scat}} = \frac{\ln(1 + \alpha)}{\alpha} \quad (3.16)$$

Inserting this result into eq. (3.14) one finds the following expression for the fidelity

$$F = \frac{\alpha - \ln(1 + \alpha)}{1 + \alpha} \stackrel{\alpha \gg 1}{\approx} 1 - \frac{\ln(1 + \alpha)}{\alpha}. \quad (3.17)$$

It can be seen by comparing eqs. (3.16) and (3.17) that for large α , i.e. high fidelities, the ultimate limit is set by the probability of spontaneous scattering. In order to estimate the entanglement fidelity for a given experimental setup, the parameter α has to be calculated. α depends on the signal to noise ratio of the QND measurement and thus on the specific implementation of this measurement. In the following section, two different detection techniques will be contrasted with respect to the achievable fidelity.

3.3 Experimental Implementation of the QND Measurement

As described in section 1.1, for $\Delta_{\text{ca}} \gg \Gamma$ an atom that couples to the resonator light field can be thought of as changing only the refractive index inside the resonator. For N atoms in $|F = 4\rangle$ in the resonator this change in the refractive index results in a shift of the cavity resonance frequency of $\Delta\omega_c = N g^2/\Delta_{\text{ca}}$. For a probe laser with a fixed frequency that is sent through the resonator, this lineshift results in a change of *intensity* and *phase* of the transmitted light. In all experiments described in chapter 2 the change in the intensity was used to gain information about the atom-light coupling. In the first part of this section I will argue that for our experiment the entanglement fidelity, which can be obtained with this method, is limited to the classical value of 50%. In the second part of this section I will describe how to measure the phaseshift of the transmitted light with a homodyne detector. Using this method a fidelity of 75% can be achieved under ideal conditions.

3.3.1 Transmission Level Detection

To obtain the best signal to noise ratio for detecting the lineshift $\Delta\omega_c$ via the transmission level, the *relative* change in the transmission per $\Delta\omega_c$ has to be maximized. Differentiating the cavity spectrum, one finds the *relative* transmission change to be given by

$$\left| \frac{1}{n_1} \frac{dn_1}{d\Delta\omega_c} \right| = \frac{2 \Delta_{\text{pc}}}{\kappa^2 + \Delta_{\text{pc}}^2}. \quad (3.18)$$

This quantity is maximized for $\Delta_{\text{pc}} = \kappa$. The transmission difference caused by the lineshift is then

$$\Delta n = n_1 \frac{g^2}{\kappa \Delta_{\text{ca}}}. \quad (3.19)$$

As mentioned in chapter 2, our transmission measurement is essentially shot noise limited, which yields a signal to noise ratio for the transmission level detection of

$$\text{SNR}_{\text{TL}} = \sqrt{n_1} \frac{g^2}{\kappa \Delta_{\text{ca}}}. \quad (3.20)$$

Using eqs. (3.7) and (3.20) in eq. (3.13) one finds that the fidelity for transmission level detection α_{TL} is given by

$$\alpha_{\text{TL}} = \frac{1}{2} \eta \frac{g^2}{\kappa \Gamma}. \quad (3.21)$$

Equation (3.18) and thus the calculated SNR is, of course, only valid for lineshifts much smaller than the cavity linewidth, i.e. $\Delta_{\text{ca}} \gg g^2/\kappa$. For larger lineshifts, i.e. smaller cavity-atom detunings, the curvature of the lorentzian cavity line shape will reduce the SNR relative to the value calculated from eq. (3.20). Thus, the value of α_{TL} in eq. (3.21) is overestimated

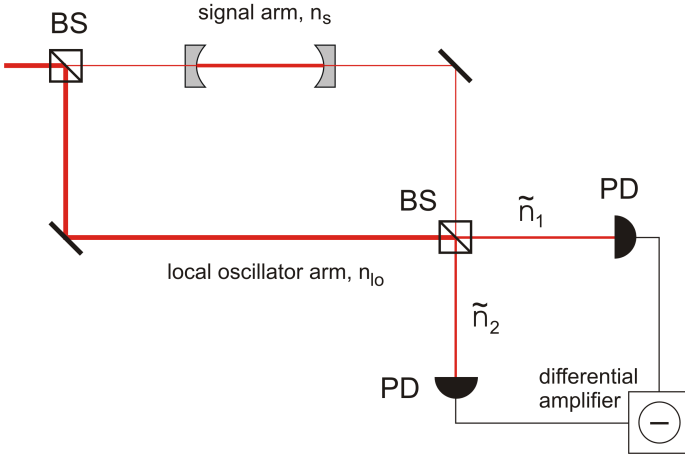


Figure 3.2: Sketch of a homodyne phase detector. The interaction between an atom and the resonator light field causes a change in the optical path difference between the two arms of a Mach-Zehnder interferometer. The path difference is translated into a difference in the powers on the two output ports. The light in the output ports is detected on regular photo diodes (PD). The difference of the photocurrents is proportional to the sine of the phaseshift in the signal arm caused by the atom-light interaction.

for detunings $\Delta_{ca} \lesssim g^2/\kappa$.

As discussed in section 1.2 the maximum achievable coupling strength in our experiment is $g_{\max} = 2\pi \times 12.8$ MHz, while the typically obtained effective coupling strength is $g_{\text{eff}} = 2\pi \times 9$ MHz. $\kappa = 2\pi \times 0.4$ MHz and $\Gamma = 2\pi \times 5.2$ MHz. The detection efficiency is $\eta = 4\%$. These values result in

$$\left. \begin{array}{l} \alpha_{\text{TL}} = 1.6 \\ F_{\text{TL}} = 24\% \end{array} \right\} g = 12.8 \text{ MHz}$$

$$\left. \begin{array}{l} \alpha_{\text{TL}} = 0.8 \\ F_{\text{TL}} = 11\% \end{array} \right\} g = 9 \text{ MHz}. \quad (3.22)$$

For these small α parameters the approximations made in eqs. (3.7), (3.12) and (3.16) do not hold. A full calculation according to the correct formulas from eqs. (3.7) and (3.8) yields a maximum fidelity for our experimental parameters of 50%, which is achieved for $n_1/\Delta_{ca}^2 \rightarrow 0$. This is the same as just *guessing* the number of coupled atoms. In order to achieve a fidelity of 60%, slightly above the classical threshold, the photon detection efficiency would have to be improved by a factor of 4, which is impossible with the current resonator.

However, the lineshift caused by the atom-light interaction cannot only be measured via the transmission level, but also via the phase of the transmitted light field. If the probe laser is on resonance with the empty cavity, the lineshift for a single atom coupled to the resonator translates into a phaseshift of the transmitted light. This phaseshift can be measured with a homodyne detector as suggested in [3].

3.3.2 Homodyne Phase Detection

Figure 3.2 shows a sketch of a homodyne detection setup. The resonator is situated in one arm of a Mach-Zehnder interferometer. The powers in the two output ports of the interferometer P_1 and P_2 are detected on photo diodes. These powers are proportional to the numbers of photons \tilde{n}_1 and \tilde{n}_2 detected in each port during the measurement duration t_m . The difference of the

detector photocurrents then yields a signal proportional to the sine of the phase difference of the two arms. In the signal arm, containing the resonator, the power is on the single photon level, assuring that the atom-resonator system is in the weak excitation regime. In the so-called local oscillator arm the power is much higher, limited only by the saturation power of the photo diodes. The high local oscillator intensity is the main advantage of homodyne detection and helps to suppress technical noise [45]. This will become clear in the following analysis of the signal to noise ratio.

The input-output relations of the beam splitter yield the photon numbers on the two output ports

$$\tilde{n}_1 = \frac{1}{2} (n_{lo} + n_s + 2\sqrt{n_{lo}n_s} \sin(\Delta\varphi)) \quad (3.23)$$

$$\tilde{n}_2 = \frac{1}{2} (n_{lo} + n_s - 2\sqrt{n_{lo}n_s} \sin(\Delta\varphi)). \quad (3.24)$$

This results in a homodyne signal of

$$n_{\text{hom}} = \tilde{n}_1 - \tilde{n}_2 = 2\sqrt{n_{lo}n_s} \sin(\Delta\varphi) \approx 2\sqrt{n_{lo}n_s} \Delta\varphi. \quad (3.25)$$

Here, n_{lo} and n_s are the photon numbers in the local oscillator arm and the signal arm, respectively. The noise of the homodyne signal has three contributions: The signal shot noise, the local oscillator shot noise and additional technical noise such as photo diode dark currents

$$\delta n_{\text{hom}}^2 = \delta \tilde{n}_1^2 + \delta \tilde{n}_2^2 + \delta n_{\text{tech}}^2 = n_s + n_{lo} + \delta n_{\text{tech}}^2. \quad (3.26)$$

Since the signal scales with the local oscillator noise $\delta n_{lo} = \sqrt{n_{lo}}$, the best signal to noise ratio is obtained, if $n_{lo} \gg n_s, \delta n_{\text{tech}}^2$. As explained in section 1.1 the phase shift of the light transmitted through the resonator per coupled atom is $\Delta\varphi = g^2/\kappa\Delta_{ca}$. Thus, in the limit of a large local oscillator intensity and with $n_s = n_1$ the signal to noise ratio reads

$$\text{SNR}_{\text{hom}} = \frac{2\sqrt{n_{lo}n_s}\Delta\varphi}{\sqrt{n_s + n_{lo} + \delta n_{\text{tech}}^2}} \approx 2\sqrt{n_1} \frac{g^2}{\kappa\Delta_{ca}}. \quad (3.27)$$

This SNR yields the following value for α_{hom} :

$$\alpha_{\text{hom}} = 2\eta \frac{g^2}{\kappa\Gamma} \quad (3.28)$$

For our experimental parameters $(g_{\text{max}}, g_{\text{eff}}, \kappa, \Gamma) = 2\pi (12.8, 9, 0.4, 5.2)$ MHz and $\eta = 4\%$ this results in the following values for α_{hom} and F_{hom} :

$$\left. \begin{array}{l} \alpha_{\text{hom}} = 6.3 \\ F_{\text{hom}} = 59\% \end{array} \right\} g = 12.8 \text{ MHz}$$

$$\left. \begin{array}{l} \alpha_{\text{hom}} = 3.1 \\ F_{\text{hom}} = 42\% \end{array} \right\} g = 9 \text{ MHz} \quad (3.29)$$

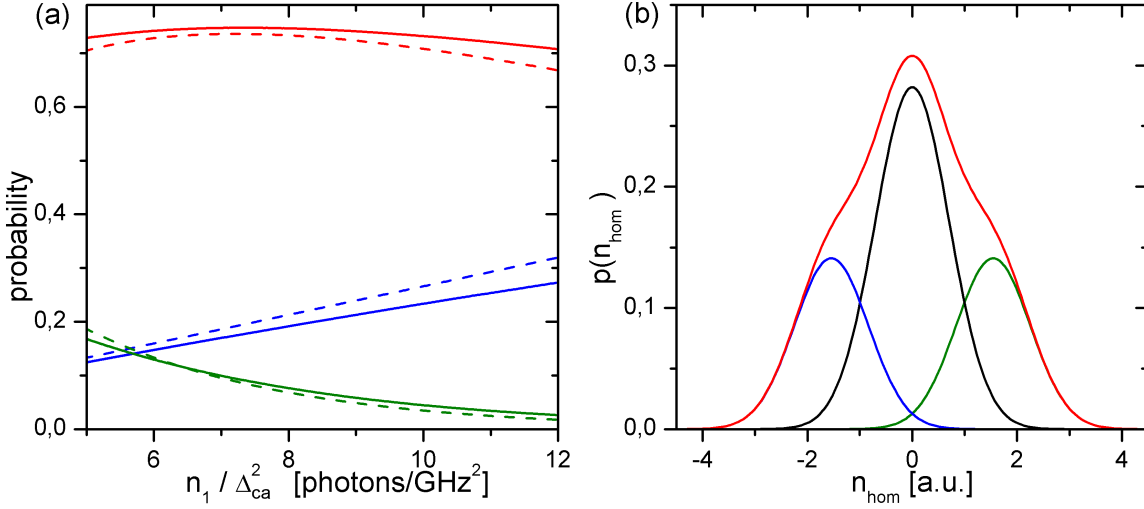


Figure 3.3: (a): F (red), p_{scat} (blue), and p_{ia} (green) plotted as a function of the dimensionless parameter n_1/Δ_{ca}^2 obtained from exact (solid) and approximate (dashed) calculations. (b): Probability distribution of the homodyne signal at maximum fidelity (red). The contributions of the signal distributions for zero coupled atoms (green), one coupled atom (black), and two coupled atoms (blue) are weighted according to the structure of the initial product state of the two atoms.

Remarkably, homodyne detection yields a two times higher signal to noise ratio than transmission level detection on the slope of the resonator line, and thus a four times higher α . The origin of this factor of two is explained in Appendix C. Consequently, homodyne detection yields the same result as transmission level detection for a four times higher detection efficiency. In terms of detection efficiency there is yet another advantage in using a homodyne detector. Since the local oscillator beam can be chosen arbitrarily intense without loss in sensitivity, regular photo diodes can be used as detectors instead of SPCMs. Regular photo diodes achieve quantum efficiencies close to 100%, while the best SPCMs reach only 50%. Consequently, in our setup the detection efficiency could be increased from 4% to 8% with a homodyne detector. In this case the expected values for α_{hom} and F_{hom} are:

$$\left. \begin{array}{l} \alpha_{\text{hom}} = 12.6 \\ F_{\text{hom}} = 74\% \end{array} \right\} g = 12.8 \text{ MHz}$$

$$\left. \begin{array}{l} \alpha_{\text{hom}} = 6.2 \\ F_{\text{hom}} = 59\% \end{array} \right\} g = 9 \text{ MHz} \quad (3.30)$$

The values for the fidelity calculated according to eq. (3.17) are maximum values obtained for the optimum ratio of n_1/Δ_{ca}^2 . To illustrate the dependence on this parameter, fig. 3.3(a) depicts the fidelity as well as p_{scat} and p_{ia} as a function of n_1/Δ_{ca}^2 . The dashed lines are obtained from the approximated formula in eq. (3.14) using the scaling parameter α_{hom} from eq. (3.28). The solid lines are exact calculations, where the exponential form of the scattering probability (see eq. (3.7)) is taken into account and p_{ia} is calculated numerically from the

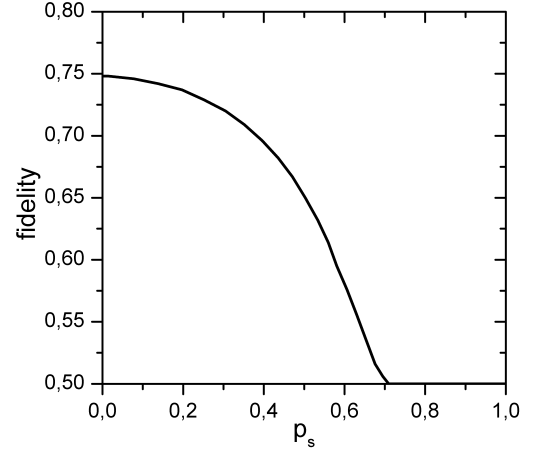


Figure 3.4: Entanglement fidelity as a function of success probability. To obtain this curve, the fidelity is calculated without approximations for a range of n_1/Δ_{ca}^2 and maximized subsequently. This is done for different acceptance intervals ΔS .

overlap of the signal distributions. Obviously, the approximated fidelity of 74% is slightly underestimated. The maximum fidelity obtained from the exact calculation is 75%. This is, because the linear approximation in eq. (3.7) overestimates p_{scat} . The maximum fidelity is obtained for about 8 photons/GHz². n_1 and Δ_{ca} can, however, not be chosen completely at will. The derivation of the fidelity given here is based on the assumption that the atom-light coupling only causes a phase shift of the transmitted light without changing the transmitted intensity. For this to be a good approximation, the resonator *lineshift* has to be much smaller than the resonator *linewidth* ($g^2/\Delta_{ca} \ll \kappa$). This requires a cavity-atom detuning in the GHz range and thus a photon number $n_1 \gtrsim 8$.

The probability distribution of the homodyne signal obtained in this situation is depicted in fig. 3.3(b). Obviously, the three gaussians have a significant overlap. At the peak position, however, the contributions of the signal distributions belonging to $N = 0, 2$ are very small. Thus, a high fidelity can be obtained, if the acceptance interval Δn_{hom} and thus the success probability p_s is chosen sufficiently small. The approximate fidelity calculations presented above assume an infinitely small p_s . The exact calculations plotted in fig. 3.3(a) assume $p_s = 1.5\%$. Figure 3.4 depicts the fidelity as a function of the success probability. The fidelity depends only weakly on p_s , if p_s is small. For a success probability of 35% the fidelity is still 70%.

The signal to noise analysis in this section clearly states that for shot noise limited detectors, homodyne detection yields a significantly better fidelity than transmission level detection. For our experimental parameters, this difference in the detection methods is even decisive for obtaining a fidelity above the classical threshold of 50%. When implementing such a QND measurement experimentally, there are, however, additional technical imperfections that will further reduce the expected fidelities. The two most important technical challenges shall be addressed in the following section.

3.4 Influence of Technical Noise and Variation of g

The homodyne detector described in the previous section is supposed to measure a change in the optical path difference in a Mach-Zehnder interferometer due to the refractive index change caused by the coupling of an atom to the resonator light field. An interferometer, however, does not distinguish between changes of the refractive index and changes in the *geometrical* path difference. Thus, the geometrical path difference in the interferometer has to be stabilized to a fraction of $\lambda\Delta\varphi/2\pi$, where $\Delta\varphi$ is the atom-induced phaseshift that is to be measured. This is a challenging but possible task. In the group of E. Polzik in Kopenhagen a shot noise limited Mach-Zehnder interferometer for homodyne phase detection has been built [46].

A second challenge is connected to the measurement of the entanglement fidelity. The fidelity is defined as the expectation value of the density matrix $\hat{\rho}$ of the generated ensemble calculated for the entangled state (see eq. (3.2)). The full density matrix can only be reconstructed from many different measurements, each on a different pair of atoms. If all atom pairs are in the target state

$$|\psi_t\rangle = \frac{1}{\sqrt{2}} (|0\rangle_1 \otimes |1\rangle_2 + |1\rangle_1 \otimes |0\rangle_2) \quad (3.31)$$

the density matrix in the basis $\{|0\rangle_1 \otimes |1\rangle_2, |1\rangle_1 \otimes |0\rangle_2\}$ reads

$$\hat{\rho} = |\Psi_t\rangle \langle \Psi_t| = \begin{pmatrix} \frac{1}{2} & \frac{1}{2} \\ \frac{1}{2} & \frac{1}{2} \end{pmatrix}. \quad (3.32)$$

yielding a fidelity of $F = 1$ (see eq. (3.2)). A varying phase between the two contributions of the entangled state will, however, lead to a reduction of the off-diagonal elements of the density matrix. This will reduce the fidelity. Such a varying phase occurs, if there is a difference in the atom-light coupling strengths g_1 and g_2 of the two atoms that varies from shot to shot. A difference in the coupling strengths introduces an energy difference between the states $|0\rangle_1 \otimes |1\rangle_2$ and $|1\rangle_1 \otimes |0\rangle_2$. According to [47], the phase difference that is accumulated during the measurement time due to this energy difference is given by

$$\varphi = t_m \frac{g_1^2 - g_2^2}{\delta}. \quad (3.33)$$

For an ensemble of atom pairs that all have the same phaseshift, the density matrix reads:

$$\rho(\varphi) = \begin{pmatrix} \frac{1}{2} & \frac{1}{2} \exp(i\varphi) \\ \frac{1}{2} \exp(i\varphi) & \frac{1}{2} \end{pmatrix} \quad (3.34)$$

Averaging over many different phaseshifts will reduce the off-diagonal elements and thus the fidelity. If the phaseshift varies over an interval of 2π or more, the off-diagonal elements of

the density matrix vanish, yielding the classical fidelity of 50%. From eq. (3.33) one finds that for a measurement time of 1 ms, an average coupling of 9 MHz and a detuning of 2 GHz, this happens for a variation of coupling strengths of more than 8%. The transmission level measurements presented in section 2.1.1 indicate variations of the single atom coupling strength of about 10% in our experiment. Thus, currently the fidelity achievable with our system is limited by the control over the coupling strength. Even with the implementation of homodyne detection a fidelity above 50% cannot be achieved. There might, however, be ways to further improve the control over the coupling strength. Two possible improvements will be discussed in the outlook of this thesis.

Outlook - Control, Control, Control

In this thesis I have presented quantum jumps of one and two atoms measured via the dispersive lineshift caused by the strong coupling of the atoms to the light field of an optical resonator. I have shown that our setup would in principle allow the probabilistic generation of entangled states via a QND measurement. The quantity that determines the fidelity of this entanglement scheme is

$$\eta \frac{g_{\text{eff}}^2}{\kappa \Gamma}.$$

Since κ and Γ are fixed in our experiment, future work should concentrate on improving the photon detection efficiency η and the effective coupling strength g_{eff} . The detection setup presented here has already been carefully optimized. However, as stated in chapter 3 replacing the SPCM by a homodyne detector could increase the detection efficiency by a factor of two, since regular photodiodes with a quantum efficiency close to 1 could be used. For our setup with a rather low overall detection efficiency due to the resonator absorption, this factor of two will be decisive for achieving an entanglement fidelity above the classical threshold. Therefore, in my view it is worth while to think about the implementation of homodyne detection in our setup.

A better control over the atomic position in the resonator and thus the effective coupling strength is the second important challenge in our experiment: The lineshift measurements from chapter 2 indicate that the achieved coupling strength is significantly below the maximum coupling strength expected at an anti-node of the cavity mode. This is most probably due to insufficient localization of the atoms.

In the current setup the atomic localization is not limited by the *size* of the trapping potential. Along the cavity axis, where the coupling strength varies most strongly and the localization is most critical, the lock laser dipole potential is in principle small enough to confine the atom to the places of strong coupling. The measurements presented in this thesis indicate that the localization is rather limited by the temperature of the atoms. However, pre-cooling the atoms to the vibrational groundstate of the optical lattice before they are inserted into the resonator will probably not help. The atoms are parametrically heated in the cavity due to fluctuations of the lock laser potential. We assume that the process which is predominantly responsible for the fluctuations of the coupling strength is hopping of the atoms between different lock laser potential wells [18]. Due to the varying phase between lock and probe laser standing wave along the cavity axis the effective coupling strength varies for different lock laser potential wells. Thus, the smaller the hopping range, the smaller the possible variation of g_{eff} . An additional trap realized by a rather tightly focused laser superimposed on the optical lattice beams could potentially limit the hopping range to a smaller region. Such an additional trap

could be realized with a blue detuned, doughnut shaped laser beam, which traps the atoms at the intensity minimum at the center of the beam. The laser could then be tuned rather close to the atomic transition without leading to a high photon scattering rate. In this way a deep trap can be realized with moderate laser power.

With a better control over the atomic position it might be possible to gain further insight into the cavity cooling mechanisms that are active in our resonator. Especially the local structure of the friction force associated with the cooling is of interest. Understanding this local structure one might find a regime where regions of large friction fall together with regions of strong coupling and a more stable coupling strength might be achieved.

Ways to systematically investigate the motional dynamics of a single atom in the cavity are currently evaluated in our group. The first step is to look at the photons transmitted through the cavity with a much higher time resolution so that the arrival times of the individual photons can be recorded. This should allow the observation of the oscillatory motion of the atoms in the trapping potential.

These are small steps on the way towards the realization of the controlled, coherent interaction of a single and two atoms with a single mode of the electromagnetic field. A system, which is the simplest possible from a theoretical point of view and has triggered a great number of exciting theoretical proposals, but which is still a great challenge when it comes to the implementation in the laboratory.

Appendix A

Calculation of the Quantum Jump Time

The dependence of the jump time τ_{43} on the cavity-atom detuning as plotted in fig. 2.4 is calculated using the Kramers-Heisenberg formula [26]. This is a generalization of Fermi's golden rule, which includes second order processes. Applied to the $|F = 4\rangle \rightarrow |F = 3\rangle$ transfer it reads

$$\frac{1}{\tau_{43}} = \frac{\Gamma}{2} \frac{3\pi c^2}{\hbar \omega_{D2}^3} I \frac{1}{|d_{45+}|^4} \sum_r \left| \sum_{l,q} \frac{\langle 3; r | \hat{d}_q | l \rangle \langle l | \mathbf{e}_L \cdot \hat{\mathbf{d}} | 4; +4 \rangle}{\Delta_l} \right|^2. \quad (\text{A.1})$$

Here, the atomic hyperfine states are written in the form $|F; m_F\rangle$. It has been assumed that the atom is initially in the outermost Zeeman sublevel of the groundstate $|F = 4\rangle$ manifold. ω_{D2} is the frequency of the caesium D_2 -transition and I denotes the intra cavity probe laser intensity. $|d_{45+}|$ is the transition dipole moment of the $|F = 4; +4\rangle \rightarrow |F' = 5; +5\rangle$, which is the strongest hyperfine component of the D_2 -line. $\hat{\mathbf{d}}$ is the dipole operator and \hat{d}_q are its spherical components. The index q takes the values $-1, 0,$ and $+1$ for $\sigma^-, \pi,$ and σ^+ transitions, respectively. \mathbf{e}_L is the polarization vector of the probe laser \mathbf{E} -field. The product of matrix element $\langle 3; r | \hat{d}_q | l \rangle \langle l | \mathbf{e}_L \cdot \hat{\mathbf{d}} | 4; +4 \rangle$ describes a two photon process transferring the atom from $|4; +4\rangle$ to $|3; r\rangle$ via the intermediate level $|l\rangle$, where one photon is absorbed from probe laser described by the operator $\mathbf{e}_L \cdot \hat{\mathbf{d}}$ and a second photon is emitted described by \hat{d}_q .

In the experiments presented in this thesis the quantization axis is defined by a magnetic field along the cavity axis perpendicular to the probe laser polarization. Thus,

$$\mathbf{e}_L \cdot \hat{\mathbf{d}} = \frac{1}{\sqrt{2}} (\hat{d}_{-1} + \hat{d}_{+1}). \quad (\text{A.2})$$

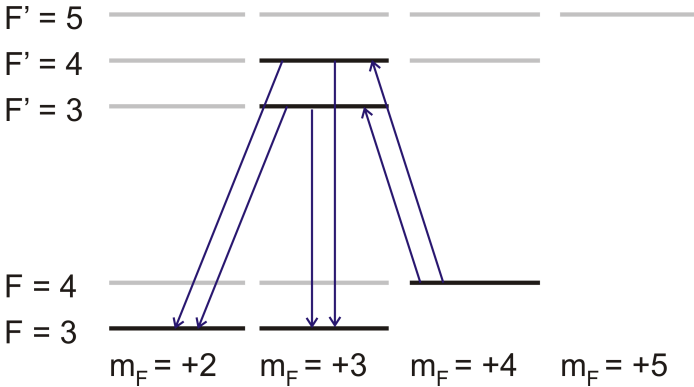


Figure A.1: Dipole-allowed scattering paths for state changing inelastic Raman transitions. Initially the atom is assumed to be in the outermost Zeeman sublevel $|4; +4\rangle$.

This means that the probe laser can only induce σ^+ - and σ^- -transitions. For the atom being initially in the $|4; +4\rangle$ state only a σ^- -transition can result in a change of the hyperfine groundstate. A σ^- -transition excites the atom to the $|5'; +5\rangle$ state from where the atom can only decay to $|4; +4\rangle$. The scattering paths with nonzero transition amplitudes, i.e. those paths that involve only dipole allowed transitions, are indicated by arrows in fig. A.1.

The amplitudes of the paths ending at different Zeeman substates have to be summed up incoherently, i.e. after taking their absolute value squared, because they can in principle be distinguished by measuring the polarization of the emitted photons. The paths ending at the same Zeeman sublevel but go via the two different hyperfine excited states have to be summed up coherently, i.e. before they are squared, because there is no way to distinguish between them.

The values for ω_{D2} , Γ , $|d_{45+}|$ and the matrix elements are taken from reference [48]. The intra cavity probe laser intensity I is calculated by numerically solving the master equation of the atom-cavity system.

Of all Zeeman substates, the outermost states yield the longest jump time. Starting from these states, only the “inward” transitions $|F = 4; m_F = \pm 4\rangle \rightarrow |F' = 3, 4; m_F = \pm 3\rangle$ are allowed and can cause jumps from $|F = 4\rangle$ to $|F = 3\rangle$ (see fig. A.1). If the atom is in one of the inner Zeeman states $|F = 4; |m_F| < 4\rangle$, also the “outward” transitions, e.g. $|F = 4; m_F = \pm 3\rangle \rightarrow |F' = 4; m_F = \pm 4\rangle$ are allowed. This shortens the jump time, since the intra cavity intensity is more or less constant for the different $|F = 4\rangle$ $|m_F|$ -levels. This is due to the fact that the coupling strength is mainly determined by the $|F = 4\rangle \rightarrow |F' = 5\rangle$ transition, for which the maximum coupling strength changes by less than 1% over the different $|m_F|$ -levels.

Appendix B

Two-Atom Intensity Auto-Correlation Function

Calculation of the Theoretically Expected $g^{(2)}(\tau)$ from the Rate Eqs.

The intensity auto-correlation function of the two-atom random telegraph signals can be derived from the rate eqs. (2.26)–(2.28) governing the internal state dynamics of the atoms. The derivation given here for the two-atom telegraph signals is done according to the derivation for the single-atom case given in [27].

The intensity auto-correlation is defined as

$$g^{(2)}(\tau) = \frac{\langle I(t)I(t+\tau) \rangle}{\langle I(t) \rangle^2}. \quad (\text{B.1})$$

For a digitized two-atom random telegraph signal that takes the values 2, 1, and 0 for 0, 1, and 2 atoms in $|F = 4\rangle$ the product $I(t)I(t+\tau)$ in eq. (B.1) can only take the values 0, 1, 2, and 4. It takes the value 1, if at times t and $t+\tau$ one atom is in $|F = 4\rangle$. It takes the value 2, if at time t one atom is in $|F = 4\rangle$ and at $t+\tau$ no atom is in $|F = 4\rangle$. And it takes the value 4, if at times t and $t+\tau$ there are no atoms in $|F = 4\rangle$. Let $p_{N,M}(\tau)$ be the probability to find N atoms in $|F = 4\rangle$ at time t and M atoms at time $t+\tau$. Let further be $p_{N,ss}$ the probability to find N atoms in $|F = 4\rangle$ at any time in the steady state. With these probabilities the intensity auto-correlation function can be written as

$$g^{(2)}(\tau) = \frac{p_{1,1}(\tau) + 2p_{1,0}(\tau) + 2p_{0,1}(\tau) + 4p_{0,0}(\tau)}{(p_{1,ss} + 2p_{0,ss})^2}. \quad (\text{B.2})$$

The probability $p_{N,M}(\tau)$ to find N atoms in $|F = 4\rangle$ at time t and M atoms at time $t+\tau$ is the same as the probability $p_{N,ss}$ to find N atoms in $|F = 4\rangle$ at any time in the steady state multiplied with the conditional probability $p_M(\tau; N)$ to find M atoms in $|F = 4\rangle$ at time τ , if N atoms were in $|F = 4\rangle$ at time t .

$$p_{N,M}(\tau) = p_{N,ss} p_M(\tau; N) \quad (\text{B.3})$$

The conditional probability $p_M(\tau; N)$ is now directly obtained from the rate eqs. (2.26)–(2.28), which I will rewrite here for convenience:

$$\frac{dp_0}{d\tau} = R_{10}p_1(\tau) - 2R_{\text{rep}}p_0(\tau) \quad (\text{B.4})$$

$$\frac{dp_1}{d\tau} = 2R_{\text{rep}}p_0(\tau) + R_{21}p_2(\tau) - (R_{10} + R_{\text{rep}})p_1(\tau) \quad (\text{B.5})$$

$$\frac{dp_2}{d\tau} = R_{\text{rep}}p_1(\tau) - R_{21}p_2(\tau) \quad (\text{B.6})$$

The condition that N atoms are in $|F = 4\rangle$ at time t is accounted for by the initial condition $p_{M \neq N}(0) = 0$. The solutions of eqs. (B.4)–(B.6) is easily obtained using a software such as MAPLE™.

Calculation of $g^{(2)}(\tau)$ from the Experimental Data

In principle, $g^{(2)}(\tau)$ can be easily obtained by the direct evaluation of eq. (B.1). A slight complication occurs for the random telegraph signals presented in chapter 2, because due to the limited life time of the atoms in the resonator they have not been recorded as one long telegraph signal, but as many short traces of 400 ms each. This brings up the question how to calculate an average correlation function for all the measured traces. There are three possible ways to do the averaging:

1. One can calculate $g^{(2)}(\tau)$ for each individual trace and then average over all traces. Let curly braces denote the average over all traces. Then $g^{(2)}(\tau)$ according to this averaging method is

$$g^{(2)}(\tau) = \left\{ \frac{\langle I(t)I(t+\tau) \rangle}{\langle I(t) \rangle^2} \right\}. \quad (\text{B.7})$$

2. One can average numerator and denominator independently over all traces, yielding

$$g^{(2)}(\tau) = \frac{\{ \langle I(t)I(t+\tau) \rangle \}}{\{ \langle I(t) \rangle^2 \}}. \quad (\text{B.8})$$

3. In the denominator, one can average $\langle I(t) \rangle$ first over all traces and then square it:

$$g^{(2)}(\tau) = \frac{\{ \langle I(t)I(t+\tau) \rangle \}}{\{ \langle I(t) \rangle \}^2} \quad (\text{B.9})$$

To understand the differences between these three averaging methods, I have applied them to a set of 150 ideal two-atom random telegraph signals of 400 ms duration, simulated according to the rate eqs. (2.26)–(2.28). The average auto-correlation functions calculated according

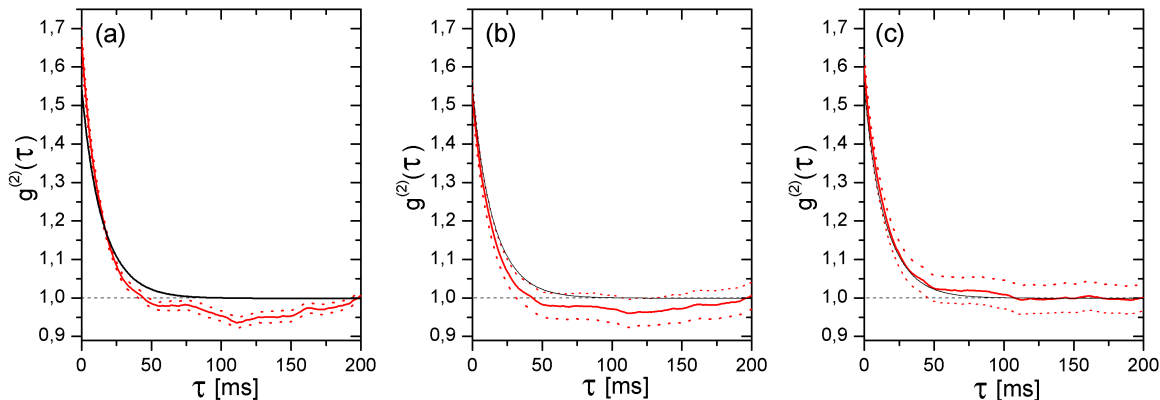


Figure B.1: Average intensity auto-correlation function of 150 400 ms long ideal two-atom telegraph signals (red solid lines), calculated according to eq. (B.7) (a), eq. (B.8) (b), and eq. (B.9) (c). The dotted lines indicate the statistical error due to the finite size of the sample. The black solid lines show the intensity auto-correlation function calculated from the rate equations, assuming one single, long telegraph signal. The telegraph signals have been simulated according to the rate eqs. (2.26)–(2.28). The rates used are those extracted from two-atom telegraph signals measured at $\Delta_{ca} = 2\pi \times 38$ MHz, which are given in eq. (2.36).

to eqs. (B.7)–(B.9) are shown in fig. B.1 together with the $g^{(2)}(\tau)$ calculated from the rate equations as described above. The calculation via the rate equations does not assume any averaging over traces. Obviously, the auto-correlation function calculated according to eq. (B.9) agrees best with the rate equation model. I attribute this to the fact that in this method the normalization factor $\{\langle I(t) \rangle\}^2$ is the same as would be obtained for a single long telegraph signal. Statistical variations of the average intensity between the traces do not influence the normalization. In contrast, the normalization factor $\{\langle I(t)^2 \rangle\}$ in eq. (B.8), where the single trace intensity averages are first squared and then averaged over all traces, is systematically higher than that obtained for a single long telegraph signal. This is because the square of the average of a set of numbers is always smaller than the average of the squares of the same set of numbers. Equation (B.7), where even the division by the normalization factor is done before averaging over all traces, is even more sensitive to statistical fluctuations as can be seen in fig. B.1(a). The details of the deviation from the correlation function expected for a single long telegraph signal are not discussed here. Since the averaging according to eq. (B.9) yields the best agreement with the correlation function calculated from the rate equations for a single long telegraph signal, I have used this averaging method for the evaluation of the measured data.

While being insensitive to statistical fluctuations of the single trace intensity averages, eq. (B.9) is sensitive to systematic variations of the single trace average intensities caused by variations of the jump rates. This can be understood as follows: For a simple two-level telegraph signal, the intensity auto-correlation function as calculated from eq. (B.8) is the probability of finding the signal in the “on” state at time $t + \tau$, if at time t it was also “on”, relative to the probability to find the signal “on” at any two times picked randomly from any

two traces. If in some traces the signal is significantly more often “on” than in most traces, the probability to find the signal “on” for two randomly picked times in this trace is higher than the probability to find the signal “on” for two times picked from any two traces. This systematically increases the auto-correlation function for large τ . Similarly, this holds for three-level telegraph signals as obtained from the two-atom quantum jumps.

Appendix C

Homodyne versus Transmission Level Detection

The signal to noise analysis in chapter 3 shows a significant difference in sensitivity between homodyne and transmission level detection when a shift of the cavity resonance frequency is to be measured. This difference will be explained here. The signal to noise ratios of the two methods were found to differ by a factor of two:

$$\text{SNR}_{\text{TL}} = \sqrt{n_1} \frac{g^2}{\kappa \Delta_{\text{ca}}} , \text{SNR}_{\text{hom}} = 2\sqrt{n_1} \frac{g^2}{\kappa \Delta_{\text{ca}}} \quad (\text{C.1})$$

Here n_1 is the number of photons transmitted through the resonator containing one coupled atom during the measurement time. It is proportional to the intra cavity photon number.

There are two advantages of homodyne detection that are responsible for the factor of two difference. One is technical, the other is rather fundamental. To understand the technical advantage, consider an ideal resonator that has no absorption and diffraction losses so that $R + T = 1$. As shown in chapter 3, the optimum sensitivity for transmission level detection is achieved for a laser-cavity detuning $\Delta_{\text{pc}} = \kappa$. For this detuning and an ideal resonator half of the light incident on the resonator is reflected. If an atom couples to the cavity and shifts the cavity resonance, this reflected light varies by the same amount as the transmitted light. Thus, if the transmitted *and* reflected light were detected, the signal would be two times higher than for the detection of only the transmission assumed in chapter 3. However, the shot noise would also increase by a factor of two, since the total amount of photons doubles. Thus, for an ideal resonator, if both reflected and transmitted light were detected, the signal to noise ratio of transmission level detection would improve by a factor of $\sqrt{2}$ compared to that given in eq. (C.1). Now for a resonator with significant absorption, even on resonance and for perfect mode matching, most of the incident light is reflected from the resonator. In a possible photon counting measurement of the reflected light, the shot noise of the light reflected due to imperfect mirrors would be much higher than the expected signal. This makes a measurement of the reflected light useless.

The remaining factor of $\sqrt{2}$ difference between SNR_{TL} and SNR_{hom} has a more fundamental reason that lies in the use of a high intensity local oscillator beam in homodyne detection. The full signal to noise ratio for homodyne detection reads according to eq. (3.27)

$$\text{SNR}_{\text{hom}} = \frac{2\sqrt{n_{\text{lo}}n_{\text{s}}}\Delta\varphi}{\sqrt{n_{\text{s}} + n_{\text{lo}}}} \quad (\text{C.2})$$

The technical noise contribution has been left out for the sake of the argument. If the local oscillator is much more intense than the signal, the signal shot noise can be neglected compared to that of the local oscillator. However, if $n_s \approx n_{lo}$, the shot noise of the signal has to be taken into account and the signal to noise ratio decreases by a factor of $\sqrt{2}$ compared to the case of a strong local oscillator. In this case the homodyne signal to noise ratio is the *same* as obtained for transmission level detection with an absorption free resonator. Thus, in the case where the local oscillator has the same intensity as the signal field there is no difference between the signal to noise ratios of homodyne and transmission level detection.

In both detection methods an interferometer is used to compare the phase of the field emitted from the resonator to the phase of a reference field. In transmission level detection this is done with the resonator itself acting as a Fabry-Perot interferometer. In homodyne detection an external Mach-Zehnder interferometer is used. The fundamental difference between the two methods is that a Mach-Zehnder interferometer has two completely independent interferometer arms and compares the fields in these two arms with each other. The light field in the local oscillator arm acts as a reference for the field in the signal arm. Since the arms are independent it is possible to increase the intensity in the local oscillator arm. This makes the reference more stable and thus increases the measurement accuracy. In a Fabry-Perot interferometer the signal light is reflected back and forth between the two mirrors and in fact interferes only with itself. Consequently, there is no way to increase the stability of the reference, since the same beam acts as both signal and reference.

Bibliography

- [1] P. J. Windpassinger, D. Oblak, P. G. Petrov, M. Kubasik, M. Saffman, C. L. Garrido Alzar, J. Appel, J. H. Muller, N. Kjaergaard, and E. S. Polzik, *Nondestructive Probing of Rabi Oscillations on the Cesium Clock Transition near the Standard Quantum Limit*, Physical Review Letters **100**, 103601–4 (2008)
- [2] A. D. Boozer, A. Boca, R. Miller, T. E. Northup, and H. J. Kimble, *Cooling to the Ground State of Axial Motion for One Atom Strongly Coupled to an Optical Cavity*, Physical Review Letters **97**, 083602–4 (2006)
- [3] Anders S. Sørensen and Klaus Mølmer, *Measurement Induced Entanglement and Quantum Computation with Atoms in Optical Cavities*, Physical Review Letters **91**, 097905 (2003)
- [4] D. F. Walls and G. J. Milburn, *Quantum Optics*, Springer Verlag, 2nd edition (2008)
- [5] E.T. Jaynes and F.W. Cummings, *Comparison of quantum and semiclassical radiation theories with application to the beam maser*, Proceedings of the IEEE **51**, 89–109 (1963)
- [6] Bruce W. Shore and Peter L. Knight, *The Jaynes-Cummings Model*, Journal of Modern Optics **40**, 1195 (1993)
- [7] Howard Carmichael, *An Open Systems Approach to Quantum Optics*, Lecture Notes in Physics, Springer-Verlag (1993)
- [8] Anders S. Sørensen and Klaus Mølmer, *Probabilistic Generation of Entanglement in Optical Cavities*, Physical Review Letters **90**, 127903 (2003)
- [9] Stefan Kuhr, *A controlled quantum system of individual neutral atoms*, Ph.D. thesis, Universität Bonn (2004), URL http://hss.ulb.uni-bonn.de/diss_online/
- [10] Wolfgang Alt, *Optical control of single neutral atoms*, Ph.D. thesis, Universität Bonn (2004), URL http://hss.ulb.uni-bonn.de/diss_online/
- [11] Dominik Schrader, *A Neutral Atom Quantum Register*, Ph.D. thesis, Universität Bonn (2004), URL http://hss.ulb.uni-bonn.de/diss_online/
- [12] Igor Dotsenko, *Single atoms on demand for cavity QED experiments*, Ph.D. thesis, Universität Bonn (2007), URL http://hss.ulb.uni-bonn.de/diss_online/

- [13] Wolfgang Alt, *An objective lens for efficient fluorescence detection of single atoms*, *Optik* **113**, 142–144 (2002)
- [14] R. W. P. Drever, J. L. Hall, F. V. Kowalski, J. Hough, G. M. Ford, A. J. Munley, and H. Ward, *Laser phase and frequency stabilization using an optical resonator*, *Applied Physics B: Lasers and Optics* **31**, 97–105 (1983)
- [15] Karim Lenhard, *Stabilisierung eines Resonators hoher Finesse zur Atom-Lichtfeld-Kopplung*, Diplomarbeit, Universität Bonn (2008)
- [16] George A. Rakuljic and Victor Leyva, *Volume holographic narrow-band optical filter*, *Optics Letters* **18**, 459–461 (1993), URL <http://ol.osa.org/abstract.cfm?URI=ol-18-6-459>
- [17] Mika Khudaverdyan, *Quantum Jumps and VRS*, Ph.D. thesis, Universität Bonn (2009), URL http://hss.ulb.uni-bonn.de/diss_online/
- [18] Ariane Stiebeiner, *Deterministische Kopplung eines einzelnen Atoms an die Mode eines Resonators hoher Finesse*, Diplomarbeit, Universität Bonn (2008)
- [19] Peter Domokos and Helmut Ritsch, *Mechanical effects of light in optical resonators*, *Journal of the Optical Society of America B* **20**, 1098–1130 (2003)
- [20] H. J. Kimble, *Strong interactions of single atoms and photons in cavity QED*, *Physica Scripta* **T76**, 127–137 (1998)
- [21] D. Schrader, I. Dotsenko, M. Khudaverdyan, Y. Miroshnychenko, A. Rauschenbeutel, and D. Meschede, *Neutral Atom Quantum Register*, *Physical Review Letters* **93**, 150501 (2004)
- [22] Jurgen Volz, Markus Weber, Daniel Schlenk, Wenjamin Rosenfeld, Johannes Vrana, Karen Saucke, Christian Kurtsiefer, and Harald Weinfurter, *Observation of Entanglement of a Single Photon with a Trapped Atom*, *Physical Review Letters* **96**, 030404–4 (2006)
- [23] M. P. A. Jones, J. Beugnon, A. Gaetan, J. Zhang, G. Messin, A. Browaeys, and P. Grangier, *Fast quantum state control of a single trapped neutral atom*, *Physical Review A (Atomic, Molecular, and Optical Physics)* **75**, 040301–4 (2007)
- [24] Richard J. Cook, *What are Quantum Jumps?*, *Physica Scripta* **T21**, 49–51 (1988)
- [25] Sze M. Tan, *A computational toolbox for quantum and atomic optics*, *Journal of Optics B: Quantum and Semiclassical Optics* **1**, 424–432 (1999)
- [26] Rodney Loudon, *The Quantum Theory of Light*, Oxford University Press, third edition (2000)

- [27] Richard J. Cook and H. J. Kimble, *Possibility of Direct Observation of Quantum Jumps*, Physical Review Letters **54**, 1023 (1985)
- [28] M. Khudaverdyan, W. Alt, T. Kampschulte, S. Reick, A. Thobe, A. Widera, and D. Meschede, *Quantum jumps and conditional spin dynamics in a strongly coupled atom-cavity system*, arXiv:0901.3738 (2009)
- [29] D. T. Pegg, R. Loudon, and P. L. Knight, *Correlations in light emitted by three-level atoms*, Physical Review A **33**, 4085 (1986)
- [30] Wayne M. Itano, J. C. Bergquist, and D. J. Wineland, *Photon antibunching and sub-Poissonian statistics from quantum jumps in one and two atoms*, Physical Review A **38**, 559 (1988)
- [31] L. Mandel, *Sub-Poissonian photon statistics in resonance fluorescence*, Optics Letters **4**, 205–207 (1979)
- [32] Warren Nagourney, Jon Sandberg, and Hans Dehmelt, *Shelved optical electron amplifier: Observation of quantum jumps*, Physical Review Letters **56**, 2797 (1986)
- [33] J. C. Bergquist, Randall G. Hulet, Wayne M. Itano, and D. J. Wineland, *Observation of Quantum Jumps in a Single Atom*, Physical Review Letters **57**, 1699 (1986)
- [34] Th. Sauter, W. Neuhauser, R. Blatt, and P. E. Toschek, *Observation of Quantum Jumps*, Physical Review Letters **57**, 1696 (1986)
- [35] Th. Basche, S. Kummer, and C. Brauchle, *Direct spectroscopic observation of quantum jumps of a single molecule*, Nature **373**, 132–134 (1995)
- [36] S. Peil and G. Gabrielse, *Observing the Quantum Limit of an Electron Cyclotron: QND Measurements of Quantum Jumps between Fock States*, Physical Review Letters **83**, 1287 (1999)
- [37] Sebastien Gleyzes, Stefan Kuhr, Christine Guerlin, Julien Bernu, Samuel Deleglise, Ulrich Busk Hoff, Michel Brune, Jean-Michel Raimond, and Serge Haroche, *Quantum jumps of light recording the birth and death of a photon in a cavity*, Nature **446**, 297–300 (2007)
- [38] L. K. Thomsen, S. Mancini, and H. M. Wiseman, *Spin squeezing via quantum feedback*, Physical Review A **65**, 061801 (2002)
- [39] Brian Julsgaard, Alexander Kozhekin, and Eugene S. Polzik, *Experimental long-lived entanglement of two macroscopic objects*, Nature **413**, 400–403 (2001)
- [40] M. A. Nielsen and I. L. Chuang, *Quantum Computation and Quantum Information*, Cambridge University Press (2000)

-
- [41] M. Khudaverdyan, W. Alt, I. Dotsenko, T. Kampschulte, K. Lenhard, A. Rauschenbeutel, S. Reick, K. Schorner, A. Widera, and D. Meschede, *Controlled insertion and retrieval of atoms coupled to a high-finesse optical resonator*, New Journal of Physics **10**, 073023 (2008)
- [42] Gerd Fischer, *Stochastik Einmal Anders*, Friedr. Vieweg & Sohn Verlag, 1st edition (2005)
- [43] Christine Guerlin, Julien Bernu, Samuel Deleglise, Clement Sayrin, Sebastien Gleyzes, Stefan Kuhr, Michel Brune, Jean-Michel Raimond, and Serge Haroche, *Progressive field-state collapse and quantum non-demolition photon counting*, Nature **448**, 889–893 (2007)
- [44] S. Haroche and J. M. Raimond, *Exploring the Quantum*, Oxford University Press (2006)
- [45] H. A. Bachor, *A Guide to Experiments in Quantum Optics*, Wiley-VCH (1998)
- [46] Daniel Oblak, Plamen G. Petrov, Carlos L. Garrido Alzar, Wolfgang Tittel, Anton K. Vershovski, Jens K. Mikkelsen, Jens L. Sørensen, and Eugene S. Polzik, *Quantum-noise-limited interferometric measurement of atomic noise: Towards spin squeezing on the Cs clock transition*, Physical Review A **71**, 043807 (2005)
- [47] S. Haroche and J. M. Raimond, *Manipulation of Nonclassical Field States in a Cavity by Atom Interferometry*, in P. R. Berman, ed., *Cavity Quantum Electrodynamics*, Academic Press, Inc. (1994)
- [48] D. A. Steck, *Cesium D Line Data* (23 January 1998, Revision 1.5, 21 November 2002), <http://steck.us/alkalidata/>

Acknowledgments

Thank you, Sebastian, Tobias and Mika for introducing me to this exciting, but complex experiment and answering all my questions during the last year. It has been a pleasure to be part of the Cavity Team.

Thank you, Wolfgang for always having time for discussions and for giving simple answers to complicated questions. Your answers as well as your questions have been invaluable during my time at the cavity experiment.

Thank you, Artur for your positive attitude even when things didn't work.

Thank you, Tobias, Sebastian, Mika, Wolfgang, Artur and Martin for your helpful comments and suggestions while reading parts of my manuscript.

Thank you, Prof. Meschede for giving me the possibility to work in your group. Thank you also for trying to open my eyes for the broader context of our research, which sometimes disappears behind the technical details of the lab work.

Thank you, Prof. Benson for making this Diplomarbeit in Bonn possible and for your straightforward cooperation.

Thank you, Dietmar, Fien and Annelise for helping me through the bureaucracy of the IAP.

Thanks everybody in the Meschede Group. Hiking, coffee, cake and mensa was always fun.

Thank you, Bernhard and Regina for constantly supporting me during my studies.

Ich versichere, dass ich diese Arbeit selbständig verfasst und keine anderen als die angegebenen Quellen und Hilfsmittel benutzt sowie die Zitate kenntlich gemacht habe.

1. Gutachter: Prof. Dr. Oliver Benson
2. Gutachter: Prof. Dr. Dieter Meschede